REPORT DOCUMENTATION PAGE

Form Approved

OMB No. 0704-0188

1. REPORT DATE *(DD-MM-YYYY)*	2. REPORT TYPE	3. DATES COVERED *(From - To)*
12-06-2014	Final	26 Sept 2012 to 25 Sept 2013

4. TITLE AND SUBTITLE

Multi-scale Computational Electromagnetics for Phenomenology and Saliency Characterization in Remote Sensing

5a. CONTRACT NUMBER
FA2386-12-1-4082

5b. GRANT NUMBER
Grant AOARD-124082

5c. PROGRAM ELEMENT NUMBER
61102F

6. AUTHOR(S)

Prof Hean-Teik Chuah

5d. PROJECT NUMBER

5e. TASK NUMBER

5f. WORK UNIT NUMBER

7. PERFORMING ORGANIZATION NAME(S) AND ADDRESS(ES)

Universiti Tunku Abdul Rahman
No9, Jalan Bersatu 13/4, Petaling Jaya,
Selangor Darul Ehsan 47500
Malaysia

8. PERFORMING ORGANIZATION REPORT NUMBER
N/A

9. SPONSORING/MONITORING AGENCY NAME(S) AND ADDRESS(ES)

AOARD
UNIT 45002
APO AP 96338-5002

10. SPONSOR/MONITOR'S ACRONYM(S)
AFRL/AFOSR/IOA(AOARD)

11. SPONSOR/MONITOR'S REPORT NUMBER(S)
AOARD-124082

12. DISTRIBUTION/AVAILABILITY STATEMENT

Approved for public release.

13. SUPPLEMENTARY NOTES
This research effort is continued for two more years.

14. ABSTRACT

For earth observation, microwave remote sensing has been a useful technology that provides sensing capability of earth terrain with wide coverage. Images from satellite based Synthetic Aperture Radar (SAR) are acquired to provide ground information about various types of earth terrain sensed (such as vegetation, farm, urban area, sea ice and snow covered land, etc). In order to interpret these SAR images correctly, it is necessary to understand how microwave interacts with these earth media.

15. SUBJECT TERMS

Electromagnetics, Remote Sensing, Electromagnetic scattering

16. SECURITY CLASSIFICATION OF:			17. LIMITATION OF ABSTRACT	18. NUMBER OF PAGES	19a. NAME OF RESPONSIBLE PERSON
a. REPORT	b. ABSTRACT	c. THIS PAGE			Seng Hong, Ph.D.
U	U	U	SAR	84	19b. TELEPHONE NUMBER *(Include area code)* +81-3-5410-4409

Standard Form 298 (Rev. 8/98)
Prescribed by ANSI Std. Z39.18

Report Documentation Page

Form Approved
OMB No. 0704-0188

1. REPORT DATE	2. REPORT TYPE	3. DATES COVERED
12 JUN 2014	**Final**	**26-09-2012 to 25-09-2013**

4. TITLE AND SUBTITLE	5a. CONTRACT NUMBER
Multi-scale Computational Electromagnetics for Phenomenology and Saliency Characterization in Remote Sensing	**FA2386-12-1-4082**
	5b. GRANT NUMBER
	5c. PROGRAM ELEMENT NUMBER
6. AUTHOR(S) **Hean-Teik Chuah**	5d. PROJECT NUMBER
	5e. TASK NUMBER
	5f. WORK UNIT NUMBER
7. PERFORMING ORGANIZATION NAME(S) AND ADDRESS(ES) **Universiti Tunku Abdul Rahman,No9, Jalan Bersatu 13/4, Petaling Jaya,Selangor Darul Ehsan ,Malaysia,ML,47500**	8. PERFORMING ORGANIZATION REPORT NUMBER **N/A**
9. SPONSORING/MONITORING AGENCY NAME(S) AND ADDRESS(ES) **AOARD, UNIT 45002, APO, AP, 96338-5002**	10. SPONSOR/MONITOR'S ACRONYM(S) **AFRL/AFOSR/IOA(AOARD)**
	11. SPONSOR/MONITOR'S REPORT NUMBER(S) **AOARD-124082**

12. DISTRIBUTION/AVAILABILITY STATEMENT
Approved for public release; distribution unlimited

13. SUPPLEMENTARY NOTES

14. ABSTRACT
For earth observation, microwave remote sensing has been a useful technology that provides sensing capability of earth terrain with wide coverage. Images from satellite based Synthetic Aperture Radar (SAR) are acquired to provide ground information about various types of earth terrain sensed (such as vegetation, farm, urban area, sea ice and snow covered land, etc). In order to interpret these SAR images correctly, it is necessary to understand how microwave interacts with these earth media.

15. SUBJECT TERMS
Electromagnetics, Remote Sensing, Electromagnetic scattering

16. SECURITY CLASSIFICATION OF:			17. LIMITATION OF ABSTRACT	18. NUMBER OF PAGES	19a. NAME OF RESPONSIBLE PERSON
a. REPORT **unclassified**	b. ABSTRACT **unclassified**	c. THIS PAGE **unclassified**	**Same as Report (SAR)**	**84**	

AOARD Final Report

Multi-scale Computational Electromagnetics for Phenomenology and Saliency Characterization in Remote Sensing

(Award No: FA2386-12-1-4082)

H.T.Chuah[1] (PI), Lijun Jiang[2], W.C. Chew[3], H.T.Ewe[1], J.Y. Koay[1] and Y.J.Lee[1]

[1]Universiti Tunku Abdul Rahman, Malaysia
[2]University of Hong Kong, Hong Kong
[3]University of Illinois at Urbana Champaign, U.S.A.

1. Introduction

This report provides the progress update of the work done under this grant from January-December 2013 with the topic of multi-scale computational electromagnetics for phenomenology and saliency characterization in remote sensing. The total duration of the project is 3 years and the remaining two years will be supported under FA2386-13-1-4140.

The objectives of this project are to

i. Identify the most influential factors of the full-wave scattering models,
ii. Investigate the feasibility of using computational electromagnetics to characterize the scattered fields of scatterers in earth terrain, and
iii. Study the use of advanced and emerging methods in multi-scale computational electromagnetics for generating synthetic aperture radar data.

2. Project Background

For earth observation, microwave remote sensing has been a useful technology that provides sensing capability of earth terrain with wide coverage. Images from satellite based Synthetic Aperture Radar (SAR) are acquired to provide ground information about various types of earth terrain sensed (such as vegetation, farm, urban area, sea ice and snow covered land, etc). In order to interpret these SAR images correctly, it is necessary for us to understand how microwave interacts with these earth media.

As these media are generally complex, traditionally researchers will model the media with simplified structure and configuration. For solutions that are based on electromagnetic wave analysis, it is common to model the medium with a fluctuating part embedded in a homogenous host medium. This approach may

provide the estimation of radar returns from the medium, but normally is not able to identify easily the various scattering mechanisms and strength caused by complex structure in the natural medium.

The other approach which is commonly pursued is based on energy transportation theory (Radiative Transfer Theory) to study how energy propagates and how it is scattered in the medium based on random discrete medium, where there are multiple types and shapes of scatterers embedded in the host medium. For this approach, it is normally suitable to identify the contributions of various scattering mechanisms from various scatterers and interfaces. As this is energy based solution, various improvement methods have been introduced to incorporate the phase information so that coherence effects from groups of scatterers can be countered for. However, as normally basic shapes of scatterers (such as cylinders, needles, disks, ellipsoids) are used to represent the complex natural objects such as leaves, branches, trunks, brine inclusion and air bubbles, that leaves room of improvement in modeling the natural media more accurately.

In recent years, with the rapid development in information and communication technology, the field of Computational Electromagnetics (CEM) has grown tremendously. Various methods such as EPA (Equivalence Principle Algorithm) have been developed to model and calculate scattering and radiation from complex circuit board, antenna arrays, and object as big as a tank. The full wave solution obtained can provide accurate account of scattering from complex structure found in semiconductor industry.

Thus, with the advances in the areas of Computational Electromagnetics (CEM) and Microwave Remote Sensing (MRS), it shows good potential and is also the main aim of this project that we design new integrated approach to improve techniques in EPA for the development of theoretical model for microwave remote sensing and prediction of radar returns from earth terrain which is complex in nature.

3. Description of Project Activities and Achievement

a. Initial design of research approach with cross-disciplinary study

The project team has conducted updated literature survey on the fields of microwave remote sensing of vegetation and EPA based computational electromagnetics, aiming to design suitable research approach to achieve the project objectives. Among the activities carried out are:

(i) Literature survey on microwave remote sensing of tropical vegetation. Traditionally, theoretical models for modeling of vegetation developed by various research teams in the world have been focusing on temperate vegetation where dense vegetation such as tropical vegetation is less researched on. In order to develop a theoretical model which is applicable for a wide range of vegetation, it is necessary that the model is able to cover the case of dense vegetation. Based on this model, various remote sensing applications that can later be developed by research community are applications such as landuse classification, crop yield prediction, growth monitoring of vegetation, surveillance of objects beneath vegetation, biomass prediction and retrieval of vegetation parameters through inverse models. Detailed finding on microwave remote sensing for tropical vegetation has been published and can be found in Appendix 1.

(ii) Design of development stages of model. Utilizing EPA for the modeling of actual natural medium such as vegetation can be challenging if full details and exact copy of vegetation are to be scanned and modeled. As suggested in the project proposal, it is important for us to identify salient scattering mechanisms in the microwave interaction with the medium and finally implement an efficient theoretical model based on EPA with reduced complexity of the configuration of vegetation which still captures the dominant components involved in the microwave interaction. A two-stage model development approach is designed and attached in Appendix 2.

b. Theoretical Simulation and Analysis of Scattering Mechanisms from Vegetation

A series of simulation and analysis of scattering mechanism for various types of vegetation was carried out earlier, covering dense vegetation like tropical forest and plantation/crop (such as oil palm and rice field). This simulation was done based on second order iterative solution of Radiative Transfer model with DMPACT (Dense Medium Phase and Amplitude Correction Theory) and Fresnel amplitude and phase correction for multilayer random discrete medium. The analysis of the theoretical simulation is attached in Appendix 3.

c. Pilot Ground Truth Measurement

For actual modeling of natural medium, it is necessary for ground truth measurement to be done to provide a better understanding of the plant growth

and also physical configuration and parameters of the trunk, branches and leaves of plant. A pilot ground truth measurement site has been identified and conducted in two estates in Perak State in Malaysia. Appendix 4 gives a preliminary report of the ground truth measurement done.

d. Loop-tree free low frequency equivalence principle algorithm

Equivalence principle is a powerful principle that will be employed in this project to handle the involved physical process in the remote sensing of the vegetables. Due to the usage of the P band or L band which are very low in the sensing process, a low frequency equivalent principle algorithm method is needed. In this work, we developed a newly developed integral equation domain decomposition method for solving complex low frequency electromagnetic problems. This method is based on low frequency augmented equivalence principle algorithm with the augmented electric field integral equation. The augmented electric field integral equation provides a stable solution in the low frequency regime since it includes both charge and current as unknowns to avoid the imbalance between the vector potential and the scalar potential. Based on similar idea, the augmented equivalence principle algorithm can suppress the projection error resulting from low frequency problems of the normal equivalence principle algorithm. Combining these two methods, the proposed algorithm can be used in domain decomposition problems and is numerically stable at low frequencies. Several numerical examples are provided to verify its validity. The development of this method effectively enables the applications of equivalence principle algorithms to be used for broadband scattering analysis. For details, please refer to Appendix 5.

e. A Novel Broadband Equivalent Source Reconstruction Method for Broadband Radiators

To characterize and analyze general radiators such as those involved in the remote sensing process, equivalent source reconstruction methods can be employed to identify where is the hot spot (strong radiation contributor). Traditional equivalent source reconstruction methods are only operating at a single frequency point each time. However, for wide band radiators, their computation cost of the source reconstruction increases linearly with the number of frequency points. In this work, a wide-band equivalent source reconstruction method (WB-SRM) based on the Neville-type Stoer-Bulirsch (SB) algorithm is developed. Supported by the adaptive frequency sampling (AFS) scheme, the number of required sampling data is significantly reduced, which leads to much better computational efficiency. During the AFS process, three fitting models (FM) are considered: two are “triangle rules”, and another one is “rhombus rule”. The combination of these three FMs will result in different sampling schemes. In this work, a bisection searching strategy is performed. Numerical examples are presented to validate the proposed WB-SRM and demonstrate its accuracy and applications. This method is extremely useful to the broadband complex scattering and radiation simulations and is

able to achieve the high modeling efficiency conveniently. Appendix 6 gives a detailed description of this method.

4. Some of the research output has been reported in the publication shown below:

- Z.H. Ma, L.J. Jiang, and W.C. Chew (2013), "Loop-tree Free Augmented Equivalence Principle Algorithm for Low-frequency Problems," Microw. and Opt. Techn. Lett. , vol. 55, no. 10, pp. 2475-2479, Oct. 2013.
- P. Li, L.J. Jiang, and J. Hu, "A Wide-band Equivalent Source Reconstruction Method Exploiting the Stoer-Bulirsch Algorithm with the Adaptive Frequency Sampling," IEEE Trans. On Antennas and Propagations, vol. 61, no. 10, pp. 5338-5343, Oct. 2013.
- Y.J. Lee, H. T. Ewe, and H.T. Chuah (2013), "Microwave Remote Sensing for Tropical Vegetation," Journal of Science and Technology in the Tropics, Vol. 9, pp. 47-78.
- K. C. Teng, J. Y. Koay, S. H. Tey, Y. J. Lee, H. T. Ewe and H. T. Chuah (2013), "Microwave Remote Sensing of Vegetation: A Study on Oil Palm and Rice Crops," The 2013 International Seminar on Communication, Electronics and Information Technology (ISCEIT2013), Thailand
- Y.J.Lee, H.T.Ewe and H.T.Chuah (2013), "A General Overview on the Microwave Remote Sensing of Tropical Vegetation," Progress in Electromagnetics Research Symposium (PIERS), March, Taipei, Taiwan.

5. Summary

In general, the project will be continued under another grant to further investigate how the new EPA algorithm can be applied to the scattering modeling of sea ice and trees so that theoretical model based on radiative transfer theory that utilizes EPA algorithm in the calculation of phase matrices of natural scatterers in earth terrain can be developed and the simulation of radar backscattering returns will be validated with satellite SAR images. The other aspect of the work will focus on how the computing scale of the developed algorithms can be upgraded. Various fast computing optimization techniques such as fast multipole algorithm will be studied and incorporated in the model.

Acknowledgement

The project team would like to acknowledge and thank for AOARD/AFOSR for the grant awarded and strong support given to the project. Acknowledgement also goes to other related external funding agencies, the universities and organizations involved for their support and assistance in this project.

Appendix 1:

Journal of Science and Technology in the tropics (2013) 9: pp. 47-78

Microwave remote sensing for tropical vegetation

Yu Jen Lee[1], Hong Tat Ewe[2,*] and Hean Teik Chuah[2]
[1]Faculty of Engineering and Green Technology, Universiti Tunku Abdul Rahman, Jalan Universiti, Bandar Barat, 31900 Kampar, Perak D. R., Malaysia
[2]Faculty of Engineering and Science, Universiti Tunku Abdul Rahman, UTAR Complex, Jalan Genting Kelang, 53300 Setapak, Kuala Lumpur, Malaysia
(*Email: eweht@utar.edu.my)

ABSTRACT A review of literature on the development and use of microwave remote sensing for vegetation in the tropics are presented. In particular, the principal areas of interest include the following:
1. Development of theoretical models to understand the electromagnetic wave-target interaction mechanisms of various types of vegetation. Such models are critical as they form the basis towards the generation of new techniques for recovering vegetation properties from electromagnetic scattering data.
2. Advancement in ground truth measurement techniques and equipment as well as collection of measurement data for future research. New methods have been developed to measure critical properties of vegetation, such as the waveguide thin sheet method for dielectric constants of leaf samples. The design of new equipment, such as scatterometers and airborne SAR systems to measure backscattering coefficients of vegetation is also important. The numerous data collected during ground truth measurements by various research groups have paved the way for the use of remote sensing technology on vegetation.
3. Image processing and classification techniques to distinguish different types of vegetation and terrain. These form the tools for large scale monitoring of crops and forests using SAR imagery. Such techniques are important, especially for the application of microwave remote sensing in disease control of crops, crop planting management and forest logging monitoring.

Keywords microwave – remote sensing – tropical – vegetation

INTRODUCTION

The use of microwave remote sensing has been advancing rapidly and has been targeted as a primary solution to earth resource monitoring and management [1]. There is currently substantial existing work being done on the use of remote sensing for various media, such as sea ice and ocean [2, 3]. In remote sensing of tropical vegetation, observations of the electromagnetic fields scattered or emitted by vegetation are used to characterize the physical properties and conditions of the plants. Large-scale information obtained from such methods is important towards applications such as the monitoring of agricultural crops and the maintenance of tropical forests.

In the tropics, such as Asian countries, where rice is the staple food, the capability to predict the yield of paddy for a particular year may assist government agencies in the planning of food resources for its people. The use of remote sensing as a tool to enable the use of crop models for yield prediction and other applications has been recommended [4]. In terms of monitoring of large areas of crops, the use of remote sensing images with the proper image classification techniques may assist towards the control of diseases or natural hazards, thus reducing the losses of both farmers and the government, where the export of the crops may play a huge role towards the country's economy. There has been reported work on using electromagnetic data to discriminate fungal disease infestation in oil palm [5].

With the current global focus shifting towards climate change and environmental issues, the use of remote sensing towards the maintenance and monitoring of tropical forests is also being considered. Logging activities and deforestation are issues currently being tackled by several tropical countries, such as in Brazil, where the Amazon rain forests are located and also in the rain forests in Malaysia and Indonesia. Illegal logging has caused losses in millions of dollars for these countries. Such activities also contribute towards the extinction of several indigenous species of flora and fauna unique to these rain forests. Due to the vast amount of areas covered by such virgin forests, it is impossible for park rangers to cover the entire landscape to counter illegal logging or deforestation. Several efforts had been made to propose the use of remote sensing to monitor the tropical rain forests, such as the development of a monitoring system for tropical rainforest management by a joint research group from Malaysia and Japan [6].

Regardless of how remote sensing is to be applied towards vegetation, it is important to note that the development of proper theoretical models, the collection of measurement data as well as the advancement of image classification techniques are required in order to realize the potential of using remote sensing techniques for such purposes. In this paper, the collection of such methods and their principal results are reported, with focus given primarily on tropical vegetation such as paddy, oil palm and forests.

THEORETICAL MODELING OF TROPICAL VEGETATION

In this section, several theoretical models developed to better understand the relationship between the scattering properties of tropical vegetation and microwaves are reported. In addition, models developed to model certain parameters of tropical vegetation are also discussed. The models discussed below are but a few of the current work being done to meet this task.

Paddy

Rice plays an integral role as the staple food of most Asians and is an important agricultural crop. In China and Malaysia, the planting of paddy is important to ensure the production of sufficient food source for the people. Due to its

importance, emphasis has been given to find methods to predict the yield of rice and also to monitor the growth of paddy [4]. There has been a growing interest towards the development of proper theoretical models to understand the scattering properties of paddy.

Radiative Transfer Model with DMPACT and Fresnel Corrections

There has been reported work on modeling paddy for the purpose of calculating the backscattering coefficients. Koay *et al*. [7] proposed to model paddy as an electrically dense media. In this method, paddy is modeled either as a single layer or multilayered dense discrete random medium consisting of cylindrical and needle-shaped scatterers, depending on the different growth stages (Fig. 1). In Malaysia, seeds are broadcasted randomly, resulting in fields with higher density and randomness [7]. Due to this, previous works such as the branching model for vegetation [8] and Foldy-Lax multiple-scattering equations [9], which consider the clustering effects from the positions of scatterers, may not be accurate for the scenario in Malaysia as these methods apply more to plants that are planted in rows with space in between clusters of plants.

In order to take into account the coherent and near-field effects of the closely spaced scatterers, the Dense Medium Phase and Amplitude Correction Theory [10] is incorporated into the phase matrix. In addition, the Fresnel field effects are also considered as further improvements to the phase matrices of dense media [11-14]. The phase matrix is then applied into the Radiative Transfer equations [15, 16] and solved up to the second order [17] to consider double-volume scattering.

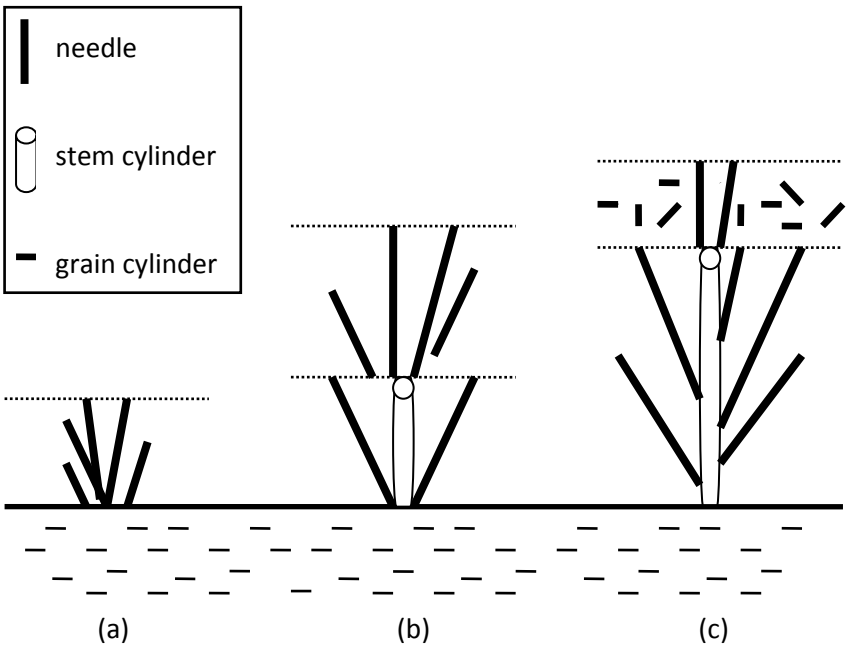

Figure 1. Variations in the model used for the computation of backscattering coefficients of paddy fields in the (a) early vegetative stage, (b) late vegetative stage, and (c) reproductive stage [7].

The theoretical model was used to calculate the backscattering coefficients of the paddy canopies, where the measured ground truth parameters such as plant geometry, dielectric constants and volume fractions were incorporated into the theoretical model equations for simulation. The ground truth measurements were carried out in Sungai Burung, Selangor, Malaysia. In addition, RADARSAT images were obtained at 24-day intervals. The specifications for the RADARSAT image were: C-band frequency of 5.3GHz, HH polarization, Fine Mode 2 with a

resolution of about 8 m and an incident angle range of 39 °–42 °. Table 1 shows the model variation used for the different growth stages of rice crops, which corresponds to the plant age and dates of the RADARSAT image acquired.

Table 1. Variations in the model for different growth stages [7].

Date	Test Field	Age (days)	Model Variation
20-09-2004	1	27	Early vegetative
	4	26	
	5	29	
	6	21	
14-10-2004	1	51	Late vegetative
	4	50	
	5	53	
	6	45	
06-11-2004	1	75	Early reproduction
	4	74	
	5	77	
	6	69	

The model was used to calculate the HH-polarized backscattering coefficients of several test fields at a frequency of 5.3GHz and at an incident angle of 41 ° in order for comparisons with the RADARSAT data. Figure 2 shows the comparison between the model prediction and the actual backscattering coefficients calculated from the RADARSAT image for different stages of growth.

It was observed that the total backscattering coefficient increased during the vegetative stages of the paddy plants as the plants grew taller and denser, but decreased slightly at the reproductive stage, which might be due to halted growth of plants and the dying off of smaller plants. The results show good matching in general, but errors of about 2 dB were noticed at the age of 50 days. Such errors were expected since the ground truth measurements were not exact statistical representations of actual fields and might not be accurate. Another possible reason could be the needle shape used to model the leaves, which might not be suitable as some leaves could be wider in dimension.

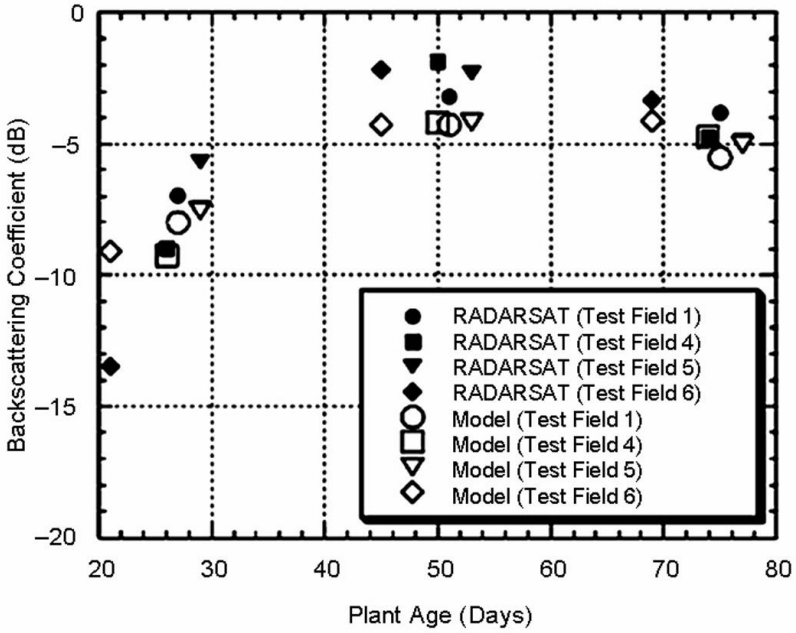

Figure 2. Comparisons of theoretical and measured HH-polarized backscattering coefficients at different stages of growth [7].

Comparisons between the dense medium model and the Monte Carlo simulations were also carried out for VV-polarized backscattering coefficients based on parameters given in [18]. Figure 3 shows that there was not much difference in the results when the plants had a lower biomass when they were young. However, as the plants grew and the biomass increased, the dense medium model gave a better match with the ERS-1 data obtained at Samarang [18] and Akita [19] due to the higher density of the canopy.

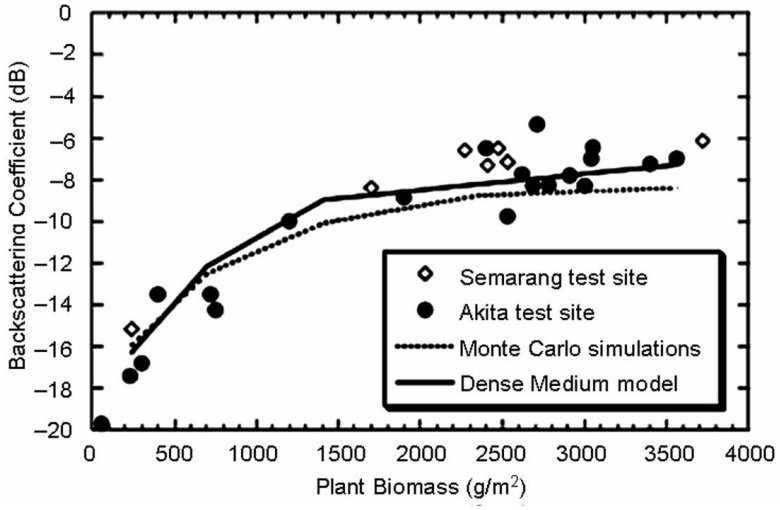

Figure 3. Comparisons of the backscattering coefficients obtained through the dense medium model, Monte Carlo simulations, and ERS-1 data with respect to the plant biomass [7].

In summary, a theoretical model developed for paddy fields using Radiative Transfer theory was proposed [7] with consideration given to the coherent and near-field effects of closely packed scatterers by incorporating the DM-PACT and

Fresnel correction terms in the phase matrix of the paddy canopy. Multiple volume scattering was also considered by incorporating second-order solutions of the Radiative Transfer theory. Utilizing ground truth measurements obtained for an entire season at Sungai Burung, Selangor, Malayia, a theoretical analysis using the model was carried out (detailed discussion of the analysis can be found in [7]). It was found that multiple-volume scattering effects are important in the calculation of cross-polarized backscattering coefficients and will be critical for applications involving polarimetric data. Coherent effects need to be considered at lower frequencies while Fresnel corrections are more important at higher frequencies. The simulated results compared with RADARSAT images and the Monte Carlo simulations showed promising results. A suggestion to improve the model is to use elliptical disk-shaped scatterers in the phase matrix [20].

Vector Radiative Transfer Model

There are also other backscattering models utilizing Radiative Transfer theory. Ma *et al*. [21] proposed a first-order microwave backscattering model for rice canopy, where the rice canopy is characterized as a uniform layer containing leaves and stems, while the spike of rice is omitted. The model is based on the Vector Radiative Transfer theory [22] and adapts the MIMICS backscattering model originally developed for forest canopy. The backscattering coefficient of the various polarizations was calculated as:

$$\sigma_{vv}^0 = 4\pi\mu_0[T]_{11}, \sigma_{hh}^0 = 4\pi\mu_0[T]_{22}$$
$$\sigma_{hv}^0 = 4\pi\mu_0[T]_{21}, \sigma_{vh}^0 = 4\pi\mu_0[T]_{12} \quad (1)$$

Figure 4 shows the variations of the rice backscattering with the date at C-band, with the incidence angle at 23 °. 3D figures were then plotted with reference to the dates (Fig. 4) to illustrate that the backscattering coefficient depends on the incidence angle and varies with the growth for L-band, C-band and X-band. The results obtained were consistent with work reported in [18] and [19]. The plot for C-band are shown in Figure 5.

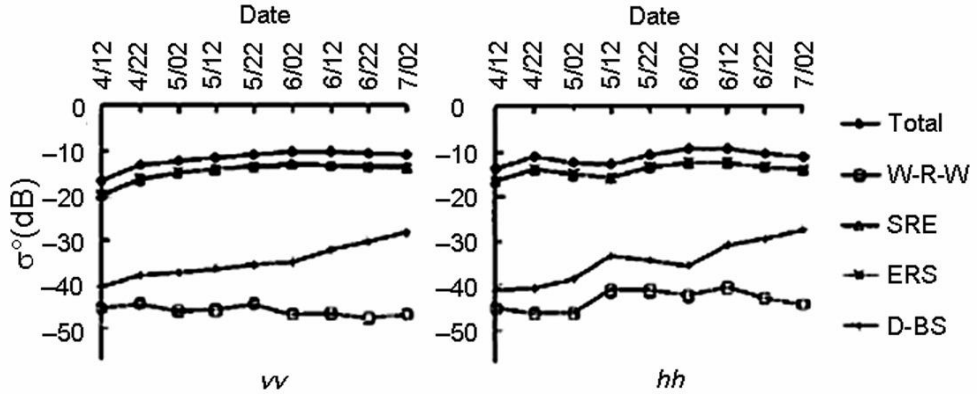

Figure 4. The variations of the rice backscattering coefficient with date (C-band, incidence angle = 23 °) [21].

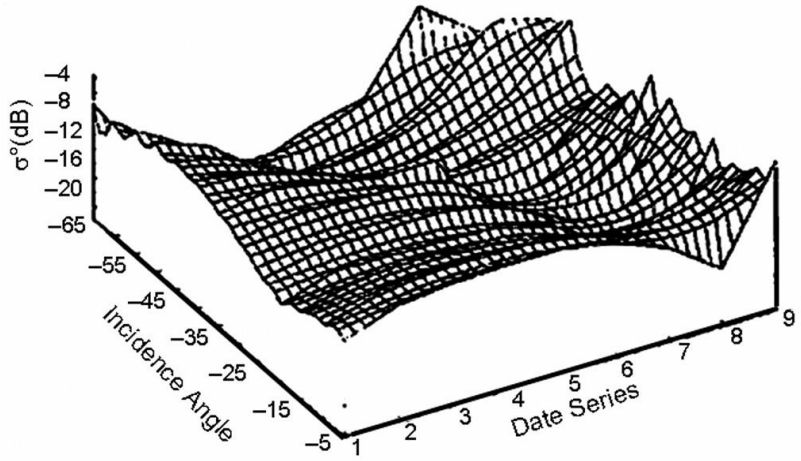

Figure 5. C-band HH polarization [21].

Single Layer Radiative Transfer Model

Shao *et al*. [23] successfully predicted the radar backscatter behaviour of rice by using an established Radiative Transfer model for vegetation canopies developed by Sun *et al*. [24] on rice. The study focused on the temporal characteristics of rice backscatter as a function of polarization at C-band. This study was carried out in the Zhaoqing test site located in Guangdong Province in Southern China. The multi-temporal RADARSAT image set comprised of 7 scenes acquired in Standard Mode from April to July, 1997. Rice physical measurements were carried out during the period of the RADARSAT acquisition. The fresh biomass of rice was determined by:

$$M = [1000/a \times 1000/b] \times W_f \times N \qquad (2)$$

where a is the row spacing; b, the line spacing; W_f, the fresh weight of each rice seedling; and N, the numbers of rice seedling of each cluster. The dielectric of rice was calculated from the gravimetric water content using the empirical Dual-dispersion model [25].

The model was used to generate backscatter coefficients for all polarizations. It was found that for HH polarization, the generated data managed to fit the few RADARSAT observations reasonably well (Fig. 6).

Further analysis of the generated backscatter coefficients shows that at a 45 ° incidence angle, crown backscatter at HH and HV polarization increases as the rice grows. However, at VV polarization the crown backscatter increases at the early stage of the rice growth cycle and then stays relatively constant for the rest of the rice growth cycle, which corresponds to results reported in [18]. Further research is needed to fully utilize the model's capabilities.

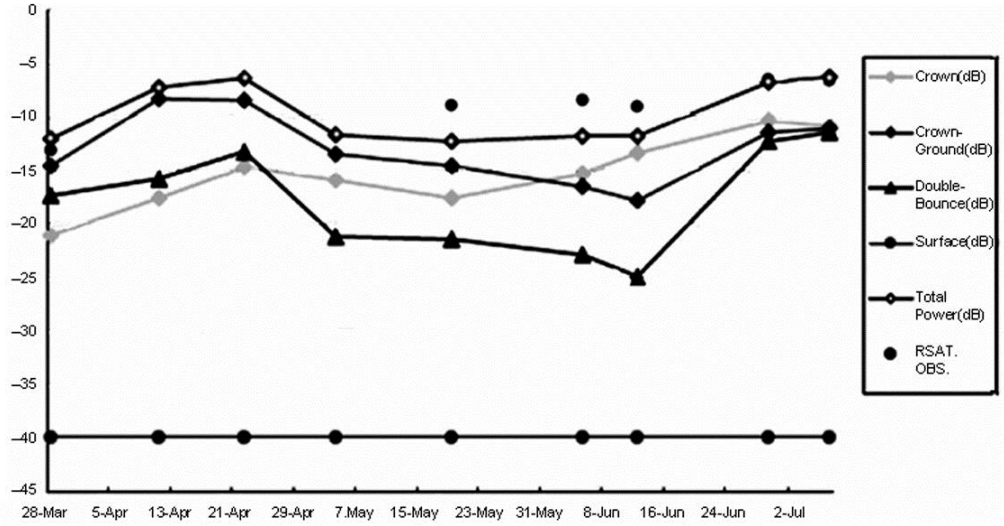

Figure 6. Comparing model results with RADARSAT observations in 1997 [23].

Coherent Electromagnetic Model

Other works on theoretical modeling of rice include work done by Fortuny-Guasch *et al*. [26] and Ma *et al*. [27]. In [26], a physics-based coherent electromagnetic model tailored for the computation of radar backscatter from rice was developed. The model considers the rice as an arrangement of plants over a flooded soil, where the plants are modeled as clusters of dielectric cylinders. The results show that the co-polar backscattering coefficients obtained by the model are similar to the measured ones, but the cross-polar scattering obtained is much lower. Future consideration into multiple scattering between stems was suggested as an improvement to the current model.

Radiative Transfer Model with Lindenmayer System

In [27], the employment of the Lindenmayer system (L-system) [28] and computer graphics technique to describe the realistic structure of the rice crops was studied. On the basis of such method, according to the physical interaction principle between electromagnetic wave and vegetation, the intensity of scattered field of each scatterer was calculated. By coherent addition of the individual scattered field of each scatterer, the total backscattered field of the crop canopy can be obtained and the backscattering coefficients can be calculated. The simulation results were compared with the measurement data obtained via scatterometer. The results show that the predication of backscatter is roughly identical to the measurement, especially when the incidence angle is between 20 °and 50 °.

Studies have also been conducted on relating physical properties of the rice to the microwave backscatter. Using the proper algorithms and models, the variations in the backscatter are compared with variations in certain parameters in the rice.

Modeling of Rice Parameters

The modeling of dielectric microwave properties of rice using the Debye-Cole dual-dispersion model of vegetation was studied in [29]. Results show that the dielectric constant of rice varies at different growth stages. The dielectric constant increases during the transplant to seedling developing period but decreases after that. On the other hand, microwave frequency, gravimetric moisture content of rice, temperature and density of dry rice canopy have an influence on dielectric constant. In the study, salinity had no effect on the dielectric constant.

The mapping of rice biomass was done using ALOS/PALSAR imagery [30]. By integrating a rice canopy scattering model [31], the spatial distribution of paddy

rice biomass was simulated. Plant height and density were the two most determinant biophysical parameters related to rice biomass, which could be retrieved with an error of less than 6 cm and 30/m^2, respectively. Thus, the biomass could be estimated with an adjusted residual of 200 g/m^2. The results indicate that the designed approach was useful to quantitatively estimate the carbon absorption from the atmosphere during the growing season of rice and demonstrated the potentials of using ALOS/PALSAR data for the mapping of rice biomass using the microwave canopy scatter model.

Another important parameter relating to microwave backscatter is the leaf area index (LAI). Stephen *et al*. [32] demonstrated this by modeling the flooded rice field as a single layer of discrete scatterers over a reflecting surface using the Distorted Born Approximation. At C-band, the VV polarization radar backscatter decreased with increasing LAI over the observed range of LAI. Further investigations using the simple model showed that the decrease was related to the domination of direct-reflected backscatter over the direct component. Model calculations suggested that at very low LAI the radar backscatter should increase with LAI.

Inoue *et al*. [33] observed unique interactions between each of the microwave backscatter coefficients at all combinations of five frequencies (Ka, Ku, X, C and L), all polarizations (HH, VH, HV and VV) and four incident angles (25°, 35°, 45° and 55°) and vegetation variables such as leaf index area (LAI), biomass and grain yield. The study revealed that the realistic cropping condition of rice would allow further quantitative insight on the interaction of backscatter with vegetation.

Oil Palm

Besides paddy, oil palm is another commodity that is important in the tropics. Palm oil is viewed as a potential biofuel source in the future as the amount of fossil fuel dwindles. It has also found uses as key ingredients in a variety of areas, such as cooking oil, soaps and glycerol. Countries such as Indonesia, Malaysia, Nigeria and Colombia are but a few of the tropical countries producing palm oil with the growth of oil palm plantations.

3D Model with Radiative Transfer Theory

Izzawati *et al*. [34] adapted a 3D radar backscatter model originally designed for forest canopies [35] to simulate high resolution images of polarimetric radar backscatter of oil palm plantations at different growth stages. The main purpose was to examine the relationships between the backscatter and texture and crop status in order to invert the latter from space borne SAR data. The individual crowns were modeled as hemispheres and distributed in a triangular pattern found in oil palm plantations. Polarimetric radar backscatter was then simulated for C and L band at high spatial resolution for a range of growth stages and LAI.

The original 3D radar backscatter matter was based on the Radiative Transfer equation for a forest canopy comprising a crown layer, trunk layer and rough-surface ground boundary. For the study, steps were taken to ensure the production of reliable oil palm plantation stands at different growth stages to be used as input in the model. Simulations were then carried out on the oil palm plantation using the theoretical model at C and L band.

Multipolarized high resolution images (0.5 m) were simulated using the model at years 2.5, 6.5 and 8.5 for C-band and at years 2.5, 4.5 and 6.5 for L-band (Fig. 7, 8). The estimation of the mean radar backscatter of C and L bands at HH, HV and VV polarizations were also completed. A texture analysis was also done using directional semivariograms. Early modeling results indicate the potential of using mean backscatter and semivariance measures to discriminate oil palm stand age.

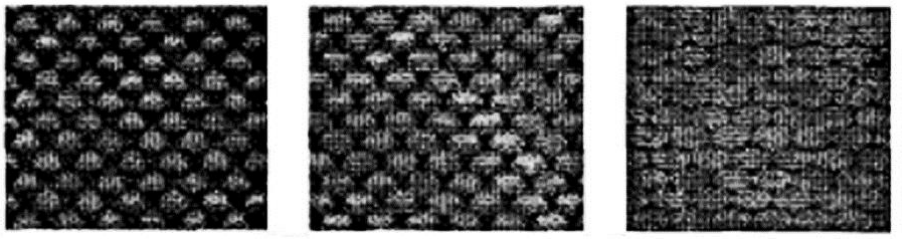

Figure 7. C-band simulation at age 2.5, 6.5 and 8.5 years [34].

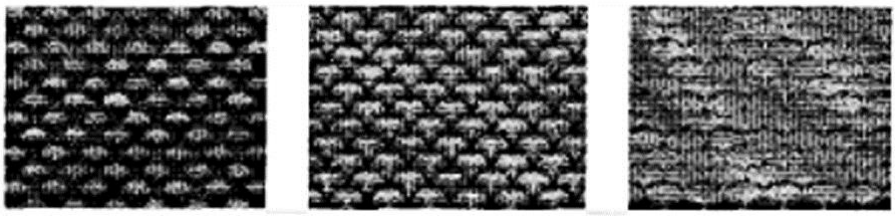

Figure 8. L-band simulation at age 2.5, 4.5, and 6.5 years [34].

Tropical Forest

There has been a multitude of reported work focusing on the modeling of vegetation in general [8, 11-13, 17, 35, 36]. Some of these models actually form the basis for the model developed for paddy and oil palm. Many of these models were previously validated on temperate climate forests, such as Boreal or Cypress forests. In this section, modeling done and validated on tropical forests is discussed.

Hybrid Coherent Scattering Model

Thirion *et al*. [37] looked into several earlier models and concluded that there is a need to study the different scattering mechanisms involved in the forest by means of a fully coherent scattering model (COSMO). They proposed a new hybrid model derived from the RVoG model. Retrieval studies indicated that the model seems to be more adapted to the P-band. COSMO is a coherent descriptive model that is applied to radiometry, interferometry and polarimetry. In the paper, the model was used to simulate SAR data for Mangrove (tropical) and Nezer (temperate) forests for P-band and L-band. The comparisons between the simulations and the real SAR data were satisfactory in radiometry for both types of vegetation. The model also showed good ability to simulate the interferometric data and polarimetric behaviour of the vegetation mentioned.

Multilayer Radiative Transfer Model

The use of multilayer models to model vegetation has also been proposed [11, 17]. Ewe *et al*. [11] treated vegetation as an electrically dense media. Utilizing the Radiative Transfer theory, the array phase correction factor was incorporated into the phase matrices of the nonspherical scatterers to take into account the coherent effect between scatterers. In addition, the amplitude and Fresnel phase corrections were also included when the Fresnel factor was larger than $\pi/8$. The improved phase matrix was then included into the Radiative transfer formulation. Finally this formulation was solved iteratively up to the second order to incorporate the multilayer effects. It was found that the measurement results for Japanese cypress and boreal forest with multifrequency and multipolarization data showed good agreement with the theoretical predictions from the model. There is huge potential for the model to be used to model for tropical dense forest.

Karam *et al*. [17] came up with a two layer scattering model for trees and tested it on both coniferous and deciduous trees. In the model, the two layers are the

crown layer and trunk layer above an irregular surface. Deciduous leaves, which are quite common in tropical trees, are modeled as randomly oriented circular discs. The advantages for this model is that it accounts for the first and second order scattering within the canopy, fully accounts for the surface roughness in the canopy-soil interaction terms, allows many branch sizes and orientation distributions, and finally is valid over a wide frequency range for both deciduous and coniferous vegetation.

Validation was carried out by applying the model to walnut and cypress trees. A comparison between the backscattering measurements and the model predictions was done. Additionally, the effects of frequency, second order interaction and surface roughness effects were studied. It was found that in order to obtain good matching between calculated and simulated backscattering coefficients, the branch size distribution is important. The model discretized branch size distribution into four sizes. Next, small branches and leaves generally contribute to the backscattering coefficients at X-band. For deciduous trees, cross polarization at X-band is dominated by stems rather than leaves. Lastly, soil moisture and soil roughness are more important for HH polarization as they influence the trunk-soil interaction contribution to the backscattering coefficients.

GROUND TRUTH MEASUREMENT OF TROPICAL VEGETATION

The development of theoretical models is important to understand the physics and interaction between electromagnetic waves and vegetation. The results from these studies also aid in the development and design of proper ground truth measurement systems.

Development of Measurement Tools

One important aspect in the study of remote sensing is the design of measurement tools to perform ground truth measurements.

Ground based scatterometers

Ground based scatterometer systems are popular methods for the collection of backscattering data from agriculture vegetation such as paddy and oil palm. Due to its importance, the development of ground based radar is as important as airborne SAR. Koo *et al*. [38] reported the development of a ground based radar for scattering measurements operating at C-band. Constructed from a combination of commercially available components and in-house fabricated circuitry, the system has full polarimetric capability for determining the complete backscattering matrix of a natural target. A microwave sensor was constructed and installed onto a boom truck (Fig. 9). Designed for short-range operations, a frequency-modulated (FM-CW) configuration was employed for the scatterometer system. Table 2 summarizes the system's specifications.

Figure 9. A photograph of the scatterometer system.

Figure 10 illustrates the simplified system block diagram, where the main sections are the RF section, the antenna, the IF section and the data acquisition unit. The system was tested in a low reflection outdoor environment [38]. The results from the measurements in the tests were compared with the theoretical values to evaluate the measurement accuracy.

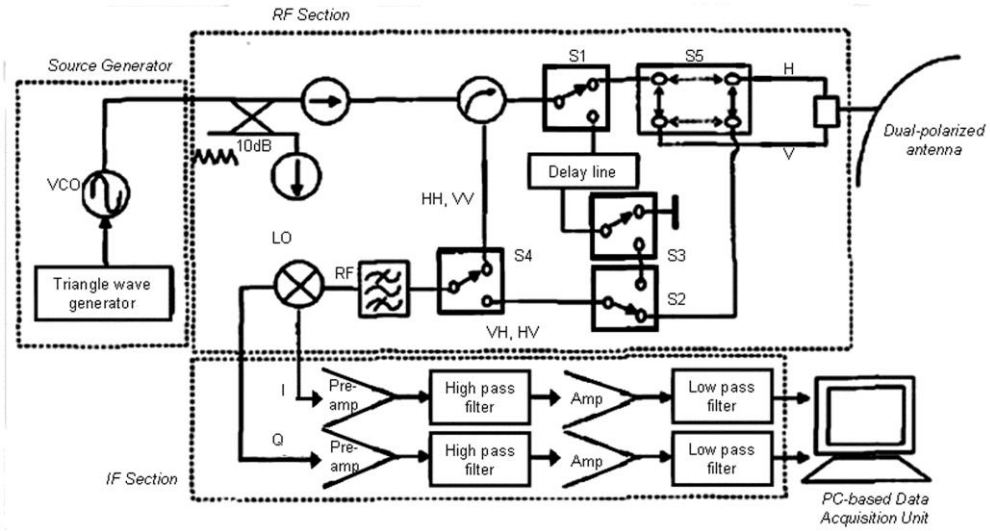

Figure 10. The system block diagram [38].

Figure 11 shows one of the RCS measurement carried out. In general, it was observed that the measured scattering matrices had good agreement with the theory and the measurement accuracy was within ±1.5 dB in magnitude and ±10 ° in phase. The scatterometer system has been used to conduct in-situ backscattering measurements of tropical crops.

Table 2. Specifications of ground based scatterometer [38].

System Parameter	Specification
System Configuration	
Type	FM-CW
Operating frequency, f_c	6 GHz (C-band)
Operating wavelength, λ	5 cm
Sweep Bandwidth, B	400 MHz
Modulating frequency, f_m	60 Hz
Polarization	HH, VV, HV, VH
Polarization isolation	35 dB
Antenna gain, G	35 dB
Antenna 3 dB beamwidth, β	3 °
Best possible range resolution, v_R	0.375 m
Platform	Boom truck
Platform height, h	25 m (vertical)
Measurement Capability	
Transmitter power, P_t	10 dBm
Received power, P_r	–15 dBm to –92 dBm
$\sigma°$ Dynamic range	+20 dB to –40 dB
Measurement range, R	20 m to 100 m
Incident angle coverage, θ	0 °– 70 °
Minimum signal-to-noise ratio, SNR	10 dB
Effective range resolution, ΔR	(~1.8 m at θ = 45 °; 4.5 m at θ = 60 °)

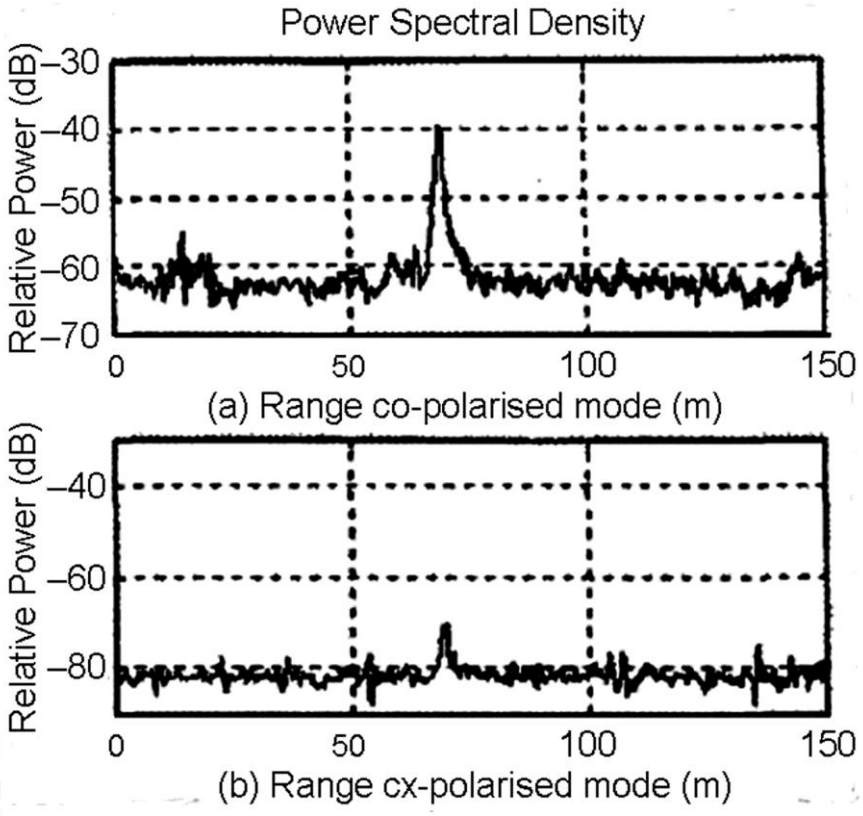

Figure 11. The measured power spectra of an 8" trihedral corner reflector [38].

There has also been a multitude of other developed ground based scatterometers utilized for the remote sensing of tropical vegetation, in particular rice crops. In [39, 40], an FM-CW scatterometer with four parabolic antenna (L, S, C, X) configurations was designed and utilized to collect microwave backscatter signatures of paddy over the entire rice-growing season. An X-band scatterometer system named POSTECH Polarimetric Scatterometer (POPOS) was designed and implemented by *Kim et al*. [41] to obtain radar backscattering measurements of rice crops over the whole period of rice growth at three polarization combinations.

The experience and success in the design and implementation of various types of ground based scatterometers gives rise to the confidence to develop airborne SAR systems.

Airborne SAR

There has been reported work on the development of airborne synthetic aperture radars. Koo *et al*. [42] developed the Malaysian Airborne Synthetic Aperture Radar (MASAR) for the purpose of earth resource monitoring, such as paddy fields, oil palm and soil surface. This SAR system is a C-band, single polarization, linear FM radar. The preparatory studies on the conceptual design of the microwave system were presented by Chan *et al*. [43]. The SAR system is capable of operating at moderate altitudes with low transmit power and small swath width.

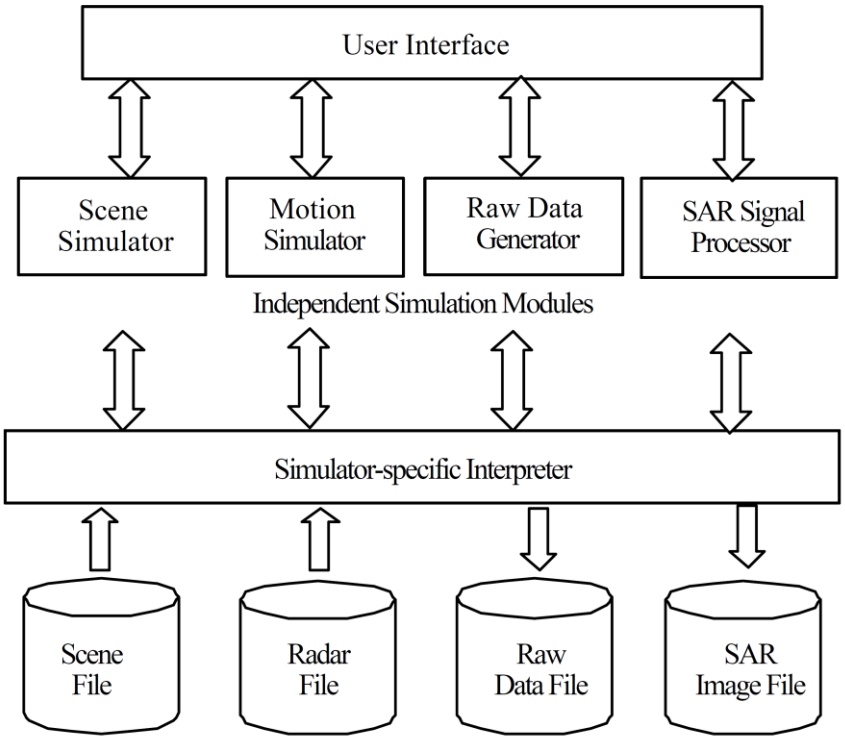

Figure 12. Block diagram of a modular-based SAR simulator [42].

The first step towards the design of the MASAR system is the model simulation carried out to select design parameters crucial towards the optimization of the hardware and software system performance. This was done by developing a modular-based simulator consisting of several independent modules sharing a pool of data files (Fig. 12) and implementing it using Matlab software. The design parameters were then iteratively selected and the results were evaluated using the SAR simulator. Table 3 presents the selected system parameters for the MASAR system.

Table 3. The MASAR specifications [42].

System Parameter	Specification
Mode of operation	Stripmap
Operating frequency, f_c	5.3 GHz (C-band)
Bandwidth, B	20 MHz
Chirp pulse duration, τ_p	20μs
Pulse repetition frequency	1000 HZ
Transmitter peak power, P_t	100 W
Polarization	Linear, VV
Antenna gain, G	>18 dBi
Elevation beamwidth, β_{el}	24 °
Azimuth beamwidth, β_{az}	3 °
Synthetic aperture length	~200 m
ADC sampling frequency	100 MHz
ADC quantization	12-bit
Data rate, d	100 Mbps
Recorder capacity	2 × 160 GB, SATA
Data take duration, T_d	>5 hours
$\sigma°$dynamic range	0 dB to –30 dB
Signal-to-noise ratio, SNR	>10 dB
Best slant range resolution	7.5 m
Best azimuth resolution, ρ_a	7.5 m (2-looks)
Incident angle, θ	50 °
Swath width, W	~8 km
Platform height, h	7500 m
Nominal platform speed, v_0	100 m/s
Operating platform	Pressurized aircraft

The functional block diagram for the MASAR system (Fig. 13) consists of a microstrip antenna, a radar electronics subsystem and a data acquisition system [for details, see [42]). A prototype RF transceiver for both ranged detection and radar cross section (RCS) measurement was also developed and verified in field experiments [44]. Finally, the algorithm for the MASAR image formation was developed based on the parallel implementation of the wavefront reconstruction theory, known as the range-stacking algorithm. The range-stacking algorithm does not require interpolation and does not suffer from truncation errors.

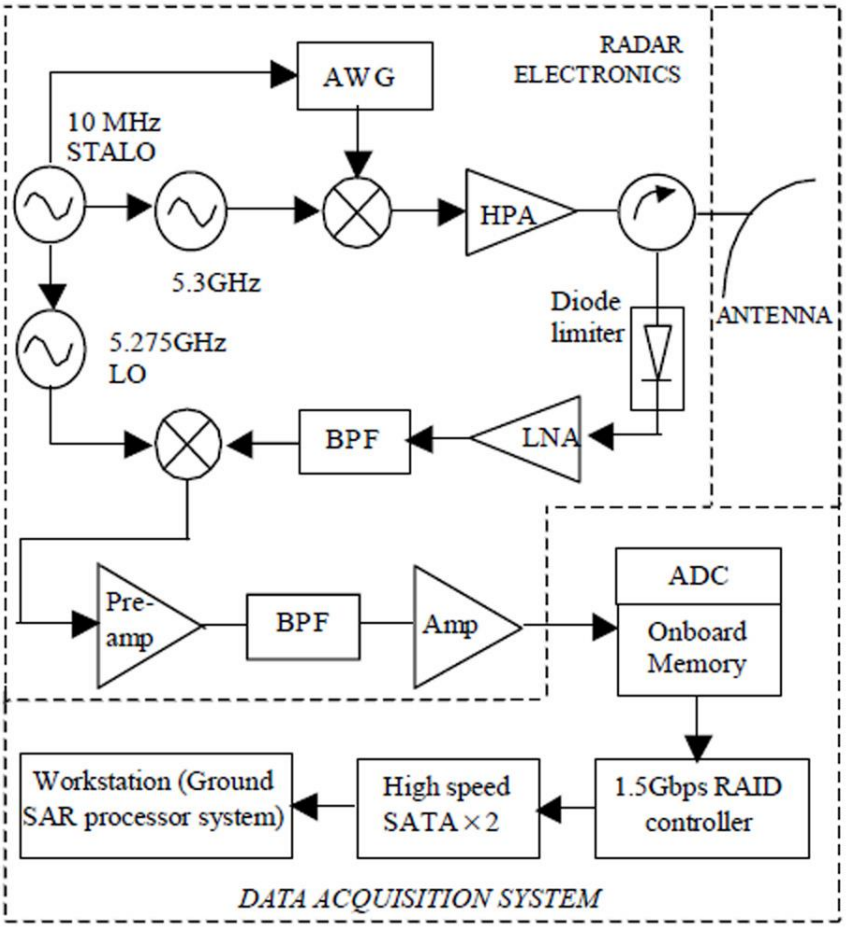

Figure 13. System block diagram of MASAR [42].

The MASAR project is an on-going activity and work is being done to mount the SAR system onto an unmanned aerial vehicle for flight commissioning and actual field measurements.

Anechoic Chamber

The potential to conduct controlled laboratory experiments to perform various electromagnetic field measurements has led to the design and construction of an anechoic chamber at Multimedia University, Cyberjaya, Malaysia [45]. While yet to be implemented on tropical vegetation, there is huge potential to utilize this facility in the future to conduct such experiments in a controlled environment. In order to design a good anechoic chamber, Chung *et al*. [46] performed the necessary modeling of anechoic chamber using a variant of the beam tracing technique to study the normalized site attenuation (NSA) performance of the anechoic chamber. In addition, work was also done to develop a model for the pyramidal RF absorber with pyramid length shorter than a quarter wavelength and poor reflectivity performance [47].

The structure of the anechoic chamber is a quarter-section geodesic dome, with a 12 foot radius and raised three feet above the floor [48]. Figure 14 shows the floor plan of the anechoic chamber, which can be used for monostatic and bistatic radar cross section measurements. Figure 15 shows the measurement system configuration, where two six-pole RF

switches select the transmitting antenna and the receiving antenna to be used in a particular measurement. The main component of the measurement system is the Wiltron 360B Vector Network Analyzer (VNA).

The calibration of the measurement system was then performed to remove systematic errors due to the frequency response of the hardware, source-impedance matching, continuity of the transmission line and residual echo from the chamber background. The equation for the scattering cross section is written as:

$$\sigma_{A(t\,\mathrm{arg}et)} = \frac{S_{11M(t\,\mathrm{arg}et)} - E_D}{E_R} \qquad (3)$$

where σ_A is the actual scattering cross section; E_D, the directivity error; S_{11M}, the measured reflection coefficient; and E_R, the reflection tracking error. The measurement accuracy of the system was then investigated. Figure 16 shows the frequency-domain response. It was found that the measurement error was within ±0.5 dB across the frequency range from 2 to 16 GHz.

Future work with anechoic chamber includes scattering measurement on young tropical trees such as rubber and oil palm.

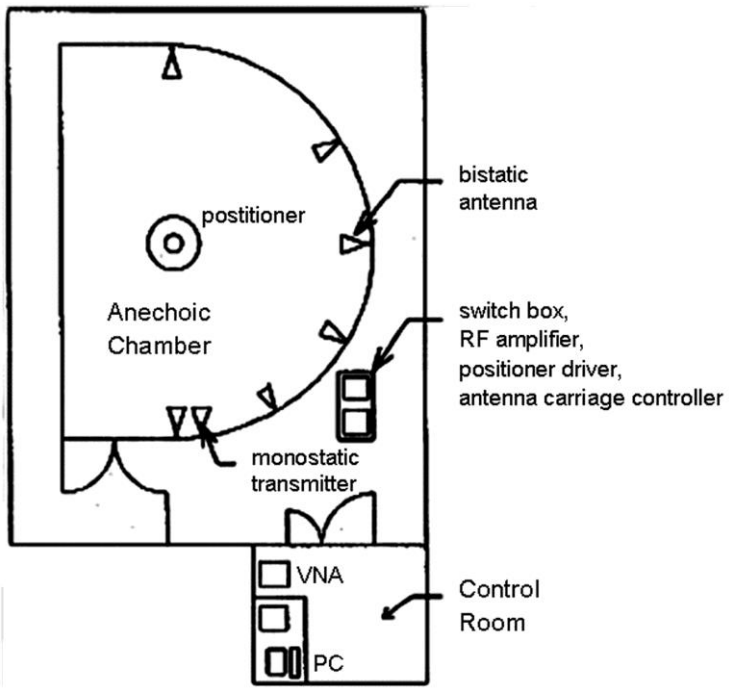

Figure 14. The anechoic chamber floor plan [48].

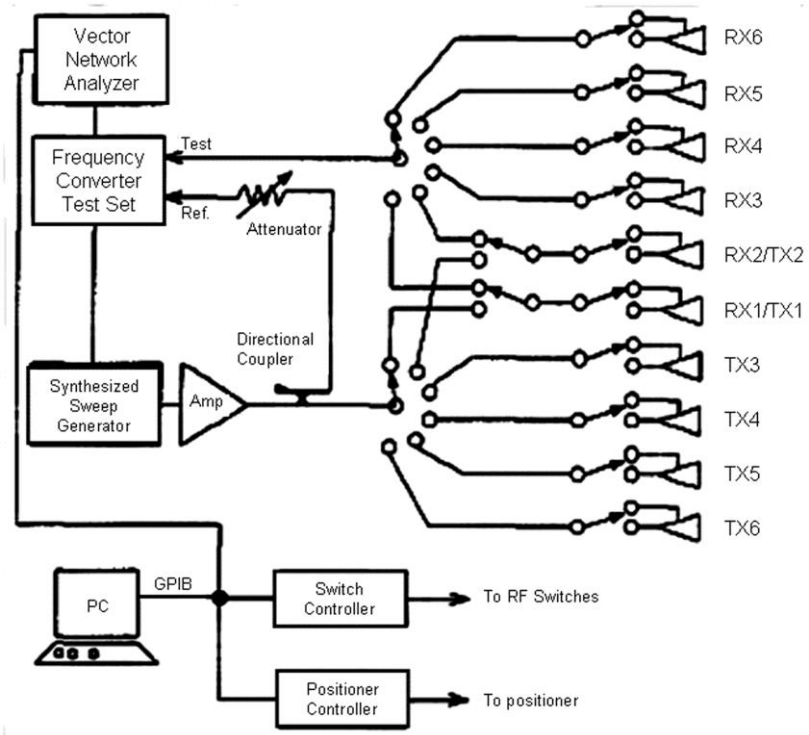

Figure 15. The measurement-system configuration [48].

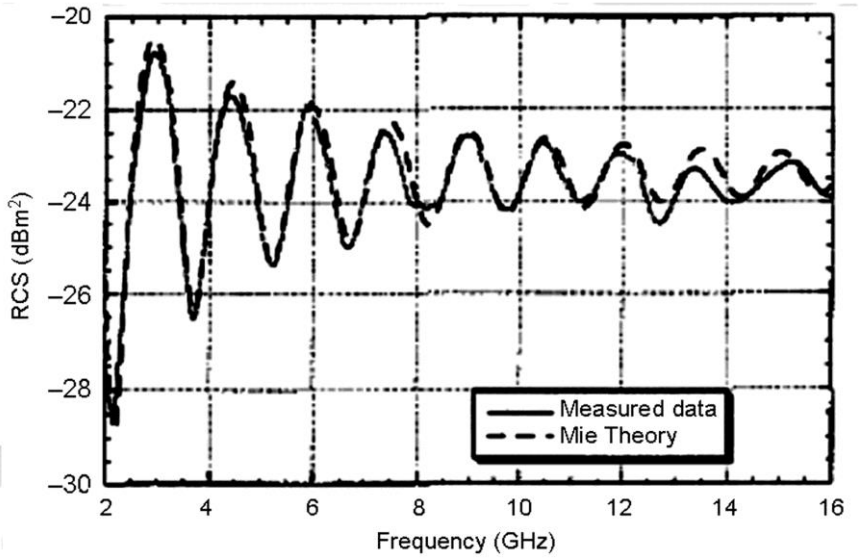

Figure 16. A comparison between the measured and theoretical frequency behaviour of the monostatic RCS of a 3" sphere after time-domain gating [48].

Moisture sensors

Moisture sensors are important measurement tools as they can provide parameter inputs to the developed theoretical models. The data collected from these sensors are also useful to verify the results obtained from theoretical models as well. The dielectric properties of a non-magnetic material play an important role in the interaction with electromagnetic waves. Understanding this importance, Khalid *et al*. [49] proposed the

development of planar microwave moisture sensors. In the study, the close relationship between moisture content and dielectric properties for both hevea rubber latex and oil palm fruits were investigated.

The attenuation of the microstrip sensor against the moisture content for hevea latex and for various thickness of protective layer is shown in Figure 17. The deviation of the test result of the moisture parameter is less than 1% compared to that obtained by Standard Gravimetric method. The microstrip sensor was integrated into the designed ripeness indicator prototype for oil palm fruits (Fig. 18). The detected current from the meter is related to the moisture content of mashed mesocarp and finally the stage of the ripeness can be determined.

A dual frequency sensor was also developed to measure moisture content of the rubber latex. The design is based on the measurement of magnitudes of the near field reflection at two frequencies in the X-band, 8.48 and 10.69 GHz. The design also replaces the conventional open horn antenna with microstrip radiating patches. This construction makes the sensor more versatile and compact and removes the temperature effect on moisture content measurements without involving phase measurement. A calibration equation was then found that instantly gives moisture content of the samples using the developed sensors. The system was tested using rubber latex and had predicted moisture content with a standard error of less than ± 0.4% compared to standard oven drying techniques and a mean error of less than ±1.3% in the temperature range of 25 ℃ to 60 ℃. The prototype version of the dual-frequency moisture meter is shown in Figure 19. Future consideration for this work is to expand the method to construct moisture sensors for other products such as palm oil.

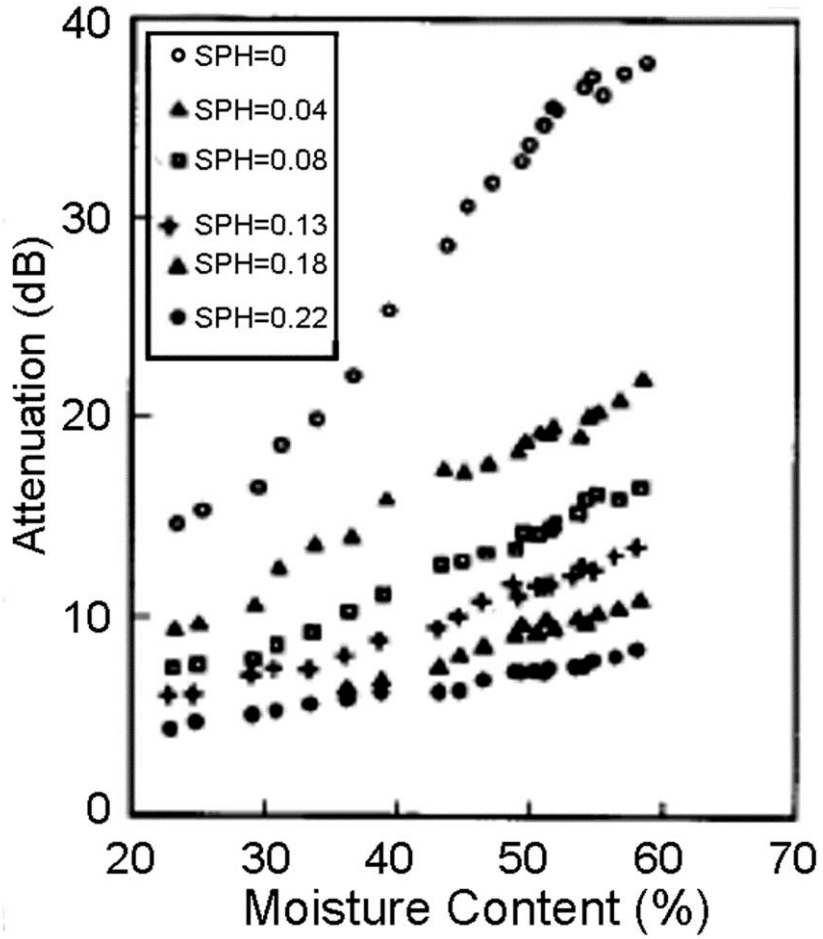

Figure 17. Variation of attenuation or insertion loss with moisture content for microstrip sensors [49].

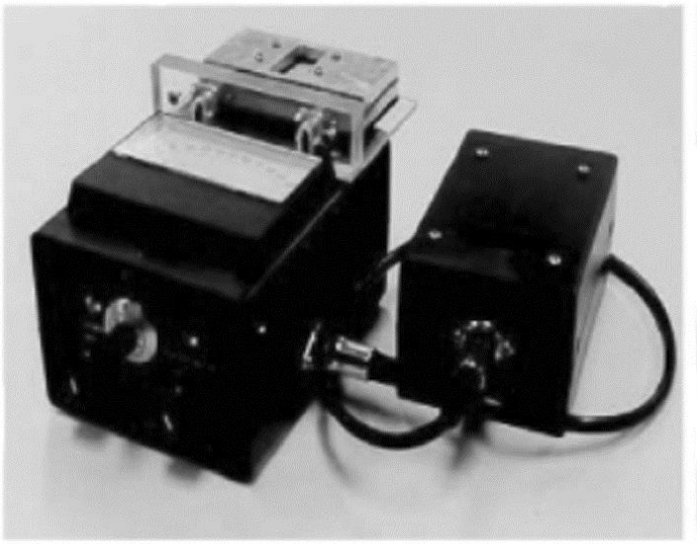

Figure 18. A prototype of ripeness meter for oil palm fruit [49].

Figure 19. A prototype model for dual-frequency microwave liquid moisture meter [49].

The development of various ground truth measurement systems and sensors has allowed researchers to conduct year long measurements at various sites.

Measurement Data Collection

The collection of various parameters from tropical vegetation is essential towards the validation of theoretical models and image classification techniques for microwave remote sensing and also for future references. Most parameters can be obtained directly through simple measurements, such as plant height, trunk diameter and circumference, leaf length, etc. Other parameters however may require the use of equations from various theoretical models to calculate. As such, the development of such models is important as they indirectly contribute towards the application of remote sensing for earth terrain monitoring. In addition, there are also plenty of measurement data collected via different techniques on tropical vegetation. Some of these measurements were carried out for the entire growth cycle of the plants and may provide crucial data for the remote sensing of such media.

Dielectric constant is an important biophysical parameter that plays a crucial role in the validation of theoretical models and the development of yield prediction models for tropical crops. Chuah *et al*. [50] explored the accuracy of two theoretical models that were used to estimate the dielectric constants of leaves from two tropical crops (rubber and oil palm) as a function of moisture content at X-band. The models being studied were the simple dielectric theory by Fung and Fung [51] and the dual-dispersion model by Ulaby and El-Rayes [52]. Utilizing the waveguide thin sheet technique to measure the dielectric constant of the leaves, they were able to successfully evaluate the performance of both models. It was found that the dual-dispersion model gave a more accurate estimation of the dielectric constants and thus confirmed its applicability to the leaves of rubber and oil palm in future research work.

Other parameters important towards yield prediction models and growth assessment are above ground biomass (AGB) and stem volume. Previous works measured oil palm biomass and stem volume from mature oil palm by destructive sampling which involved weighing all the major components of biomass and stem volume for different ages [53].

These studies extrapolated the data from the destructive measurements on a few palms from each age group, but the procedure might be underestimated due to restricted sampling areas. In addition, the method is tedious and time consuming.

Asari *et al*. [54] proposed the measurement of the parameters using the non-destructive sampling as a preliminary study towards the development of a prediction model for the estimation of oil palm above ground biomass and stem volume using remote sensing data. The main aim of the study was to estimate the two parameters at different ages using the non-destructive method and to study the relationship between oil palm biomass and several parameters such as crown width, height, the diameter of breast height, length and depth of petiole of oil palm stand. The study found that the trunk biomass contributed a major portion of the oil palm biomass, about 86 to 95% from the total AGB. The study also discovered that the age of the oil palm was directly correlated to above ground biomass, while stem volume was inversely correlated with the age of oil palm. A full scale study combining the ground information and remote sensing is being conducted.

Vegetation water content (VWC) plays a significant role in the retrieval of soil moisture from microwave remote sensing and also in forest and agricultural studies such as drought assessment and yield prediction. Kim *et al*. [55] reported that previous studies analyzed the relationship between NDVI and VWC and developed techniques to estimate VWC and other biophysical variables. They went a step further and examined the relationship between polarimetric radar data, VWC, LAI and normalized difference vegetation index (NDVI) using soybean and rice, focusing on the use of radar vegetation index (RVI) to estimate VWC. In order to perform the study, the backscattering coefficients for L-, C- and X-bands, vegetation indices (RVI, NDVI and LAI) and VWC were observed over rice and soybean growth cycles. Retrieval equations were then developed for estimating VWC using the RVI of both crops. The study concluded that L-band RVI was well correlated with VWC, LAI and NDVI compared to C- and X-band and thus achieved the most accurate VWC retrievals. It should be noted however, that the investigation only focused on a 40° single incidence angle observing system since this study would be employed on the NASA Soil Moisture Active Passive satellite (SMAP) in the future. As such further studies may explore the effects of the incidence and azimuth angles.

The measurement of radar backscatter data from paddy, especially over the entire growth cycle is also important towards the development of yield prediction models via remote sensing. There is a substantial amount of reported work on the radar measurements microwave backscattering coefficients of rice plants [39-41, 56]. In these papers, the measurements of the rice plants were carried out using constructed ground based scatterometers over multifrequency and multipolarization covering an entire rice growing season. The locations of the measurements covered areas in Japan, China and Korea. In addition, measurement of other parameters such as LAI, biomass, etc. were also performed on the paddy. While the earlier works performed radar measurements using ground based scatterometers, the attempts to use space borne satellites for such measurements are few. Kurosu *et al*. [19] presented their measurements on monitoring rice crop growth from space using the European Remote Sensing satellite 1 (ERS-1). The SAR measurements were performed at

the rice fields of Akita Prefectural College of Agriculture covering two growing seasons in 1992 and 1993 and were the first attempt to monitor rice crop growth from space covering all growth stages.

Tropical forest biomass estimation is important for global research. Such correlation analysis forms the base for developing models and techniques to estimate tropical forest biomass from remote sensing data. Yang *et al*. [57] utilized LANDSAT TM data and the biomass data collected from main tropical forest vegetation types in Xishuangbanna, China for studying the correlations between the biomass of vegetation types. The study found that the relationships between the biomass of monsoon tropical forest and LANDSAT TM6 and TM7 were the strongest. TM6 was positively and significantly (at 95% level of confidence) related to forest biomass while TM7 was inversely and significantly (at 95% level of confidence) related to forest biomass. Lastly, the LANDSAT TM was observed to be not significantly (at 95% level of confidence) related to the forest biomass for both the mountainous tropical forest and the seasonal ever-green broadleaf forest.

IMAGE PROCESSING TECHNIQUES FOR THE REMOTE SENSING OF TROPICAL VEGETATION

Remote sensing has proved to be an extremely convenient method to monitor large areas of agriculture crops or forests. The use of SAR images from airborne or space borne radar allows the coverage of large areas and provides huge amount of information. Image processing thus plays a crucial role, as it is important for researchers to be able to differentiate between areas of interest from other landscape captured within the image. The proper image processing tool will be required in order to correctly analyze the image and highlight the areas of interest.

Chuah *et al.* [1] reported the use of fractal dimension of images as an additional input to a neural network classifier to classify different areas of interest. Preliminary results showed that fractal analysis was useful towards the classification of sea, urban, forested and paddy areas. Ouchi *et al*. [58] explored the comparison between the use of optical and radar images on the classification of mangrove, virgin forests and oil palm plantation with the ground truth data collected from the field survey. Visible and infrared images were acquired using MOS-1b, while SAR images from JERS-1 at L-band and ERS-2 at C-band were also obtained.

The optical images were capable of classifying deforestation areas, but applications to mangrove forests were limited. SAR images performed better and were capable of differentiating the mangrove from virgin forests [58]. It was concluded that due to the longer penetration depth of L-band, the JERS-1 performed better than the ERS-2, even though both the mangrove and virgin forests had similar biomass well above the saturation range of the L-band RCS. The top image in Figure 20 shows the 3-look image of the Sematan test site in 1993, with the difference in intensity between the mangrove and neighbouring virgin forests about 6dB, making it possible to extract the mangrove area. The classified image is shown in the middle of Figure 24 and shows good agreement with the OS (Ordnance Survey) map at the bottom. The reason in the difference in intensity is associated with whether the ground is covered by water or undergrowth, which is supported by the difference in image intensity between dry and wet seasons. Lastly, the study also showed that

the ability to monitor palm oil trees is limited to the early stages of plantation.

The use of SAR images in L-band and C-band for the purpose of rice mapping and monitoring has been carried out by various research groups. Zhao *et al*. [59] carried out a study on rice monitoring using ENVISAT ASAR data over a period of three years in Jiangsu Province of China. The study showed that multi-temporal and multi-polarization radar data have great advantages in rice mapping and also parameter inversion. A practical scheme for rice yield estimation has been put forward, but further studies will need to be performed to improve its accuracy.

Yamada [60] investigated the relations between ground features and mathematical morphology using JERS-1 data during flooding time in paddy areas. The study was to improve on classification of flood areas from paddy fields or floating rice growing regions. Applying computational mathematical morphology to flood extent recognition showed promising results, with improved differentiation between paddy field areas, river courses and irrigation canals and human activity areas.

The classification of rice and sugarcane from other cover types such as water, urban areas, bush and scrubs using ERS-1 and JERS-1 satellites in Kanchanaburi, Thailand was explored [61]. Using qualitative and quantitative measures to investigate the separability of different cover types, results showed that the use of at least two appropriately timed imaging dates during the growing season was sufficient for rice field inventory. However, the study also showed difficulty in discriminating sugarcane from shrubs using the SAR images.

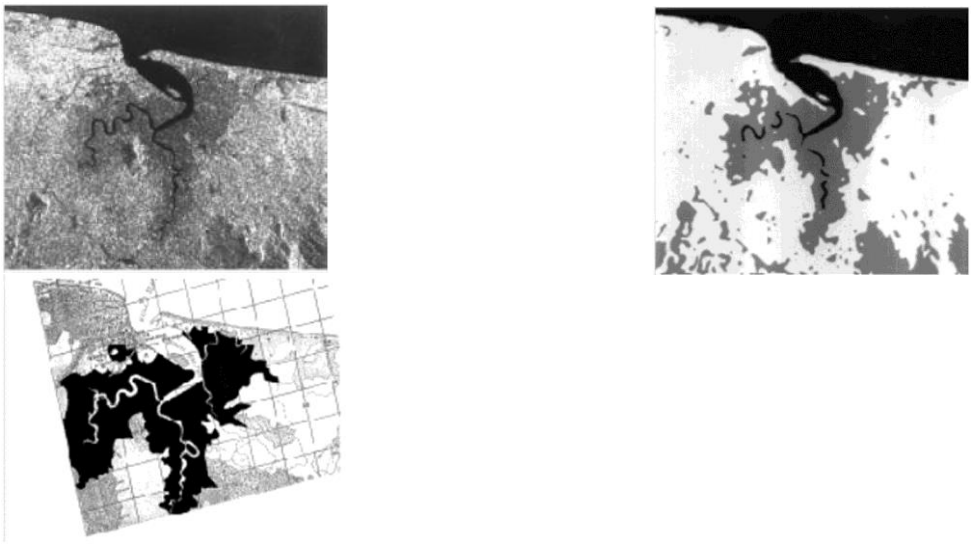

Figure 20. JERS-1 SAR image of the Sematan mangrove and surrounding forests (left), classified image (centre) and OS (Ordnance Survey) map (right) [58].

Several projects using image classification and mapping on tropical forests were also carried out. A joint research between Malaysia and Japan developed a monitoring system for tropical rain forest management [6]. The study was divided into three main areas: characteristics of high resolution remote sensing sensors such as LANDSAT TM, SPOT HRV and MOS-1, the study of global forest environment using NOAA AVHRR, where NOAA GAC data were used to estimate the surface

temperature and evapotranspiration of Peninsula Malaysia, and zoning technology using a combination of a GIS system with remote sensing data processing system for managing tropical forest environment. Another similar project, where remote sensing was used to extract environmental information of a tropical mountainous forest was carried out in a National Park in Vietnam [62]. Parameters crucial towards the management of the mountainous forest, such as wetness, groundwater conditions, geological structure and land cover changes were successfully extracted by application of remote sensing and GIS analysis. The Central Africa Mosaic project (CAMP) also studied the use of ERS-1 images for the purpose of tropical vegetation monitoring, combining the use of thematic interpretation, data processing and new initiatives for large scale radar maps [63].

The use of image processing techniques together with SAR images to estimate different forest parameters were also researched. Foody *et al*. [64] proposed the use of neural networks to estimate the diversity and composition of a Bornean tropical rain forest using Landsat TM data. In the study, a feedforward neural network was applied to estimate species richness while a Kohonen neural network was used to provide information on species composition. Another study focused on soil moisture estimation using a remote sensing algorithm from LANDSAT TM, ETM and ENVISAT images [65]. Preliminary results show that the empirical model used to estimate soil moisure had a poor agreement with the measured values. As such, further exploration into the model is necessary.

Tropical forest carbon stock and biomass are important parameters in forest management. Yang *et al*. [66] explored the possibility to estimate carbon stock of tropical forest vegetation using LANDSAT TM data and GIS data. A model to estimate biomass was formulated with the data of forest fixed samples, GIS and LANDSAT TM images. Finally the carbon stock was created from the biomass calculated using the above model. The model has been found to be effective. Williams *et al*. [67] proposed recovering tropical forest biomass from GeoSAR observations. The airborne GeoSAR collects X-band and P-band InSAR data simultaneously. It was shown that GeoSAR X-P interferometric data alone may be used to recover tropical forest biomass, removing any ambiguity associated with variation in ground conditions.

CONCLUSION

Remote sensing has been applied to tropical vegetation, both in agriculture and forestry. The problem of remote sensing of vegetation can be divided into three main categories: development of theoretical models, ground truth measurement techniques, and equipment and image processing.

There has been a multitude of scattering models developed to understand the interaction between tropical vegetation and electromagnetic waves. The use of Radiative Transfer theory is highly popular, though there are other theories being utilized as well. Several variations to the RT model are the multilayer model, DMPACT and Fresnel corrections, combination with the Lindenmayer System and also the Vector Radiative Transfer model. These extensions sought to improve

on the accuracy of backscatter predictions and serve as the basis for the future development of inversion models.

The design and study of equipment to carry out measurements are needed to obtain ground truth data from vegetation for the purpose of model validation. There are research groups focusing on the development of ground based and airborne scatterometers and SAR. An anechoic chamber was also designed by a research team in MMU, Cyberjaya, Malaysia, while moisture sensors have also been looked into. Lastly, there is also research on image processing to improve on image classification from spaceborne and airborne images to distinguish between different vegetation types and other land areas.

There is still much work to be done on all areas in order to develop more accurate techniques for the remote sensing of tropical vegetation.

Acknowledgement – The authors would like to thank Advanced Agriecological Research Sdn Bhd (AAR), Universiti Tunku Abdul Rahman (UTAR) and the Ministry of Science, Technology and Innovation of Malaysia (MOSTI) for their support in the project.

REFERENCES

1. Chuah H.T. (1997) An Overview of Microwave Remote Sensing Research at the University of Malaya, Malaysia. *Proceedings of IEEE International Geoscience and Remote Sensing Symposium* **3**: 1421–1423.
2. Golden, K.M.; Borup, D.; Cheney, M.; Cherkaeva, E.; Dawson, M.S.; Kung-Hau Ding; Fung, A.K.; Isaacson, D.; Johnson, S.A.; Jordan, A.K.; Jin An Kon; Kwok, R.; Nghiem, S.V.; Onstott, R.G.; Sylvester, J.; Winebrenner, D.P.; Zabel, I.H.H. (1998) Inverse Electromagnetic Scattering Models for Sea Ice. *IEEE Transactions on Geoscience and Remote Sensing* **36(5)**: 1675–1704.
3. Fernandez D.E.; Chang P.S., Carswell J.R., Contreras R.F. and Frasier S.J. (2005) IWRAP: The Imaging Wind and Rain Airborne Profiler for Remote Sensing of the Ocean and the Atmospheric Boundary Layer Within Tropical Cyclones. *IEEE Transactions on Geoscience and Remote Sensing* **43(8)**: 1775–1787.
4. Guerif M., Launay M. and Duke C. (2000) Remote sensing as a tool enabling the spatial use of crop models for crop diagnosis and yield prediction. *Proceedings of IEEE International Geoscience and Remote Sensing Symposium* **4**: 1477–1479.
5. Lelong C.C.D., Roger J.-M., Bregand S., Dubertret F., Lanore M., Sitorus N.A., Raharjo D.A. and Caliman J.-P. (2009) Discrimination of Fungal Disease Infestation in Oil-Palm Canopy and *Hyperspectral Reflectance Data. Proceedings of First Workshop on Hyperspectral Image and Signal Processing: Evolution in Remote Sensing*: 1–4.
6. Sawada H., Nakakita O., Awaya Y., Hamzah K.A. and Hassan A. (1991) Development of Monitoring System for Tropical Rain Forest Management in the Peninsula Malaysia: The Joint Malaysia-Japan Research Project on Remote Sensing. *Proceedings of IEEE International Geoscience and Remote Sensing Symposium: Remote Sensing: Global Monitoring for Earth Management* **3**: 1153–1156.
7. Koay J.Y., Tan C.P., Lim K.S., Saiful Bahari A.B., Ewe H.T., Chuah H.T. and Kong J.A. (2007) Paddy Fields as Electrically Dense Media: Theoretical Modeling and Measurement Comparisons. *IEEE Transactions on Geoscience and Remote Sensing* **45(9)**: 2837–2849.

8. Yueh S. H., Kong J. A., Jao J. K., Shin R. T. and Le Toan T. (1992) Branching Model for Vegetation," *IEEE Transactions on Geoscience and Remote Sensing* **30(2)**: 390–402.
9. Tsang L., Ding K. H., Zhang G., Hsu C. C. and Kong J. A. (1995) Backscattering Enhancement and Clustering Effects of Randomly Distributed Dielectric Cylinders Overlying a Dielectric Half Space based on Monte-Carlo Simulations. *IEEE Transactions on. Antennas and Propagation* **43(5)**: 488–499.
10. Chuah H.T, Tjuatja S., Fung A.K. and Bredow, J.W. (1996) A Phase Matrix for a Dense Discrete Random Medium: Evaluation of Volume Scattering Coefficient. *IEEE Transactions on Geoscience and Remote Sensing* **34(5)**: 1137-1143.
11. Ewe H.T. and Chuah H.T. (2000). Electromagnetic Scattering from an Electrically Dense Vegetation Medium. *IEEE Transactions on Geoscience and Remote Sensing* **38(5)**: 2093-2105.
12. Fung A. K. and Chen M. F. (1987) Fresnel Field Interaction Applied to Scattering from a Vegetation Layer. *Remote Sensing of Environment*. **23(1)**: 35–50.
13. Ewe H. T. and Chuah H. T. (2000) A Study of Fresnel Scattered Field for Nonspherical Discrete Scatterers. *Progress in Electromagnetics Research* **25**: 189–222.
14. Fung A.K. (1994) *Microwave Scattering and Emission Models and Their Applications*. Artech House, Norwood, Massachusetts.
15. Chandrasekhar S. (1960) *Radiative Transfer*. Dover, New York.
16. Ulaby F. T., Moore R. K. and Fung A. K. (1982) *Microwave Remote Sensing: Active and Passive, Vol. II*. Artech House, Norwood, Massachusetts.
17. Karam M. A., Fung A. K., Lang R. H. and Chauhan N. S. (1992) A Microwave Scattering Model for Layered Vegetation. *IEEE Transactions on Geoscience and Remote Sensing* **30(4)**: 767–784.
18. Le Toan T., Ribbes F., Wang L. F., Floury N., Ding K. H., Kong J. A., Fujita M. and Kurosu T. (1997) Rice Crop Mapping and Monitoring Using ERS-1 Data Based on Experiment and Modeling results. *IEEE Transactions on Geoscience and Remote Sensing* **35(1)**: 41–56.
19. Kurosu T., Suitz T., and Moriya T. (1995) Monitoring of Rice Crop Growth from Space using ERS-1 C-Band SAR," *IEEE Transactions on Geoscience and Remote Sensing* **33(4)**: 1092–1096.
20. Koay J.Y., Ewe H.T. and Chuah H.T. (2008) A Study of Fresnel Scattered Fields for Ellipsoidal and Elliptic-Disk-Shaped Scatterers. *IEEE Transactions on Geoscience and Remote Sensing* **46(4)**: 1091–1103.
21. Ma H.B., Zeng Q.M., Ma A.N. and Zhang T. (2000) Simulation and Analysis for the Microwave Backscattering Coefficient of Rice. *Proceedings of IEEE International Geoscience and Remote Sensing Symposium* **2**: 369–371.
22. Ulaby F.T., Sarabandi K., MacDonald K., Whitt M., and Dobson M. C. (1990) Michigan Microwave Canopy Scattering Model. *International Journal of Remote Sensing* **11**, 1223–1253.
23. Shao Y., Liao J.J, Fan X.T. and Wang Y.H. (2002) Analysis of Temporal Backscatter of Rice: A Comparison of RADARSAT Observations with Modeling Results. *Proceedings of IEEE International Geoscience and Remote Sensing Symposium: Remote Sensing* **1**: 478–480.
24. Sun G., Simonett D., and Strahler A. (1991) A Radar Backscatter Model for Discontinuous Coniferous Forests. *IEEE Transactions on Geoscience and Remote Sensing* **29(4)**: 639–650.

25. Ulaby F. T. and El-Rayes M. A. (1987) Microwave Dielectric Spectrum of Vegetation-Part II: Dual-Dispersion Model. *IEEE Transactions on Geoscience and Remote Sensing* **GE-25(5)**: 550–557.
26. Fortuny-Guasch J., Martinez-Vazquez A., Riccio D., Lopez-Sanchez J.M. and Ballester J.D. (2003) Experimental Validation of an Electromagnetic Model for Rice Crops Using a Wide-Band Polarimetric Radar. *Proceedings of IEEE International Geoscience and Remote Sensing Symposium* **4**: 2866–2868.
27. Ma H.B., Zeng Q.M., Ma A.N. (2000) Backscattering Model for Crops Based on L-system and Coherent Addition of Scattered Field. *Proceedings of IEEE International Geoscience and Remote Sensing Symposium* **2**: 907–909.
28. Lindenmayer A. (1968) Mathematical Models for Cellular Interaction in Development, I and 11. *Journal of Theoretical Biology* **18**: 280–315.
29. Liao J.J, Guo H.D. and Shao Y. (2002) Modeling of Microwave Dielectric Properties of Rice Growth Stages in Zhaoqing Test Site of Southern China. *Proceedings of IEEE International Geoscience and Remote Sensing Symposium* **5**: 2620–2622.
30. Zhang Y., Huang H., Chen X. and Wu J. (2008) Mapping Paddy Rice Biomass Using ALOS/PALSAR Imagery. *Proceedings of 2008 International Workshop on Education Technology and Training & 2008 International Workshop on Geoscience and Remote Sensing* **2**: 207–210.
31. Wang C., Wu J., Zhang Y., Qi J. and Salas W.A. (2009) Characterizing L-Band Scattering of Paddy Rice in Southeast China with Radiative Transfer Model and Multitemporal ALOS/PALSAR Imagery," *IEEE Transactions on Geoscience and Remote Sensing* **47(4)**: 988–998.
32. Durden S.L., Morrissey L.A. and Livingston G.P. (1995) Microwave Backscatter and Attenuation Dependence on Leaf Area Index for Flooded Rice Fields. *IEEE Transactions on Geoscience and Remote Sensing* **33(3)**: 807–810.
33. Inoue Y., Dabrowska-Zielinska K., Kurosu T., Maeno H., Uratsuka S. and Kozu T. (2001) Interactions between Multi-Frequency Microwave Backscatters and Rice Canopy Variables. *Proceedings of IEEE International Geoscience and Remote Sensing Symposium: Remote Sensing* **3**: 1270–1272.
34. Izzawati, Lewis P. and McMorrow J. (1998) 3D Model Simulation of Polarimetric Radar Backscatter and Texture of An Oil-Palm Plantation. *Proceedings of IEEE International Geoscience and Remote Sensing Symposium* **3**: 1502–1504.
35. Sun G. and Ranson K.J. (1995) A Three-Dimensional Radar Backscatter Model of Forest Canopies. *IEEE Transactions on Geoscience and Remote Sensing* **33(2)**: 372–382.
36. Chauhan N.S., Lang R.H. and Ranson K.J. (1991) Radar Modeling of a Boreal Forest. *IEEE Transactions on Geoscience and Remote Sensing* **29(4)**: 627–638.
37. Thirion L., Colin E. and Dahon C. (2006) Capabilities of a Forest Coherent Scattering Model Applied to Radiometry, Interferometry, and Polarimetry at P- and L-Band. *IEEE Transactions on Geoscience and Remote Sensing* **44(4)**: 849–862.
38. Koo V.C., Chung B.K. and Chuah H.T. (2003) Development of a Ground-Based Radar for Scattering Measurements. *IEEE Antennas and Propagation Magazine* **45(2)**: 36–42.
39. Xu C.L, Chen Y., Tong L., Jia M.Q., Liu Z.C. and Lu H.P. (2008) Measuring the Microwave Backscattering Coefficient of Paddy Rice Using FM-CW Ground-based Scatterometer. *Proceedings of 2008 International Workshop on Education Technology and Training & 2008 International Workshop on Geoscience and Remote Sensing* **2**: 194–198.

40. Zhao C.W, Chen Y., Tong L. and Jia M.Q., (2011) Multi-frequency and Multi-polarization Radar Measurements Over Paddy Rice Field and Their Relationship with Ground Parameters. *Proceedings of IEEE International Geoscience and Remote Sensing Symposium: Remote Sensing* **3**: 1958–1960.
41. Kim S.B., Kim B.W., Kong Y.K. and Kim Y.S. (2000) Radar Backscattering Measurements of Rice Crop Using X-Band Scatterometer. *IEEE Transactions on Geoscience and Remote Sensing* **38(3)**: 1467–1471.
42. Koo V.C., Chan Y.K., Gobi V., Lim T.S., Chung B.K. and Chuah H.T. (2005) The Masar Project: Design and Development. *Progress in Electromagnetics Research* **50**: 279–298.
43. Chan Y.K., Azlindawaty M.K., Gobi V., Chung B.K. and Chuah H.T. (2000) The Design and Development of Airborne Synthetic Aperture Radar. *Proceedings of IEEE International Geoscience and Remote Sensing Symposium* **2**: 518–520.
44. Chan Y.K., Chung B.K. and Chuah H.T. (2004) Transmitter and Receiver Design of an Experimental Airborne Synthetic Aperture Radar Sensor. *Progress in Electromagnetics Research* **49**: 203–218.
45. Chung B.K. and Chuah H.T. (2003) Design and Construction of a Multipurpose Wideband Anechoic Chamber. *IEEE Antennas and Propagation Magazine* **45(6)**: 41–47.
46. Chung B.K., Teh C.H. and Chuah H.T. (2004) Modeling of Anechoic Chamber Using a Beam-tracing Technique. *Progress in Electromagnetics Research* **49**: 23–38.
47. Chung B.K. and Chuah H.T. (2003) Modeling of RF Absorber for Application in the Design of Anechoic Chamber. *Progress in Electromagnetics Research* **43**: 273–285.
48. Chung B.K., Chuah H.T. and Bredow J.W. (1997) A Microwave Anechoic Chamber for Radar-Cross Section Measurement. *IEEE Antennas and Propagation Magazine* **39(3)**: 21–26.
49. Khalid K., Ghretli, M.M., Abbas Z. and Grozescu I.V. (2006) Development of Planar Microwave Moisture Sensors for Hevea RubberLatex and Oil Palm Fruits. *Proceedings of International RF and Microwave Conference*: 10–15.
50. Chuah H.T., Lee K.Y. and Lau T.W. (1995) Dielectric Constants of Rubber and Oil Palm Leaf Samples at X-Band. *IEEE Transactions on Geoscience and Remote Sensing* **33(1)**: 221–223.
51. Fung A.K. and Fung H.S. (1977) Application of First-Order Renormalization Method to Scattering from a Vegetation-Like Half-Space. *IEEE Transactions on Geoscience Electronics* **15(4)**: 189–195.
52. Ulaby F.T. and El-Rayes M.A., (1987) Microwave Dielectric Spectrum of Vegetation-Part 2: Dual-Dispersion Model," *IEEE Transactions on Geoscience and Remote Sensing* **25(5)**: 541–549.
53. Rees A.R. and Tinker P.B.H. (1963) Dry-Matter Production and Nutrient Content of Plantation Oil Palms in Nigeria. *Plant and Soil* **16(3)**: 350–363.
54. Asari N., Suratman M.N. and Jaafar J. (2011) Preliminary Study of Above Ground Biomass (AGB) and Stem Volume of Oil Palm Stands. *Proceedings of IEEE Symposium on Business, Engineering and Industrial Applications*: 65–70.
55. Kim Y.Y., Jackson T., Bindlish R., Lee H.Y. and Hong S.Y. (2012) Radar Vegetation Index for Estimating the Vegetation Water Content of Rice and Soybean. *IEEE Geoscience and Remote Sensing Letters* **9(4)**: 564–568.
56. Suitz, T., Kurosu, T. and Umehara, T. (1988) A Measurement Of Microwave Backscattering Coefficients Of Rice Plants. *Proceedings of*

IEEE International Geoscience and Remote Sensing Symposium **3**: 1283–1286.
57. Yang C.J., Zhou J.M., Huang H. and Chen X. (2007) Correlations of the Biomass of the Main Topical Forest Vegetation Types and LANDSAT TM Data in Xishuangbanna of P. R. of China. *Proceedings of IEEE International Geoscience and Remote Sensing Symposium*: 4336–4338.
58. Ouchi K. and Ipor I.B. (2002) Comparison of SAR and Optical Images of the Rainforests of Borneo, Malaysia with Field Data. *Proceedings of IEEE International Geoscience and Remote Sensing* Symposium **5**: 2905–2907.
59. Zhao X.Y, Yang S.B., Shen S.H. and Li B.B. (2011) Assessment of ENVISAT ASAR Data for Rice Monitoring Based on Three Years Experiments. *Proceedings of IEEE International Conference on Remote Sensing, Environment and Transportation Engineering*: 136–139.
60. Yamada Y. (2003) Relation between Ground Features and Mathematical Morphology Using JERS-1/SAR Data During Flooding Time in Paddy Areas. *Proceedings of IEEE International Geoscience and Remote Sensing Symposium* **4**: 2526–2528.
61. Paudyal D.R., Eiumnoh A. and Aschbacher J. (1995) Multitemporal Analysis of SAR Images Over the Tropics for Agricultural Applications. *Proceedings of IEEE International Geoscience and Remote Sensing Symposium* **2**: 1219–1221.
62. Hung L.Q. and Batelaan O. (2003) Environmental Geological Remote Sensing and GIS Analysis of Tropical Karst Areas in Vietnam. *Proceedings of IEEE International Geoscience and Remote Sensing Symposium* **4**: 2964–2966.
63. Malingreau J.P., De Grandi G.F., Leysen M., Mayaux P. and Simard M. (1997) The ERS-1 Central Africa Mosaic: A New Role for Radar Remote Sensing in Global Studies of the Tropical Ecosystem. *Proceedings of IEEE International Geoscience and Remote Sensing Symposium* **4**: 1725–1727.
64. Foody G.A. and Cutler M.E. (2002) Remote Sensing of Biodiversity: Using Neural Networks to Estimate the Diversity and Composition of a Bornean Tropical Rainforest from Landsat TM Data. *Proceedings of IEEE International Geoscience and Remote Sensing Symposium* **1**: 497–499.
65. Marrufo L., Gonzalez F., Monsivais-Huertero A. And Ramos J. (2011) Spatio-Temporal Estimation of Soil Moisture in a Tropical Region using a Remote Sensing Algorithm. *Proceedings of IEEE International Geoscience and Remote Sensing Symposium*: 3089–3092.
66. Yang C.J., Liu J.Y., Zhang Z.X. and Zhang Z.K. (2001) Estimation of the Carbon Stock of Tropical Forest Vegetation by Using Remote Sensing and GIS. *Proceedings of IEEE International Geoscience and Remote Sensing Symposium* **4**: 1672–1674.
67. Williams M.L., Milne T., Tapley I., Reis J.J., Sanford M., Kofman B. and Hensley S. (2009) Tropical Forest Biomass Recovery Using GeoSAR Observations. *Proceedings of IEEE International Geoscience and Remote Sensing Symposium* **4**: 173–176.

Appendix 2:

Development of Theoretical Model for Microwave Remote Sensing with Computational Electromagnetics

Stage 1:

In order to understand how basic and important scatterers in the medium contribute to the dominant scattering mechanisms that leads to final radar bacskattering returns received by the satellite, it is decided that:

- as currently the scattering matrices of basic shapes (disks, needles, cylinders, ellipsoids) used by remote sensing models do not represent real shapes and dimensions of actual components of scatterers in the natural medium, EPA (Equivalence Principle Algorithm) is used to construct scattering matrices of natural scatterers (modelled after real natural objects such as tree trunk, branches, paddy leaf), and
- backscattering returns from a layer of terrain (such as paddy field, oil palm, dense vegetation) will be simulated through 2nd order iterative Radiative Transfer Theory Solution with derived scattering matrices from EPA and physical parameters from ground truth measurement, and
- comparison of simulation results and satellite SAR images will be conducted to determine the validity of model as well as analysis of key scatterers and salient scattering mechanisms involved

Stage 2:

With the evaluation of model developed in Stage 1, development efforts in Stage 2 will focus on:

- extension to multiscale modeling of clusters or configuration of natural objects (like a layer of vegetation, paddy field etc) with new model developed based on full EPA solution and direct simulation of scattered fields through the EPA model developed, and
- utilization of fast multipole algorithm in solution performance improvement, and
- analysis of simulation results and comparison and validation with satellite SAR data

Appendix 3:

Theoretical Simulation and Analysis of Scattering Mechanisms from Vegetation

This appendix generally provides an overview of the theoretical model based on radiative transfer Theory and how this is applied to generate simulation of backscattering returns from natural medium. The constructed model allows a multilayer configuration and the simulation is obtained through second order iterative solution. In addition, analysis of scattering mechanisms from various vegetation media is also included.

Consider a multilayer medium which is used to model vegetation. Figure 1 shows the geometry of the N layer forest canopy over a rough surface. The boundaries of the nth layer are denoted by $z = -d_{n-1}$ (as top boundary) and $z = -d_n$ (as bottom boundary) where

$$d_n = \sum_{i=1}^{n} H_i \tag{1}$$

and $d_o = 0$, and H_i is the depth of the ith layer.

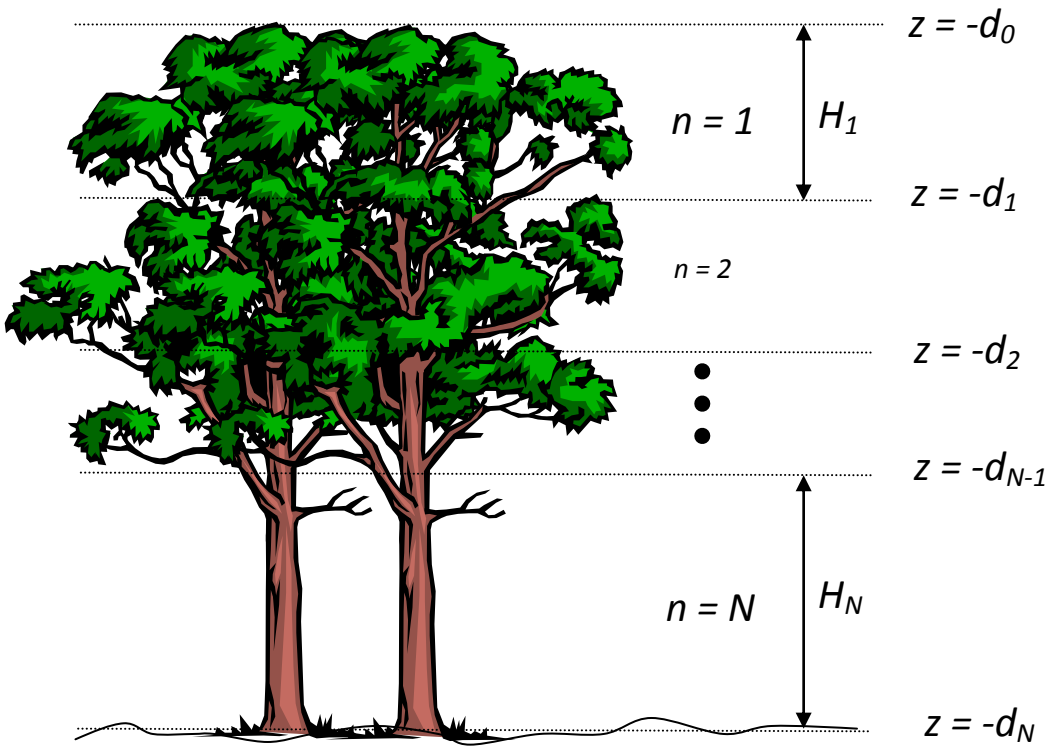

Figure 1: Geometry of multilayer forest canopy model

In order to find the backscattering returns from the multilayer medium described above, we can solve the radiative transfer equation shown in (2) below:

$$\cos\theta \frac{d\bar{I}}{dz} = -\bar{\bar{\kappa}}_e \bar{I} + \int \bar{\bar{P}} \bar{I}\, d\Omega \tag{2}$$

where $\bar{I}$ is the Stokes vector, $\bar{\bar{\kappa}}_e$ and $\bar{\bar{P}}$ are the extinction matrix and phase matrix of the medium, respectively. The phase matrix $\bar{\bar{P}}$ for scatterers can be from scatterers of basic shapes such as disk-shaped, needle-shaped, cylindrical and ellipsoidal scatterers.

The radiative transfer equation is solved iteratively by using the albedo as an iteration parameter. The phase matrices of these scatterers have included the DMPACT (Dense Medium Phase and Amplitude Correction Theory) with array phase correction factor and Fresnel amplitude and phase correction for coherence and near field consideration. These are incorporated into the radiative transfer formulation and up to second order solutions are obtained.

After solving for the intensity of the backscattered waves in the radiative transfer equation, the backscattering coefficient can be obtained using this equation:-

$$\sigma_{pq} = \frac{4\pi \cos\theta_s I_{sp}}{I_{iq}} \qquad (3)$$

where *p* and *q* represent the incident and backscattered polarizations respectively and can be *v* or *h*. θ_s is the angle of the scattered field with respect to the normal of the medium. I_{sp} is the intensity of the backscattered waves, while I_{iq} is the intensity of the incident wave.

The phase matrix of the scatterers in (2) is given by

$$\overline{\overline{P}} = \left\langle |\Psi|^2 \right\rangle_n \cdot \overline{\overline{S}} = \left\langle |\Psi|^2 \right\rangle_n \cdot \begin{bmatrix} S_{vv} & S_{vh} \\ S_{hv} & S_{hh} \end{bmatrix} = \begin{bmatrix} P_{vv} & P_{vh} \\ P_{hv} & P_{hh} \end{bmatrix} \tag{4}$$

where $\left\langle |\Psi|^2 \right\rangle_n$ is the array phase correction factor. $\overline{\overline{S}}$ is the phase matrix of a unit volume of scatterers of a single class and it is obtained by averaging the Stokes matrix over the size and spatial orientation of the scatterers.

$$\overline{\overline{P}}(\theta,\phi;\theta',\phi') = \int da \int db \int dc \int d\alpha \int d\beta \int d\gamma \cdot p(a,b,c,\alpha,\beta,\gamma) \cdot \overline{\overline{S}}(\theta,\phi;\theta',\phi') \tag{5}$$

where $\overline{\overline{S}}(\theta,\phi;\theta',\phi')$ is the Stokes matrix that relates the scattered intensity of a scatterer to the incident intensity. For ellipsoidal scatterer, *a*, *b* and *c* are the length of the semi-major axes, and α, β and γ are the Eulerian angles which describe the orientation of the ellipsoid. $p(a,b,c,\alpha,\beta,\gamma)$ is the joint probability density function for the quantities *a*, *b*, *c*, α, β and γ. The Stoke matrix has been improved to include Fresnel amplitude and phase correction to consider the near field effect of the scatterers. For detailed formulation of Fresnel correction, please refer to [1-2].

The array phase correction factor in (4) is given by

$$\left\langle |\Psi|^2 \right\rangle_n = \frac{1-e^{-k_{si}^2\sigma^2}}{d^3} + \frac{e^{-k_{si}^2\sigma^2}}{d^3} \sum_{q=1}^{\infty} \frac{(k_{si}^2\sigma^2)^q}{q!} \cdot \left[\left(\sqrt{\frac{\pi}{q}} \left(\frac{l}{d} \right) \right)^3 \exp\left(\frac{-k_{si}^2 l^2}{4q} \right) - a(k_x)a(k_y)a(k_z) \right] \tag{6}$$

where

$$a(k_r) = \sqrt{\frac{\pi}{q}} \left(\frac{l}{d} \right) \exp\left(\frac{-k_r^2 l^2}{4q} \right) \mathrm{Re}\left\{ erf\left(\frac{(qd/l) + jk_r l}{2\sqrt{q}} \right) \right\} \text{ and}$$

$\bar{k}_i$ and $\bar{k}_s$ are the propagation vectors in the incident and scattering directions, *l* is the array correlation length, *d* denotes the average distance between scatterers and σ is the standard deviation of scatterers from their mean positions.

When we assume independent scattering from the scatterers, $\left\langle |\Psi|^2 \right\rangle_n$ reduces to n_o, which is the number of scatterers per unit volume.

For a medium with *N* classes of scatterers, the total phase matrix is given by

$$\overline{\overline{P}}_{total}(\theta,\phi;\theta',\phi') = \sum_{i=1}^{N} \overline{\overline{P}}_i(\theta,\phi;\theta',\phi') \,. \tag{7}$$

The contribution of the solution of the radiative transfer equation can be expressed by

$$I_{spq}^{total} = I_{spq}^{0} + I_{spq}^{1} + I_{spq}^{2} \tag{8}$$

where I_{spq}^{w} is the backscatter intensity with *pq* polarization (*p*,*q* = *v*,*h*) and w denotes the order of the iterative solution of the radiative transfer equation. The components of all these can be further divided to:

$$\begin{aligned} I_{spq}^{0} &= I_{spq}^{s} \\ I_{spq}^{1} &= \sum_{n=1}^{N} I_{spq}^{v}(n) + I_{spq}^{vs}(n \leftrightarrow s) \\ I_{spq}^{2} &= \sum_{n=1}^{N} I_{spq}^{v-v}(n) + \sum_{n=2}^{N}\sum_{m=1}^{n-1} I_{spq}^{v-v}(n \leftrightarrow m) \end{aligned} \tag{9}$$

where I_{spq}^{s} is the contribution from the ground surface scattering and $I_{pq}^{v}(n)$ accounts for direct volume scattering from the scatterers in *n*th layer. $I_{pq}^{vs}(n \leftrightarrow s)$ includes the interaction between the scatterers in the *n*th layer and the ground surface (surface-volume scattering). $I_{pq}^{v-v}(n)$ and $I_{pq}^{v-v}(n \leftrightarrow m)$ are the contributions from the volume-volume scattering between the scatterers within the *n*th layer and between the scatterers in layers *n* and *m*, respectively.

Regrouping the contribution terms in equation (9) into the surface, surface-volume and volume scattering groups, the solution is then given by

$$I_{spq}^{total} = I_{spq}^{s} + I_{spq}^{vs} + I_{spq}^{v} \tag{10}$$

$$I_{spq}^{vs} = I_{spq}^{vs}(n \leftrightarrow s)$$
$$I_{spq}^{v} = \sum_{n=1}^{N} I_{spq}^{v}(n) + \sum_{n=1}^{N} I_{spq}^{v-v}(n) + \sum_{n=2}^{N}\sum_{m=1}^{n-1} I_{spq}^{v-v}(n \leftrightarrow m) \tag{11}$$

For detailed formulation of the steps mentioned above and details of application of this model in natural medium such as paddy field and sea ice, please refer to [3-6].

Table 1 lists the parameters used in the physical configuration of various types of forest [Fig 1-2] which can be used by the model to study backscattering returns and analyze dominant scattering mechanisms.

	Temperate Coniferous Forest	Tropical Deciduous Forest	Tropical Evergreen Forest
Crown layer (m)	5.50	3.00	6.00
Trunk layer (m)	4.00	1.50	2.00
Leaf:			
Diameter (cm)	0.20	3.50	4.00
Length or thickness (cm)	10.00	0.05	0.05
Density (#/m^3)	1500	900	2600
Branch:			
Diameter (cm)	1.00	2.50	3.00
Length (m)	1.50	1.50	2.00
Density (#/m^3)	2.00	0.80	4.00
Upper Trunk:			
Diameter (cm)	8.0	5.0	5.5
Length (m)	5.50	3.00	6.00
Density (#/m^3)	0.0182	0.0666	0.1000
Lower Trunk:			
Diameter (cm)	16.0	10.0	11.0
Length (m)	4.00	1.50	2.00
Density (#/m^2)	0.0250	0.1333	0.3000

Table 1: Geometrical parameters for three types of forests.

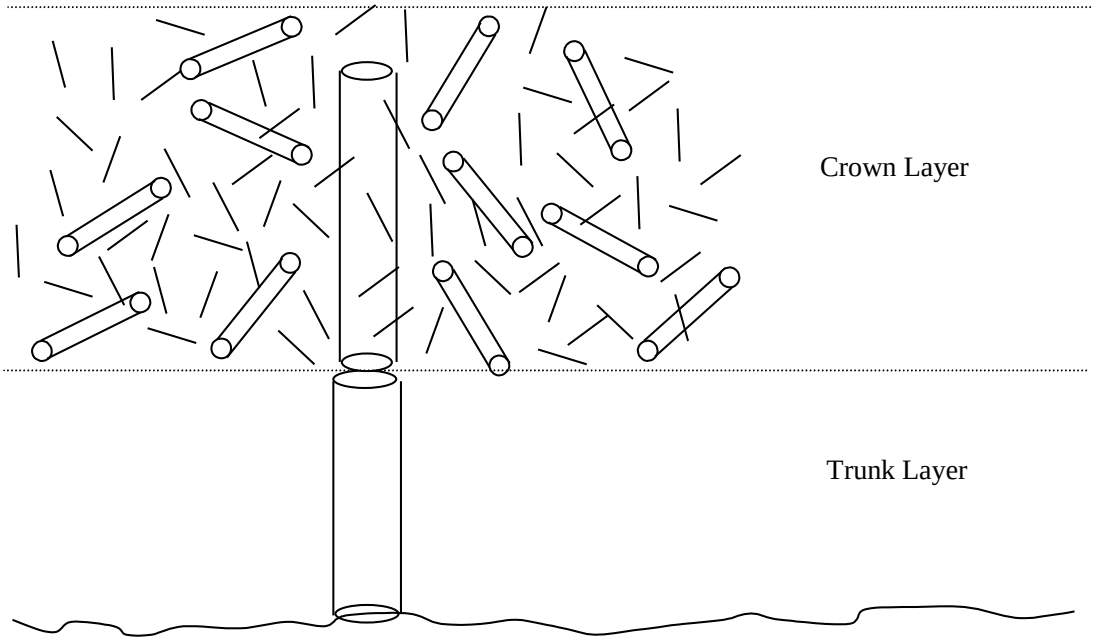

Figure 1: Modelling of temperate coniferous forest as a two layer random medium with needles as leaves.

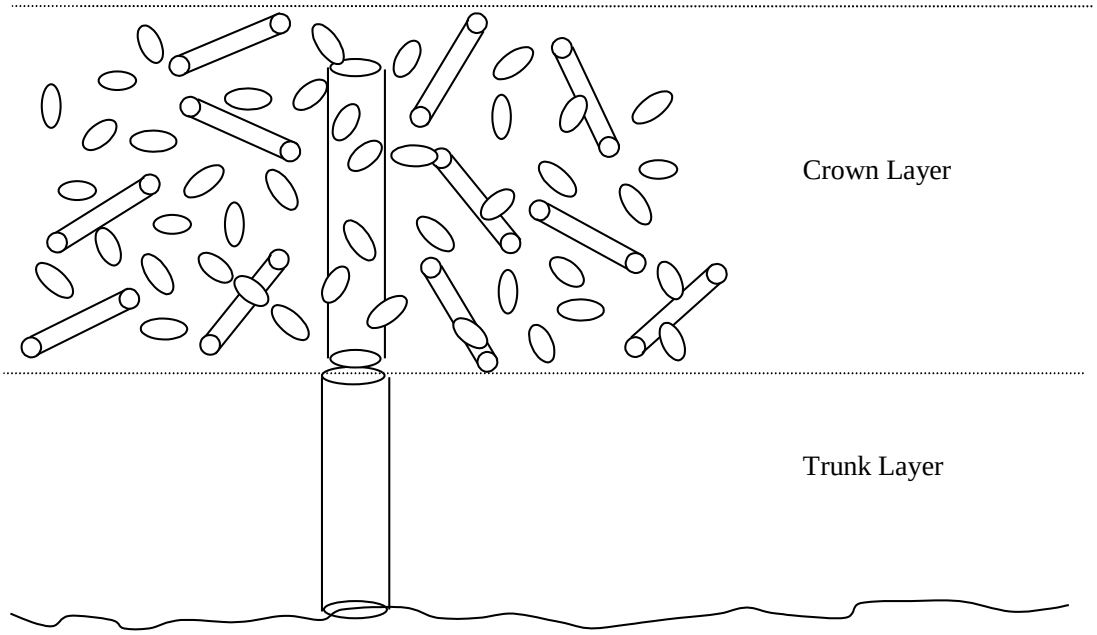

Figure 2: Modelling of tropical deciduous and evergreen forests as a two layer random medium with circular disks as leaves.

From the solutions, the following scattering contributions can be identified:

(i) Ground surface backscattering

(ii) Surface-volume scattering: leaf-ground, branch-ground, upper trunk-ground and lower trunk-ground

(iii) Direct volume scattering: leaves, branches, upper trunks and lower trunks

(iv) Volume-volume scattering (within the layer and between the layers)

Analysis of backscattering coefficient from different types of forests and vegetation is provided below based on theoretical simulations from the model by the research team over the years. This provides a good reference model for further development of EPA based microwave remote sensing model.

(a) Temperate Coniferous Forest

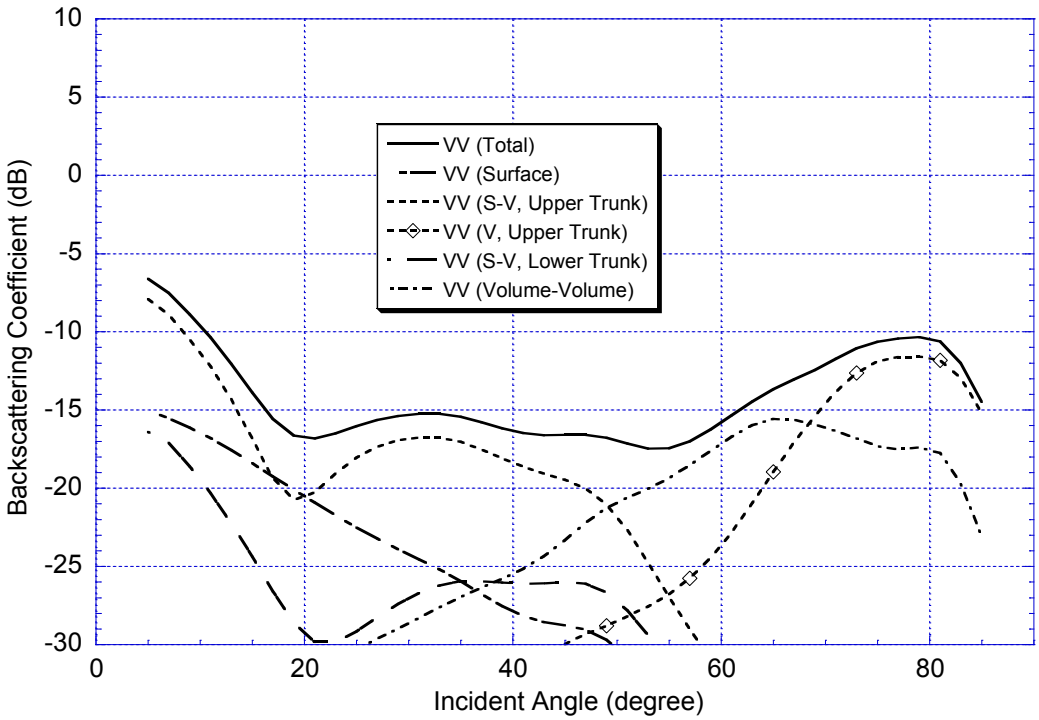

Figure 3: VV backscattering coefficient of temperate coniferous forest at P band plotted against incident angle for various dominant scattering mechanisms.

Figure 3 to Figure 5 show the backscattering coefficient at P band (0.5 GHz) for the coniferous forest plotted against the incident angle for VV, HH and VH polarizations, respectively. In Figure 3 where the VV polarization case is shown, it can be seen that at low incident angle ($\theta_i \lesssim 50^o$), the dominant scattering contribution comes from the surface-volume interactions between the ground surface and the upper trunk. In addition, the lower trunk-ground interaction is also considerably more important than other volume scattering contributions. In this case, both the upper and the lower trunks act as corner reflectors to give strong scattering in the backscattering direction. Direct backscattering from the ground surface is also found important but decreases as the incident angle increases. For higher incident angles ($\theta_i \gtrsim 50^o$), the surface-volume scattering contributions for VV polarization become smaller in the region of angles where the Brewster angle effect is important. At these high angles, it is found that the volume scattering from the upper trunk and volume-volume scattering become dominant.

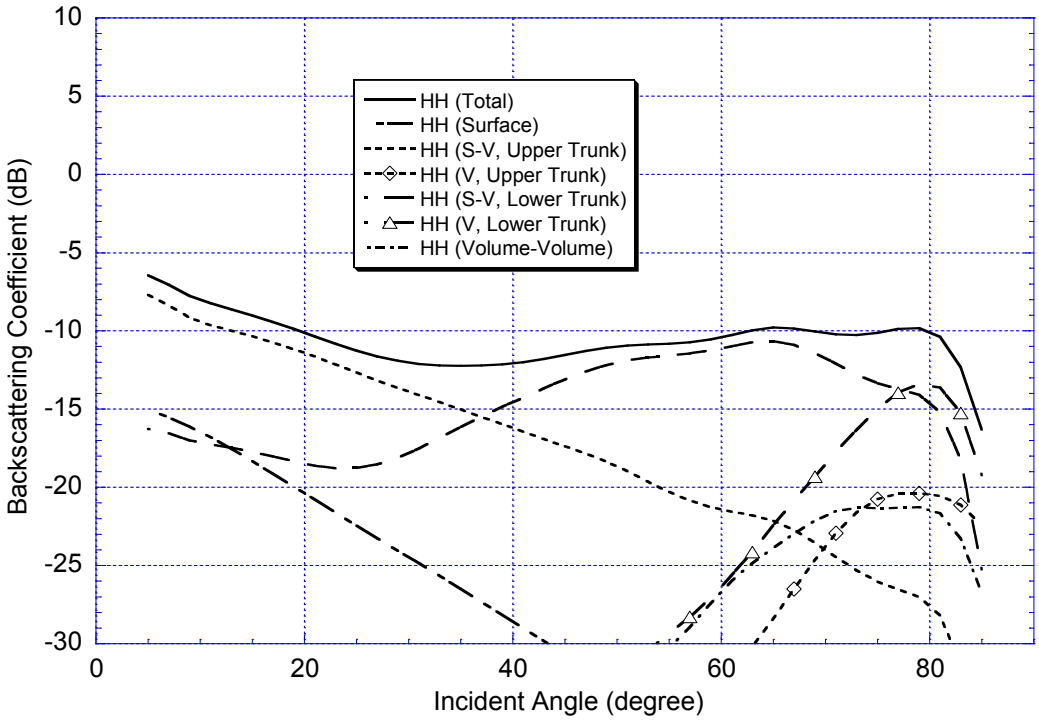

Figure 4: HH backscattering coefficient of temperate coniferous forest at P band plotted against incident angle for various dominant scattering mechanisms.

For HH polarization (Figure 4) where there is no Brewster angle effect, the dominant scattering contributions are from the lower trunk-ground and upper trunk-ground interactions for most incident angles. Ground surface backscattering is also important at low incident angles. The volume scattering contributions from the upper trunks and the lower trunks and the volume-volume scattering become important only at very high incident angles. For VH polarization (Figure 5), it is shown that the upper trunk-ground interactions are dominant at incident angles up to 50^o. The lower trunk-ground interactions are generally smaller but still more important than other scattering contributions in this region of incident angles. When the incident angle increases ($\theta_i \gtrsim 50^o$), volume-volume scattering contribution starts to be important. At very high incident angles, the two major scattering contributions are the volume-volume scattering and the direct volume scattering from upper trunks.

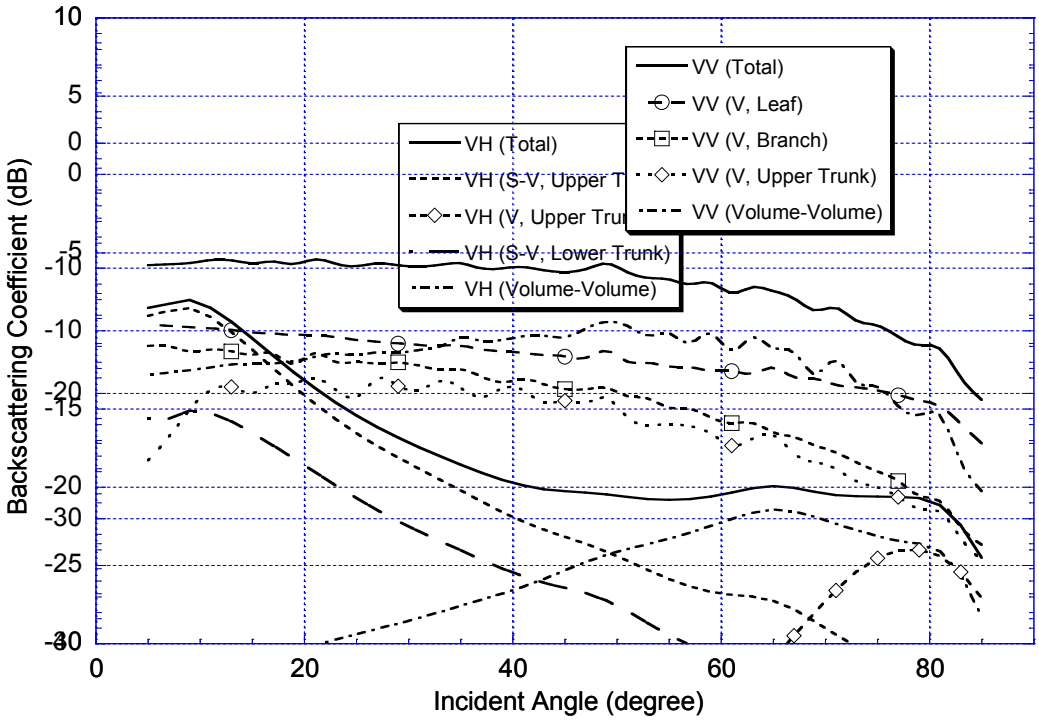

Figure 6: VH backscattering coefficient of temperate coniferous forest at X band plotted against incident angle for various dominant scattering mechanisms.

At 10 GHz (X band), different scattering mechanisms are dominant for backscattering from the coniferous forest considered. Figure 6 to Figure 8 show the contributions from different scattering mechanisms against incident angles for VV, HH and VH polarizations, respectively. At this frequency, due to the increase of attenuation in the crown layer, the ground surface backscattering contributions and the surface-volume scattering contributions are negligibly small. For VV polarization (Figure 6), the needle-shaped leaves are the strongest scatterers compared with the direct volume scattering from branches and trunks. For the range of incident angles considered, the direct scattering from the needle-shaped leaves is dominant at low incident angles whereas for most high incident angles, the volume-volume scattering is more important. For HH polarization, the same observation as in the VV case can be obtained. For VH polarization, it is found that the volume-volume scattering is the strongest source in contributing the backscattering returns for most incident angles. Although the direct volume scattering contribution from the leaves is smaller than

that of the volume-volume scattering, it is much higher than the direct volume scattering contribution from the branches.

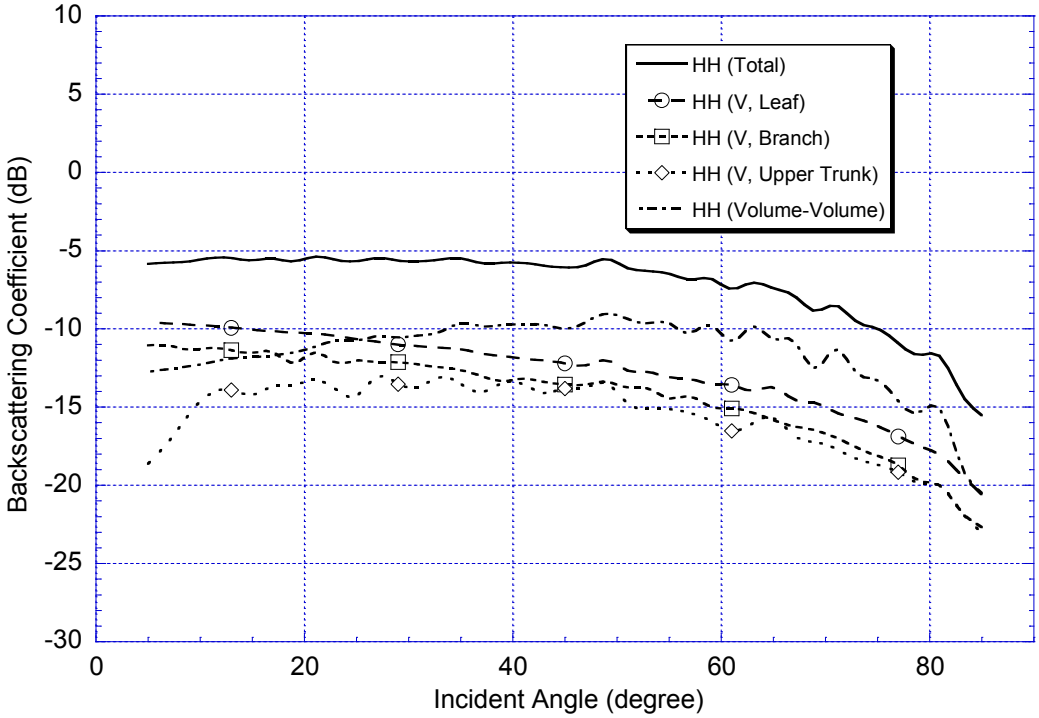

Figure 7: HH backscattering coefficient of temperate coniferous forest at X band plotted against incident angle for various dominant scattering mechanisms.

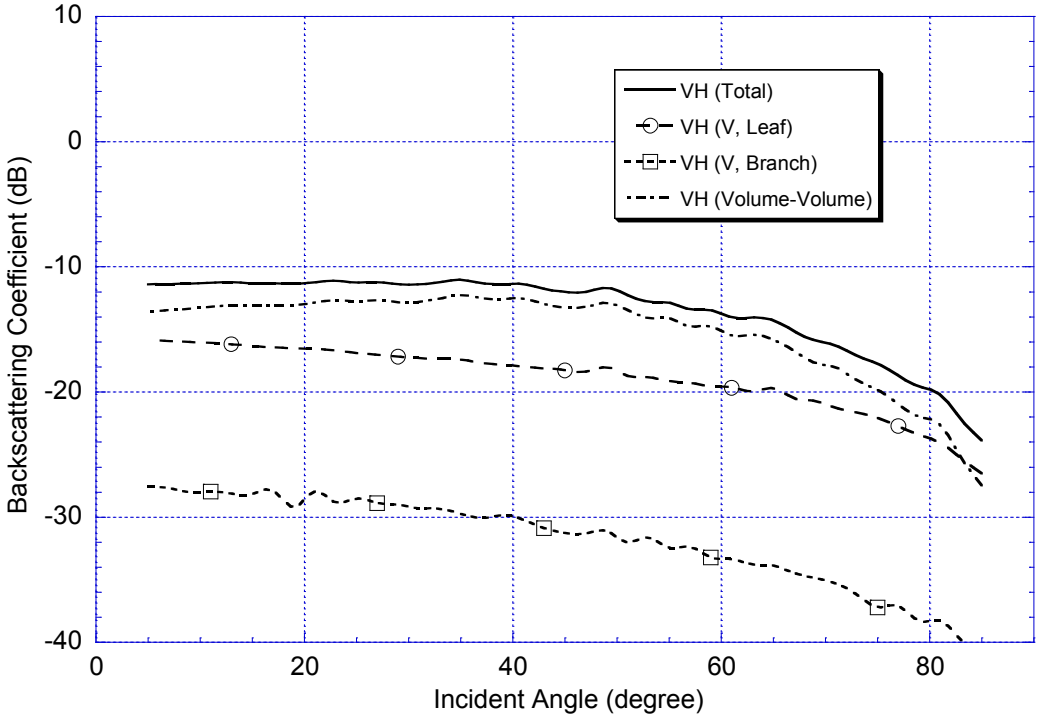

Figure 8: VH backscattering coefficient of temperate coniferous forest at X band plotted against incident angle for various dominant scattering mechanisms.

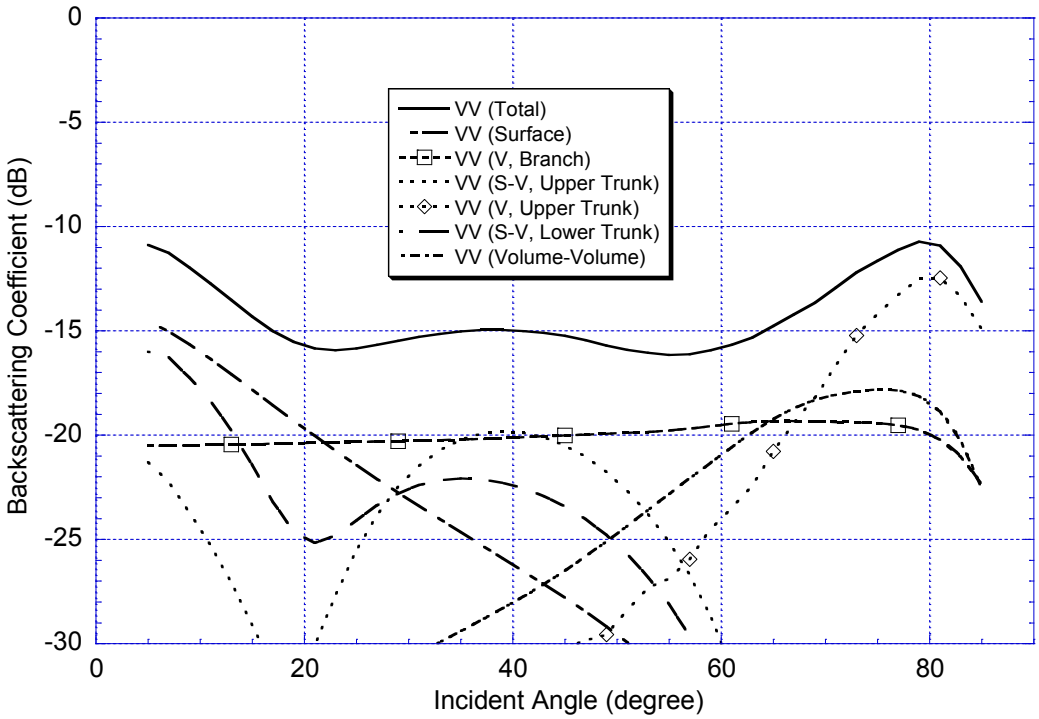

Figure 9: VV backscattering coefficient of tropical deciduous forest at P band plotted against incident angle for various dominant scattering mechanisms.

(b) Tropical Deciduous Forest

For the tropical deciduous forest considered here, it has thicker branches and smaller trunks compared with the temperate coniferous forest. From Figure 9 to Figure 11 they show the various scattering contributions for a range of incident angles for VV, HH and VH polarizations, respectively. For VV polarization (Figure 5.58), it is found that at low incident angles ($\theta_i \lesssim 20^o$), the three dominant scattering contributions are (in order of contribution) the ground surface backscattering, the lower trunk-ground scattering and the direct volume scattering from the randomly oriented branches. For incident angles between 20^o and 50^o, the dominant scattering contributions are from the direct volume scattering from the branches, the upper trunk-ground interactions and the lower trunk-ground interactions. Combining the two types of trunk-ground interactions, its contribution is still generally higher than the direct volume scattering from the branches. For higher incident angles ($\theta_i \gtrsim 50^o$),

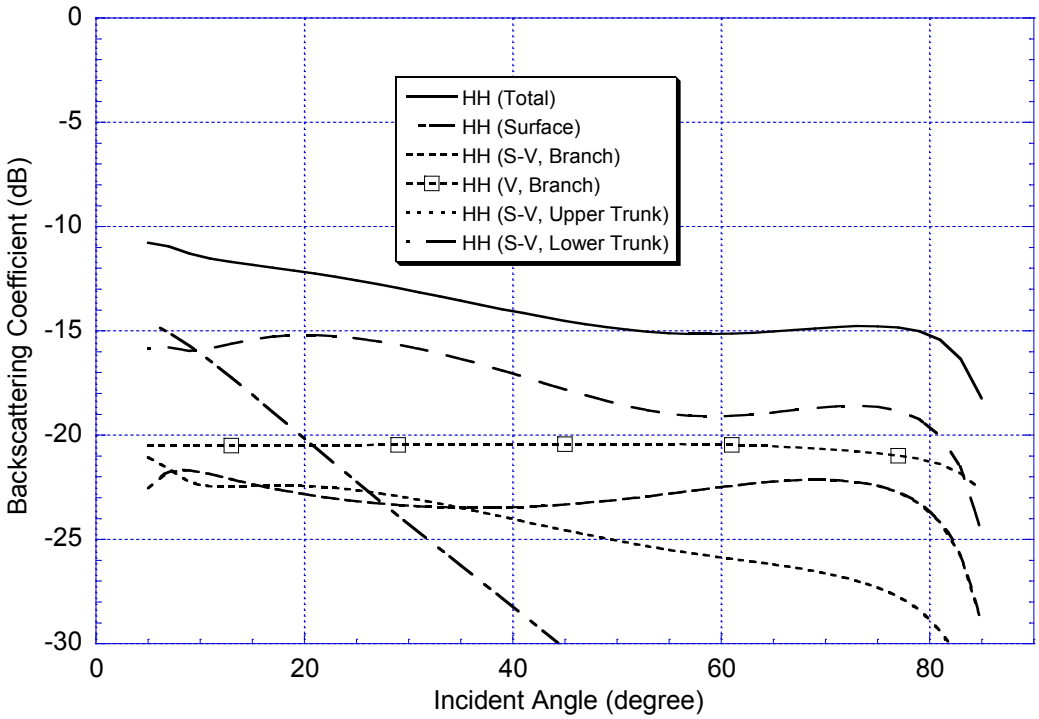

Figure 10: HH backscattering coefficient of tropical deciduous forest at P band plotted against incident angle for various dominant scattering mechanisms.

volume-volume scattering and direct volume scattering from the branches and upper trunks are the dominant scattering mechanisms. As in the temperate coniferous case, the Brewster angle effect reduces the volume-ground interactions at these high incident angles.

For HH polarization (Figure 10), the lower trunk-ground interactions are dominant over most incident angles, except at very low incident angles ($\theta_i \lesssim 10^o$) where ground surface backscattering is slightly more important. The direct volume scattering from the branches and the branch-ground and the upper trunk-ground interactions are also contributing substantially. For VH polarization (Figure 11), it is clearly shown that the lower trunk-ground scattering contribution is important at low incident angles ($\theta_i \lesssim 30^o$) whereas the direct volume scattering from the branches is dominant for higher incident angles.

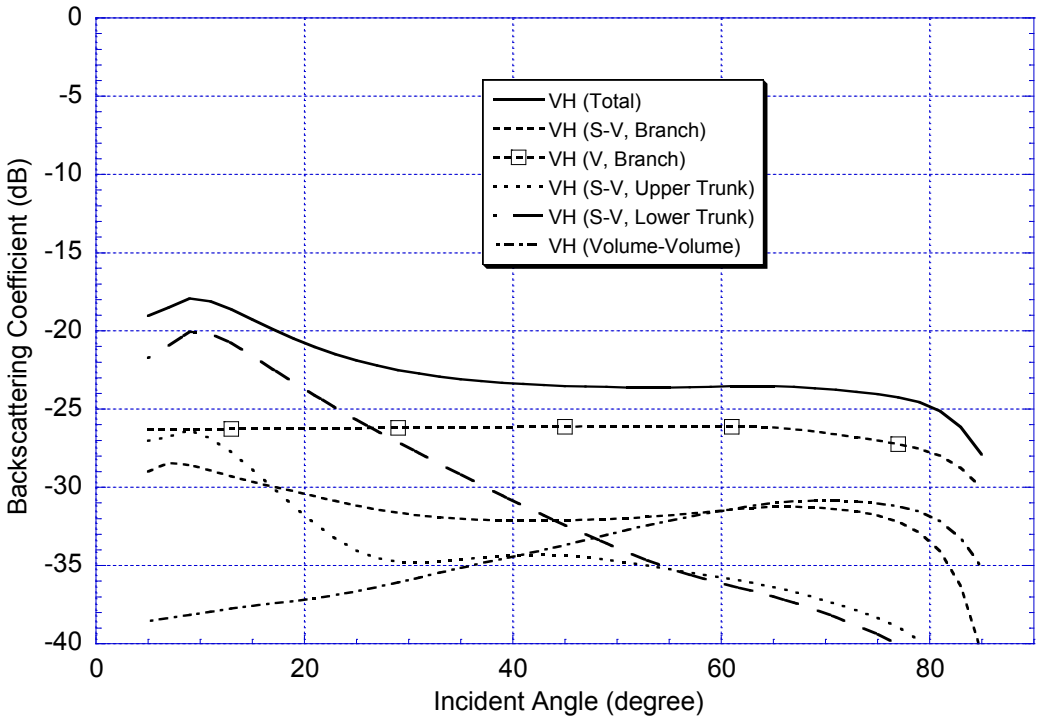

Figure 11: VH backscattering coefficient of tropical deciduous forest at P band plotted against incident angle for various dominant scattering mechanisms.

At 10 GHz (X band), the various scattering contributions for the tropical deciduous forest for VV, HH and VH polarizations are shown in Figure 12 to Figure 14, respectively. For both VV and HH polarizations (as shown in Figures 12 and 13), it is clearly shown that the backscattering returns are generally dominated by the direct volume scattering from the disk-shaped leaves and the volume-volume scattering, where the former is more important than the latter at low incident angles and vice versa at high incident angles. The other two scattering contributions that are lower but may be considered are the direct volume scattering from the branches and the upper trunks. The attenuation of the waves in the crown layer is high enough that practically the volume scattering from the lower layer and the surface-volume scattering contributions are negligibly small. For VH polarization (Figure 14), it is found that the backscattering returns are solely from the volume-volume scattering as the direct volume scattering from the disk-shaped leaves and branches and the leaf-ground interactions do not contribute enough to be comparable to that of the volume-volume scattering. The disk-shaped leaves with broad leaf surface in this case do not

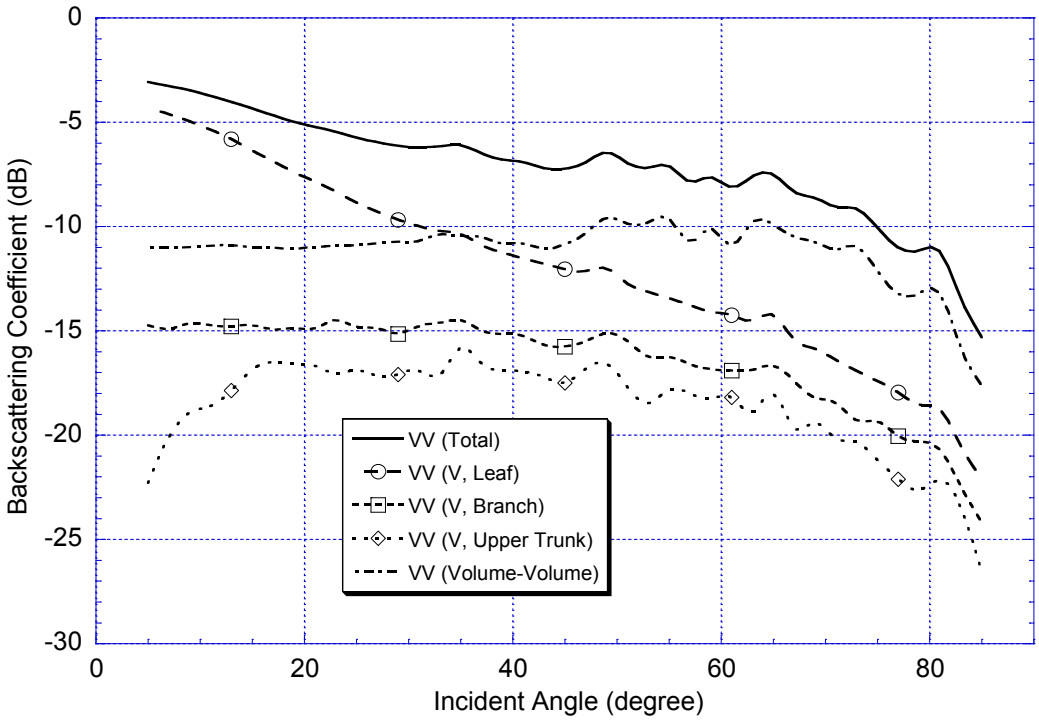

Figure 12: VV backscattering coefficient of tropical deciduous forest at X band plotted against incident angle for various dominant scattering mechanisms.

produce as much cross polarized returns as the needle-shaped leaves in the temperate coniferous case although both of them have almost the same volume fraction (~0.04%).

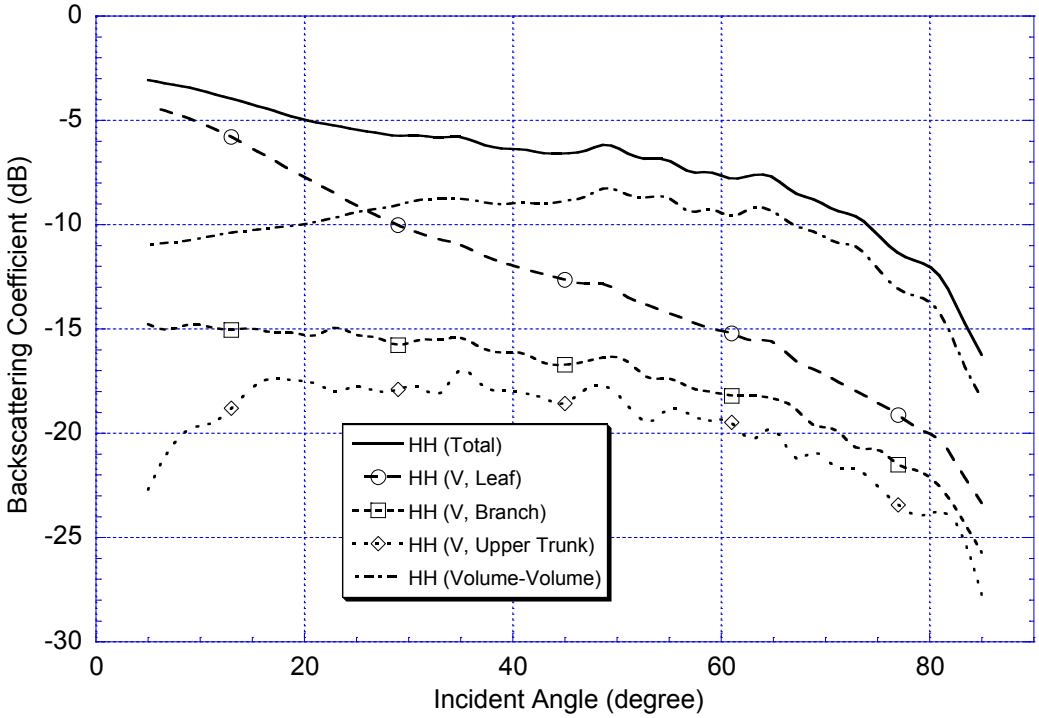

Figure 13: HH backscattering coefficient of tropical deciduous forest at X band plotted against incident angle for various dominant scattering mechanisms.

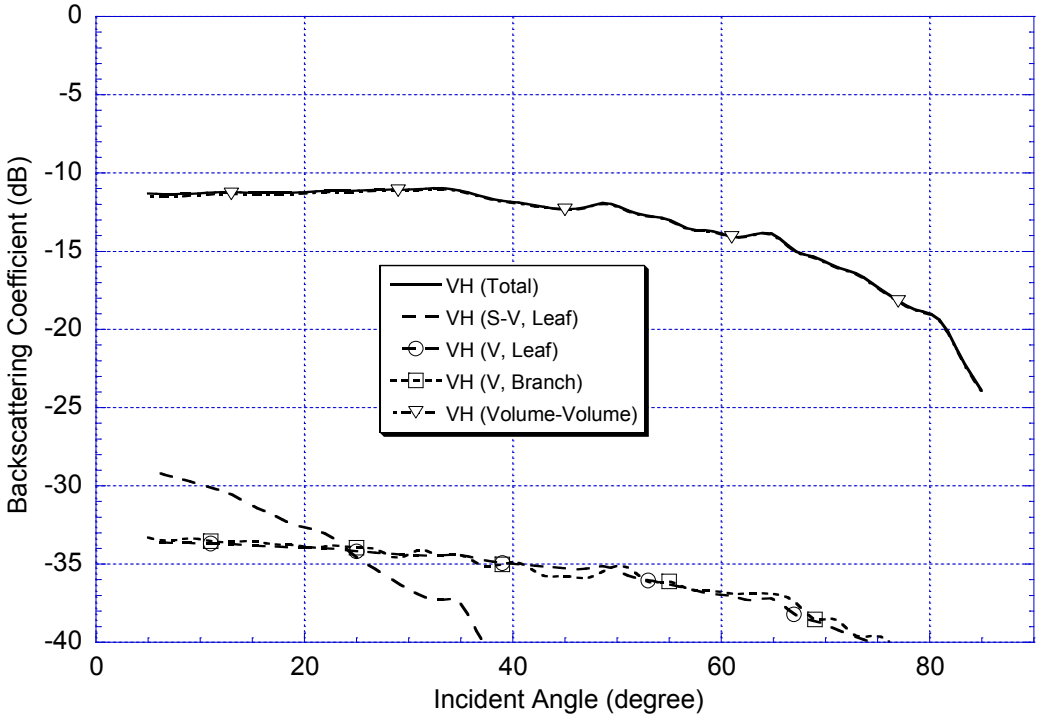

Figure 14: VH backscattering coefficient of tropical deciduous forest at X band plotted against incident angle for various dominant scattering mechanisms.

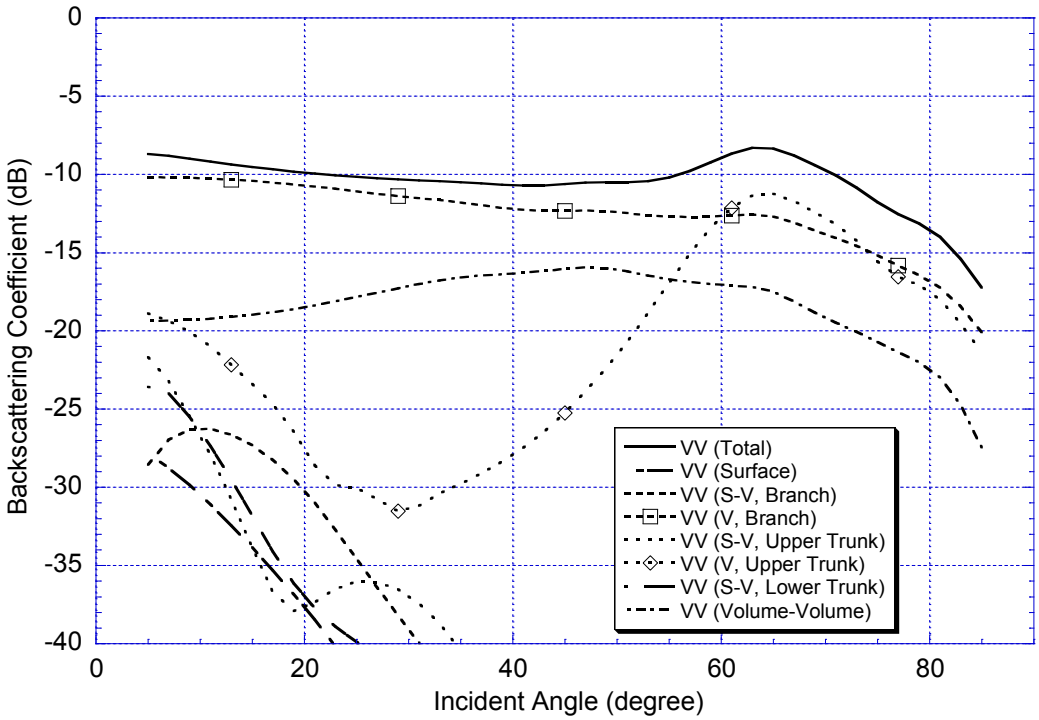

Figure 15: VV backscattering coefficient of tropical evergreen forest at P band plotted against incident angle for various dominant scattering mechanisms.

(c) Tropical Evergreen Forest

Figure 15 to Figure 17 show the backscattering coefficients at 0.5 GHz (P band) for the dominant scattering mechanisms involved in the tropical evergreen forest backscattering and are plotted against the incident angles for VV, HH and VH polarizations, respectively. For VV polarization (Figure 15), the backscattering returns are dominated by the direct volume scattering from the branches and upper trunks and the volume-volume scattering. In the tropical evergreen forest case, the volume fraction of the evergreen leaves is about four times (~0.16%) denser than those of the temperate coniferous and tropical deciduous forests. In addition, the volume fraction of the branches for the tropical evergreen forest is at least 10 times denser than those of the other two types and the density of its upper trunks is also the highest of the three. Thus, the attenuation through the crown layer is high and this leads to much reduced contributions from the ground surface backscattering and

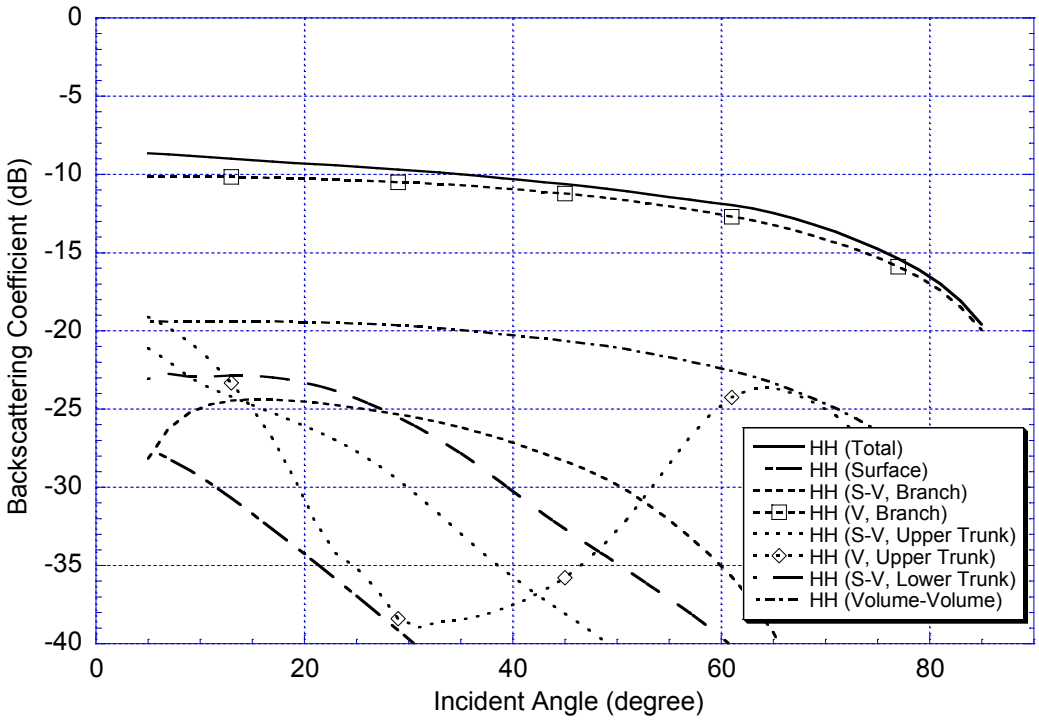

Figure 16: HH backscattering coefficient of tropical evergreen forest at P band plotted against incident angle for various dominant scattering mechanisms.

surface-volume scattering as compared to direct volume scattering and volume-volume scattering from the crown layer. For VV polarization as shown in Figure 15, direct volume scattering contribution from the branches is dominant for most incident angles, except at high incident angles ($\theta_i \gtrsim 60^o$) where the direct volume scattering contribution from the upper trunks becomes equally important. Due to its smaller size compared to the branches and upper trunks, the disk-shaped leaves contribute relatively less backscattering returns.

For HH polarization (Figure 16), the backscattering contribution from the branches is dominant for the range of incident angles considered here. It can be seen that those surface-volume contributions (branches and trunks) are generally more important than in the VV polarization case for wider incident angle range as there is no Brewster angle effect for HH polarization. In Figure 17 where the VH polarization case is shown, the direct volume scattering from the branches and

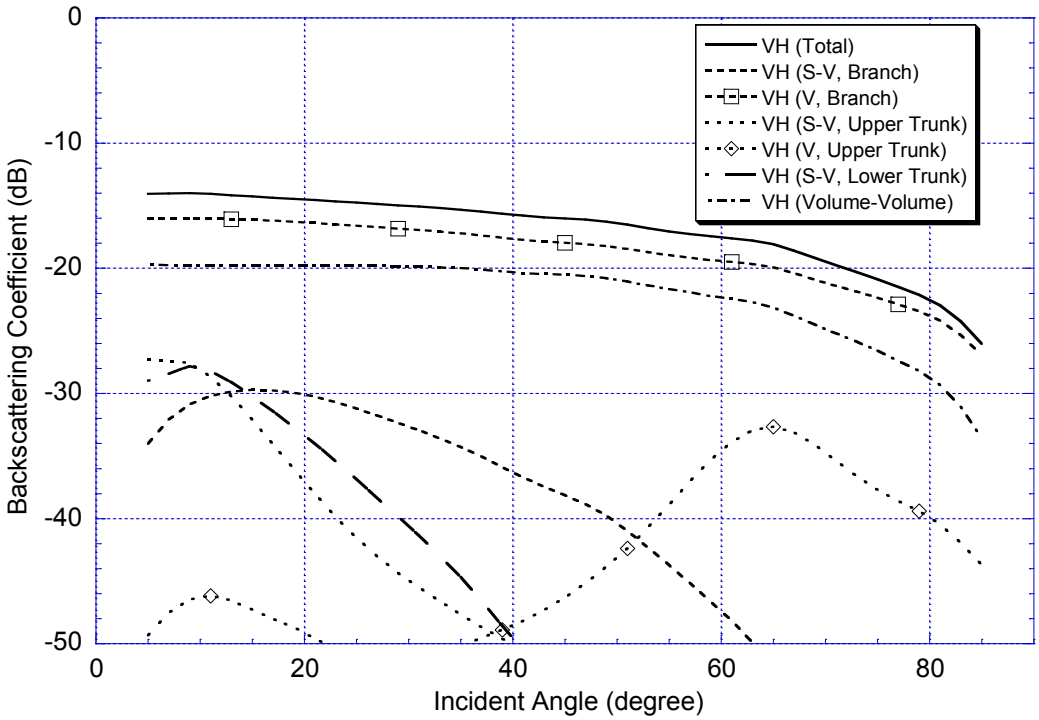

Figure 17: VH backscattering coefficient of tropical evergreen forest at P band plotted against incident angle for various dominant scattering mechanisms.

volume-volume scattering are important contributors to the backscattering returns throughout the range of incident angles considered.

At 10 GHz (X band), similar plots for the VV, HH and VH polarizations are shown in Figure 18 to Figure 20. For VV and HH polarizations, it is found that the leaves are the dominant scatterers for incident angles less than 20^{o}. For higher incident angles, the volume-volume scattering becomes more important than other scattering mechanisms. For VH polarization, as in the case of tropical deciduous forest, the backscattering returns are significantly due to the volume-volume scattering.

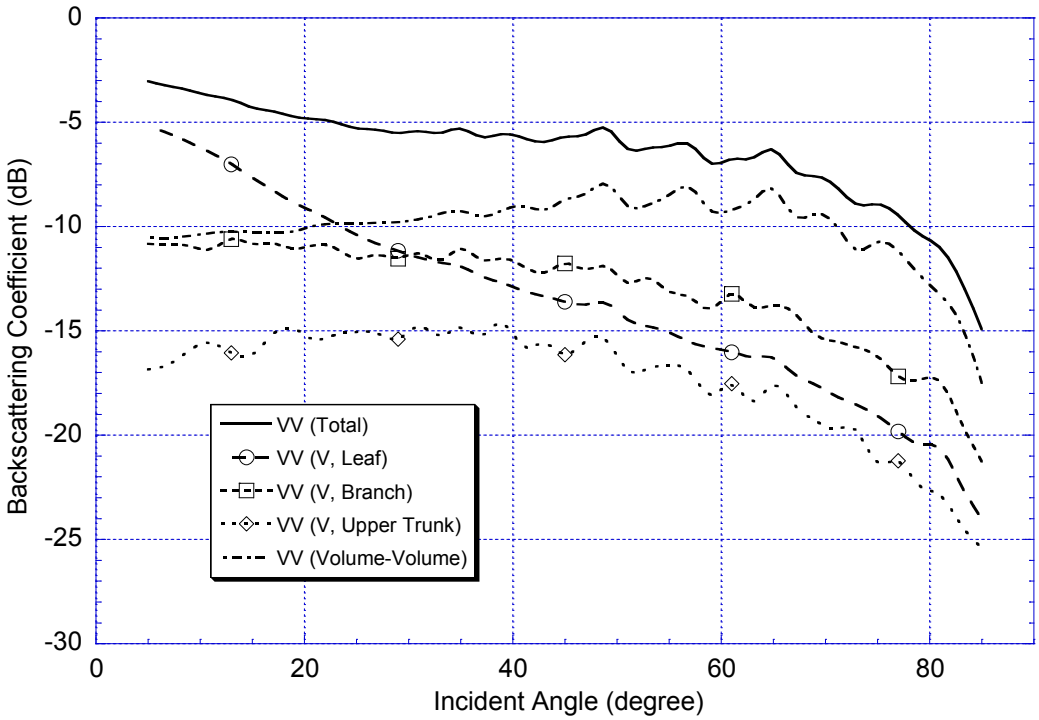

Figure 18: VV backscattering coefficient of tropical evergreen forest at X band plotted against incident angle for various dominant scattering mechanisms.

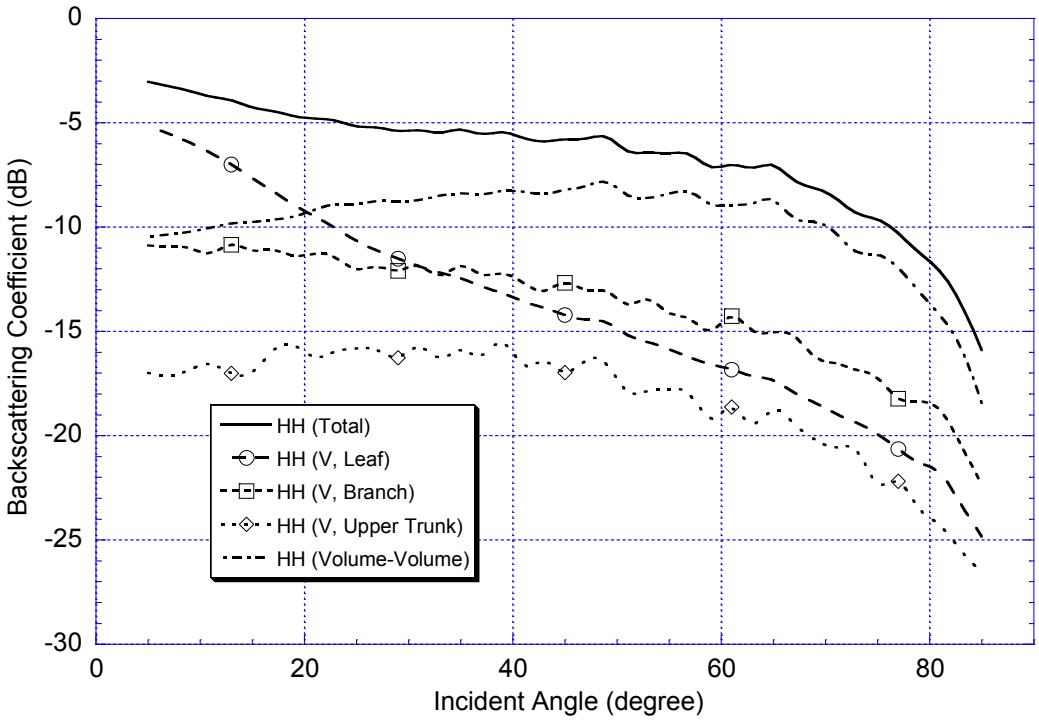

Figure 19: HH backscattering coefficient of tropical evergreen forest at X band plotted against incident angle for various dominant scattering mechanisms.

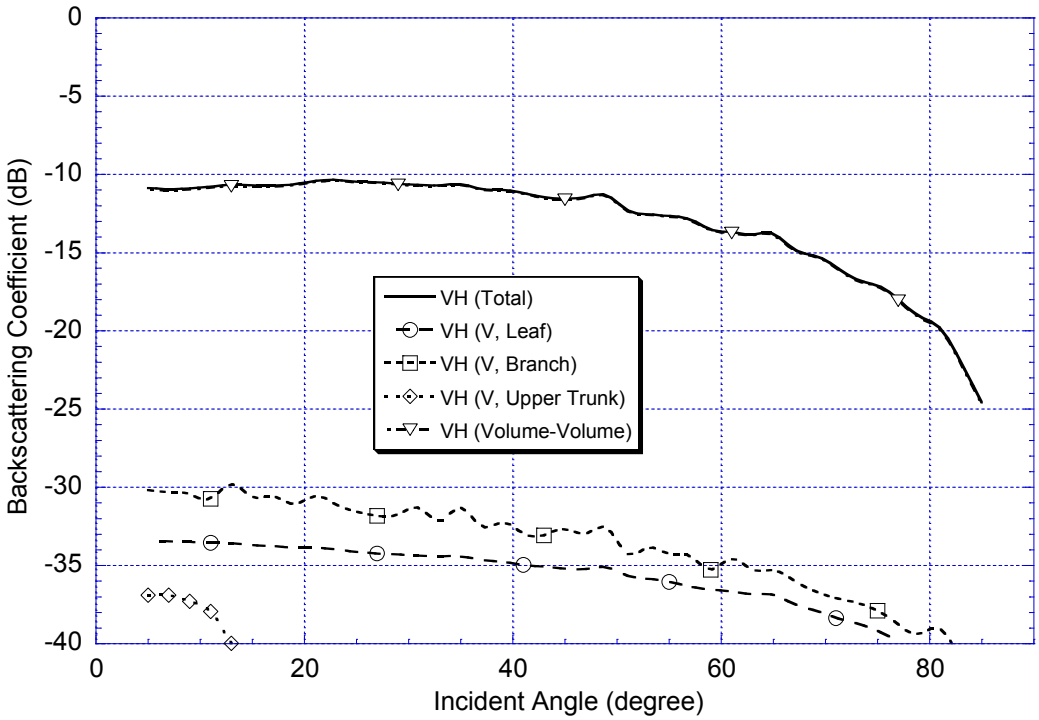

Figure 20: VH backscattering coefficient of tropical evergreen forest at X band plotted against incident angle for various dominant scattering mechanisms.

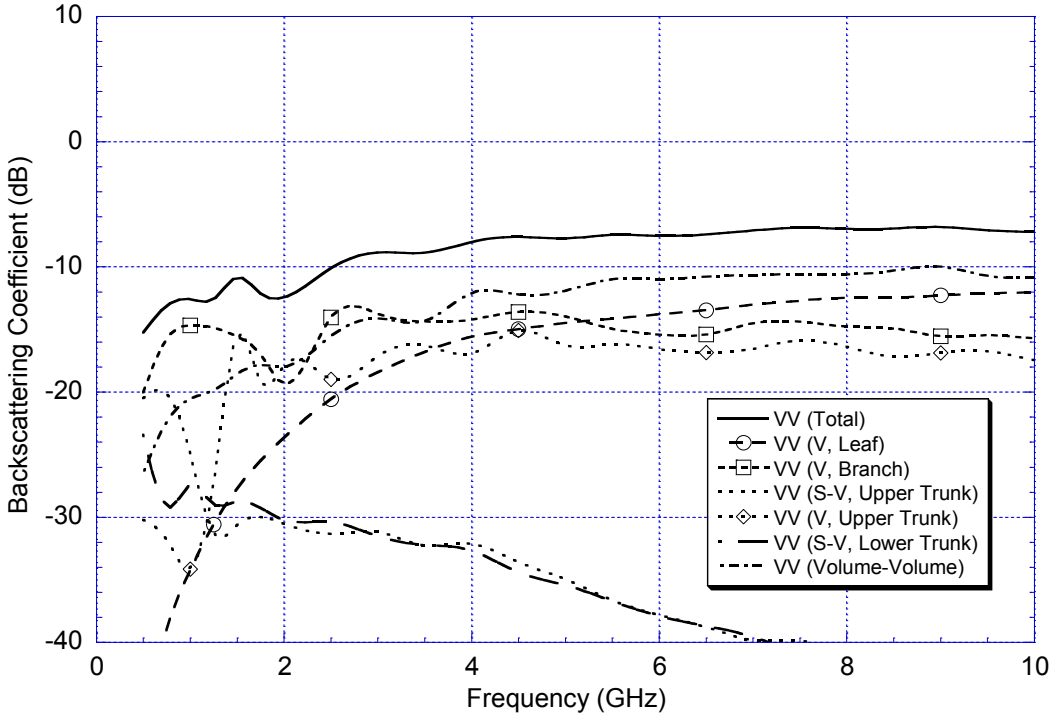

Figure 21: VV backscattering coefficient of tropical deciduous forest at 45^{o} incident angle plotted against frequency for various dominant scattering mechanisms.

From the analysis above for the cases of 0.5 GHz and 10.0 GHz, it is known that the dominance of certain scattering mechanisms changes with frequency. To show this effect in more detail, the deciduous forest case is chosen and the backscattering coefficients for various scattering mechanisms at 45^{o} incident angle are plotted for a frequency range of 0.5 GHz to 10 GHz. Figure 21 to Figure 23 show the graphs for VV, HH and VH polarizations, respectively. Only those dominant scattering mechanisms will be included in the graphs.

For VV polarization, it is found that at 0.5 GHz, three dominant scattering mechanisms are the direct volume scattering from the branches, the upper trunk-ground interactions and the lower trunk-ground interactions. When the frequency increases (~ 1 GHz – 3 GHz), the dominant scattering mechanisms are the direct volume scattering from the branches and upper trunks and the volume-volume scattering. For higher frequency ($\gtrsim$ 3 GHz), volume-volume scattering becomes the dominant scattering mechanism, but the other important contributors to the backscattering returns are the direct volume scattering from the leaves, branches and upper trunks. It should be noted that the direct scattering contribution from the leaves increases as the frequency increases and becomes the most important direct

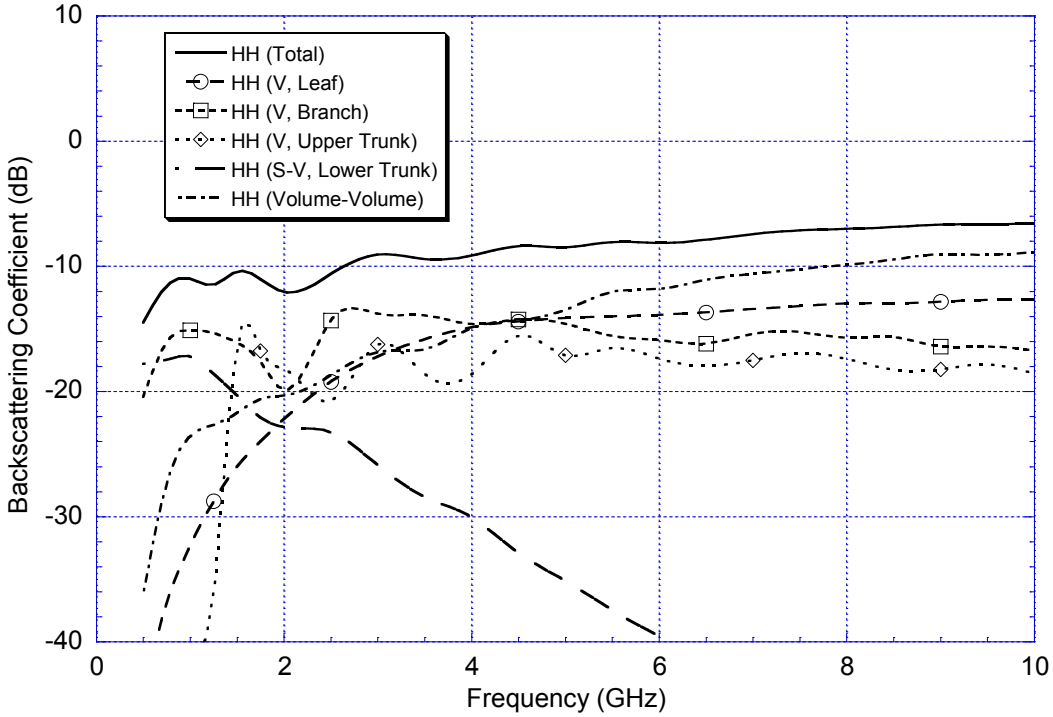

Figure 22: HH backscattering coefficient of tropical deciduous forest at 45^{o} incident angle plotted against frequency for various dominant scattering mechanisms.

scattering mechanism at 5 GHz and above when compared with the direct scattering from the other scatterers such as the branches and upper trunks.

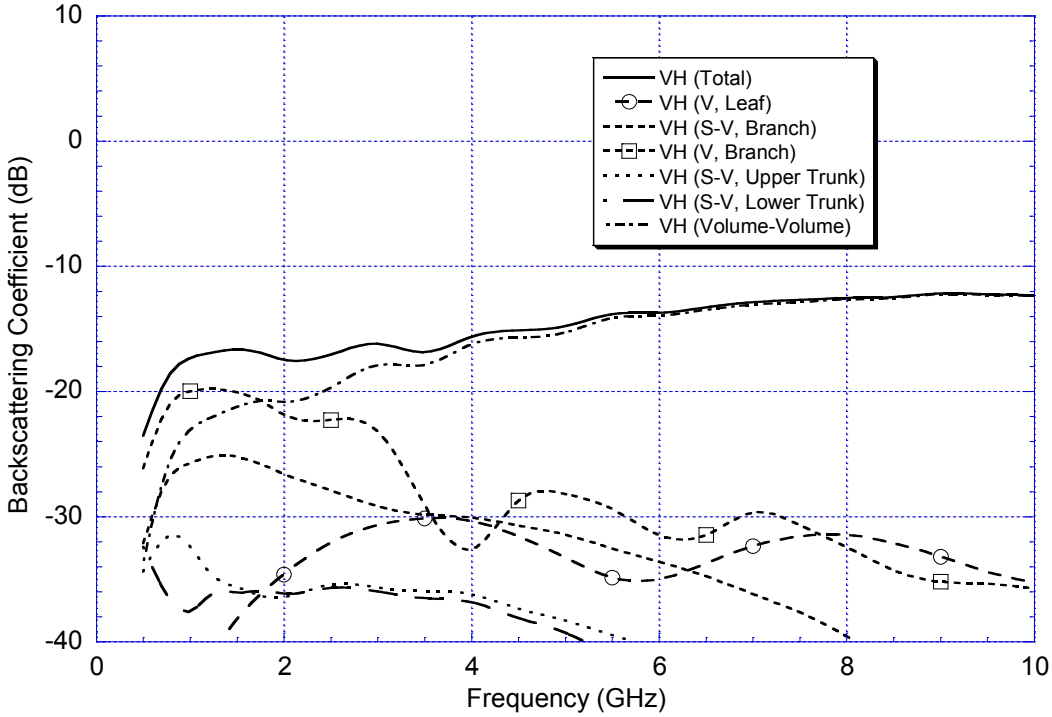

Figure 23: VH backscattering coefficient of tropical deciduous forest at 45^{o} incident angle plotted against frequency for various dominant scattering mechanisms.

For HH polarization, the dominant scattering mechanism at 0.5 GHz is the trunk-ground interaction from the lower trunks (which have diameter twice that of the upper trunks). As frequency increases, the direct volume scattering from the branches becomes important and the contribution from the lower-trunk interaction decreases. For frequency higher than 5 GHz, the same trend found in the VV polarization case is observed where the volume-volume scattering becomes the dominant scattering mechanism and the direct volume scattering from the leaves, branches and upper trunks are important. Out of the three direct volume scattering contributions, the contribution from direct scattering from the leaves is the highest. For VH polarization, the trend is simpler where the direct volume scattering from the branches is important at low frequency ($\lesssim$ 2 GHz) and decreases as frequency increases and the volume-volume scattering dominates at high frequency ($\gtrsim$ 2 GHz).

(d) Paddy Field and Oil Palm

In Figure 24, it shows a plot of various scattering mechanisms involved in the C-band HH backscattering coefficient of a 26-day old paddy field in Sungai Burung, Selangor State,

Malaysia where the ground truth measurement was conducted to collect physical parameters to be input to the simulation program based on this model.

In Figure 25, various scattering mechanisms involved in HH backscattering coefficient for two-year old oil palm is shown. Input physical parameters were obtained from ground truth measurement conducted in Perak State, Malaysia in August, 2013.

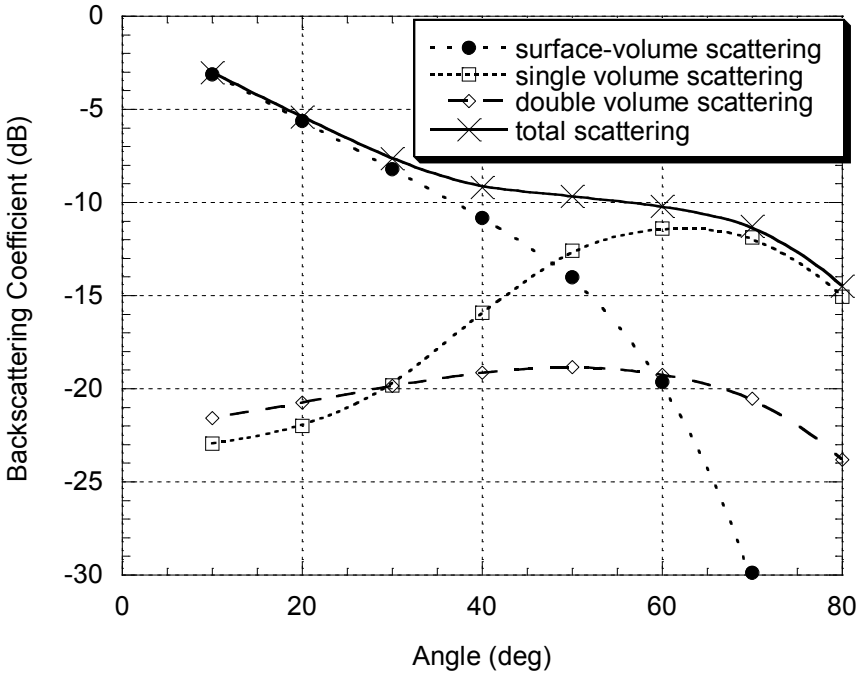

Figure 24: Various scattering mechanisms (HH polarization) in paddy field.

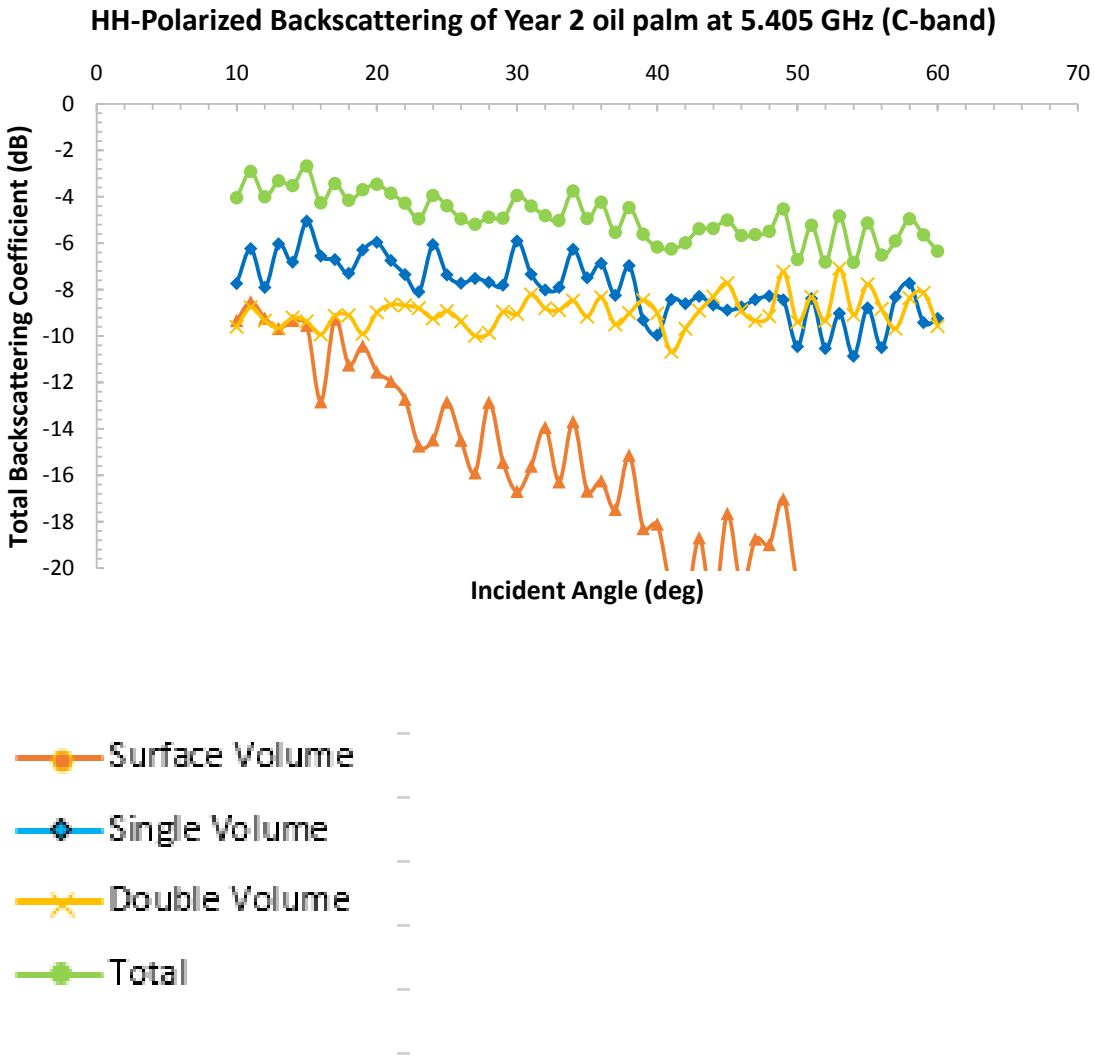

Figure 25: Various scattering mechanisms (HH polarization) for 2-year old oil palm.

In general, the above analysis provides us with better understanding of scattering mechanisms in various types of forests and vegetation. For future analysis, if the physical configuration of a particular type of forest or vegetation is given, this model can be utilized for such analysis to identify salient scattering mechanisms in microwave remote sensing of earth terrain.

References:

[1] H.T.Ewe and H.T.Chuah, "A Study of Fresnel Scattered Field for Non-Spherical Discrete Scatterers, Journal of Electromagnetic Waves and Applications", Vol. 14, 2000, pp. 51-52. Full text appears in Progress in Electromagnetics Research, PIER 25, 2000, pp. 189-222.

[2] J.Y. Koay, H.T. Ewe and H.T. Chuah, "A Study of Fresnel Scattered Fields for Ellipsoidal and Elliptic Disk-Shaped Scatterers," IEEE Transactions on Geoscience and Remote Sensing, Vol. 46, No. 3, 2008, pp. 1091 – 1103.
[3] H.T.Ewe and H.T.Chuah, "Electromagnetic Scattering from an Electrically Dense Vegetation Medium", IEEE Transactions on Geoscience and Remote Sensing, Vol. 38, No. 5, 2000, pp. 2093-2105.
[4] Chuah, H. T., Tjuatja, S., Fung, A. K. & Bredow, J. W. A phase matrix for a dense discrete random medium: Evaluation of volume scattering coefficient. IEEE Transactions on Geoscience and Remote Sensing, 34(5), 1996, pp. 1137-1143.
[5] J. Y. Koay, C. P. Tan, K. S. Lim, Saiful Bahari, H. T. Ewe, H. T. Chuah, J. A. Kong, "Paddy Fields as Electrically Dense Media: Theoretical Modeling and Measurement Comparisons with Season-Long Data," IEEE Transactions on Geoscience and Remote Sensing, Vol. 45, No. 9, 2007, pp. 2837-2849.
[6] M. D. Albert, Y. J. Lee, H.T. Ewe, and H.T. Chuah, "Multilayer Model Formulation and Analysis of Radar Backscattering from Sea Ice," Progress in Electromagnetics Research (PIER), Vol. 128, 2012, pp. 267-290.

Appendix 4:

Pilot Ground Truth Measurement

In order to understand better the physical configuration of natural medium such as vegetation, it is necessary for ground truth measurement to be conducted. The project team has previously conducted detailed ground truth measurement in paddy (or rice, largely planted in Asia region) field in Malaysia as well as sea ice and ice shelf areas in Ross Island Antarctica, these collected data will be useful in the modeling work. In 2013, with the support of funding of related project, detailed ground truth measurement of oil palm plantation was carried out. As of 2006, 11,000,000 hectares (42,000 sq mi) of oil palm plantation are found in tropical countries like Indonesia and Malaysia.

On 29 – 30 August 2013, ground truth measurement of oil palm trees was done at Changkat Chermin Estate and Lekir Estate in Perak State, Malaysia. For pilot study, plantation plots for 2, 7 and 14 year old palm were chosen.

Parameters such as leaf length, leaf width, leaf thickness, frond radius, frond length, trunk circumference and trunk height were measured. LaserAce TM 1000 rangefinder was used to measure canopy height and trunk height of taller palm. In addition, number of leaves per frond, number of fronds per palm and general distribution of leaf inclination angle were also counted and observed.

Samples of leaf, frond and soil of each plantation plot were also collected for measurement of moisture content and dielectric constant of each sample will then be calculated based on empirical model published in the literature.

These ground truth measurement parameters will be used as input parameters of model simulation.

Table 1 shows some of the physical parameters collected through the pilot ground truth measurement.

Age of oil palm	Y2	Y7	Y14
Leaf length (cm)	72.5	83.5	98.5
Leaf width (cm)	2.5	4	4.5
No of leaves per frond	232	295	268
Frond radius (cm)	1.15	1.53	1.67
Frond length (cm)	316	626	645
No of fronds per palm	40	40	48
Canopy height (cm)	399	663	717
Planting Density (palms/ha)	145	136	130
Surface soils type	Marine Clay	Silt Clay	Sandy Clay Loam

Table 1: Physical parameters measured in oil palm plantation.

It was also noticed that the growth of 14-year oil palm plot selected was not well as it was located at a site with soil type of sandy clay loam and number of leave per frond is less compared with that of 7-year oil palm plot. Figures 1-2 are collection of photos taken during the ground truth measurement. A more thorough field trip measurement was later conducted in October, 2013.

Figure 1: Oil palm plots (2-year, 7-year and 14 year).

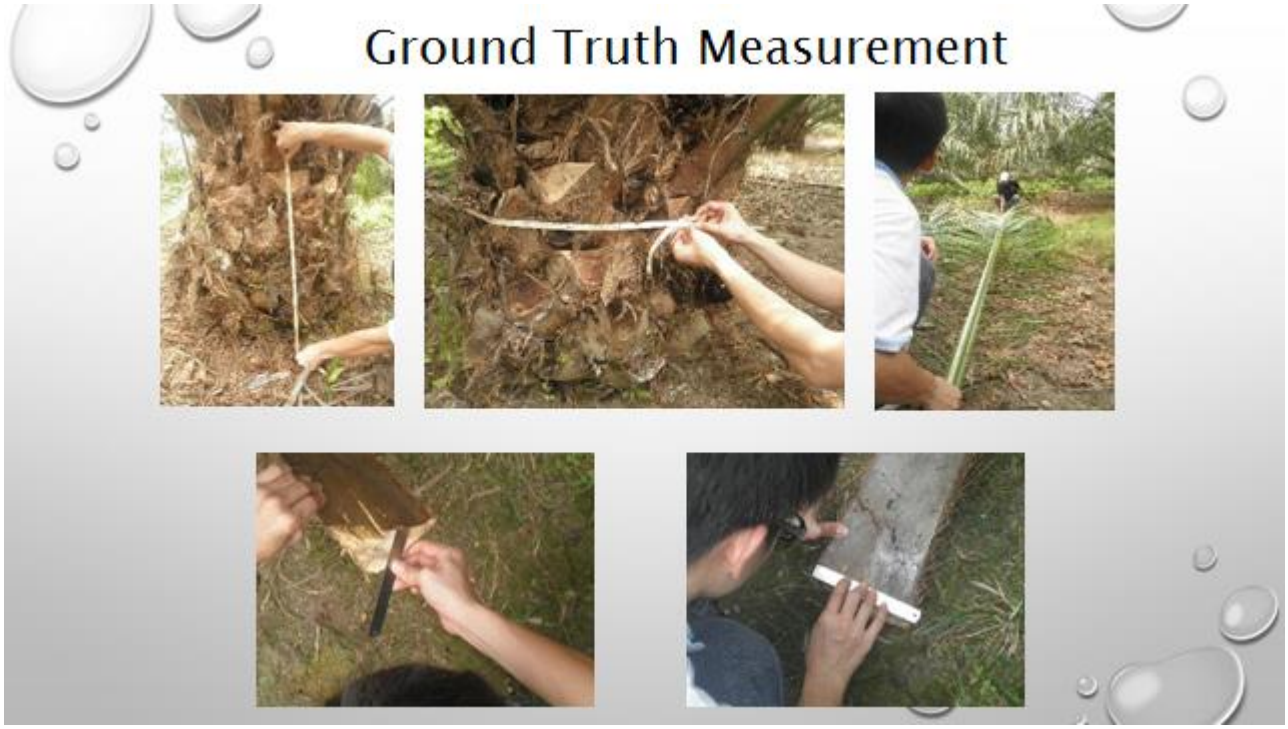

Figure 2: Measuring physical parameters of oil palm plots.

Appendix 5:

LOOP-TREE FREE AUGMENTED EQUIVALENCE PRINCIPLE ALGORITHM FOR LOW FREQUENCY PROBLEMS

1. INTRODUCTION

Solving full-wave electromagnetic problems is challenging, especially when the structure is working at low frequencies [1]. These problems are often encountered in ICs, electronic packaging, PCBs, small antennas, and small sensors. Computational electromagnetics (CEM) research is crucial in accurately predicting the electromagnetic behavior of this kind of structures.

A challenging problem in computational electromagnetics is the electrodynamics problem in the low frequency regime. When the wavelength is much longer than the size of the structure, the physics of the electromagnetic field resembles that of circuits. This is the circuit-physics regime. When the wavelength is sizeable compared to the structure, wave physics becomes important. It is important for a simulation method to capture proper physics at different frequency bands [2]. When a structure is multiscale, it has parts that are small compared to wavelength, and parts that are on the order of wavelength. Hence, both circuit physics and wave physics are equally important. A simulation method has to capture both physics to conquer this difficulty.

A popular way of solving these problems is to use integral equation (IE) methods [3]. Although the IE method with the novel RWG basis [4] has been a prevalent solution to various electromagnetic problems, it does not work well at low frequencies. This is due to the fact that the electric field and the magnetic field are weakly coupled at the low frequency regime decomposing into inductance physics and capacitance physics. Hence, most numerical methods working in mid frequencies do not capture both phenomena simultaneously, yielding low-frequency breakdown. So far, some techniques have been proposed to handle this issue including the loop-tree decomposition [5-7]. However, it is laborious to find the loop-tree basis for complicated structures. In [8], an augmented electric field integral equation (A-EFIE) has been proposed to solve the low-frequency problem without the need of loop-tree basis. In this method, the EFIE is augmented with an additional charge unknown, and an additional continuity equation relating the charge to the current. The resultant equation, after proper frequency normalization, is frequency stable down to very low frequency.

In the work of [9], the equivalence principle algorithm (EPA) has been used to capture the multi-scale physics of complex structures by partitioning objects into parts through equivalence surfaces. The interaction of the electromagnetic field between equivalence surfaces is done through translation operators and the equivalence currents on equivalence surfaces. The solution within the equivalence surface can be obtained by various numerical methods, which must be low frequency stable. To surmount the low frequency issue, [10] used the augmented EPA that applies the similar idea of A-EFIE to separate the vector potential term and scalar potential term. This method avoids ill conditioning at low frequencies. In this method, however, the solvers inside equivalence surfaces employ the loop-tree basis, which becomes burdensome when it comes to the complex structure. Hence, it is beneficial to develop an A-EPA method that is loop-tree free. In this project activity, we developed a new A-EPA that is based on A-EFIE to avoid the loop-tree involvement. Several numerical examples are provided to validate this proposed new method.

2. AUGMENTED EQUIVALENCE PRINCIPLE ALGORITHM

Based on the equivalence principle, the scattering of one object can be calculated in conjunction with an equivalence surface (ES). It includes three steps: outside-in propagation, solving for the current on the object, and inside-out propagation. First, the incident currents on the equivalence surface replace the source outside ES. Next, the electric current on the object is solved by MoM solver. In the last step, the scattered electric and magnetic field can be computed using the electric and magnetic currents on ES. This also can be described by the equivalence principle operator [9] (we also denote it the scattering operator for short):

$$\mathbf{X}^{sca} = \widetilde{S} \cdot \mathbf{X}^{inc} \tag{1}$$

where $\mathbf{X}$ is the unknown vector on ES

$$\mathbf{X}^T = \left[\mathbf{J}_s \quad \frac{1}{\eta}\mathbf{M}_s \quad \rho^e \quad \rho^m \right] \tag{2}$$

and

$$\tilde{S} = \begin{bmatrix} -\hat{\mathbf{n}}' \times \tilde{K}_{HJ}^{S} \\ -\eta^{-1}\hat{\mathbf{n}}' \times \tilde{L}_{EJ}^{S} \\ (c_0\eta)^{-1}\hat{\mathbf{n}}' \cdot \tilde{L}_{EJ}^{S} \\ -\dfrac{\eta}{c_0}\hat{\mathbf{n}}' \cdot \tilde{K}_{HJ}^{S} \end{bmatrix} \cdot \left[\tilde{L}_{pp}\right]^{-1} \cdot \begin{bmatrix} -\tilde{L}_{EJ,v}^{S} \\ -\eta\tilde{K}_{EM}^{S} \\ -\tilde{L}_{EJ,s}^{S} \\ 0 \end{bmatrix}^{T}. \tag{3}$$

Here, $\mathbf{J}_s$ and $\mathbf{M}_s$ are the equivalence electric and magnetic surface current vectors. The magnetic current is normalized by η^{-1}. The superscript T stands for transpose. Definitions of $\tilde{L}$ and $\tilde{K}$ operators can be found from [10]. $\left[\tilde{L}_{pp}\right]^{-1}$ denotes the calculation of inside PEC objects' currents.

Moreover, surface charge density on ES are defined as

$$\rho^{e} = (i\omega)^{-1}\nabla \cdot \mathbf{J}_s \tag{4}$$

$$\rho^{m} = (i\omega)^{-1}\nabla \cdot \mathbf{M}_s. \tag{5}$$

In augmented EPA, the radiation from one ES to another is described by the translation operator $\tilde{T}$ [10]. Then the translation procedure on ES_1 from ES_2 can be described by

$$\mathbf{X}_1 = \tilde{T}_{12} \cdot \mathbf{X}_2 \tag{6}$$

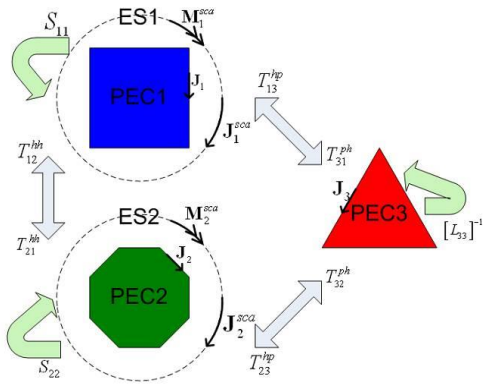

Figure 1 An example of the interactions among two equivalence surfaces and one PEC.

With aid of these operators, we can construct the A-EPA system. For example, with the interaction among two ESs and one PEC as shown in Fig. 1, the equations are

$$\mathbf{X}_1^{sca} - \tilde{S}_{11} \cdot \tilde{T}_{12}^{hh} \cdot \mathbf{X}_2^{sca} - \tilde{S}_{11} \cdot \tilde{T}_{13}^{hp} \cdot \begin{bmatrix} \mathbf{J}_3 \\ \mathbf{M}_3 \end{bmatrix} = \tilde{S}_{11} \cdot \mathbf{X}_1^{inc} \tag{7}$$

$$-\tilde{S}_{22} \cdot \tilde{T}_{21}^{hh} \cdot \mathbf{X}_1^{sca} + \mathbf{X}_2^{sca} - \tilde{S}_{22} \cdot \tilde{T}_{23}^{hp} \cdot \begin{bmatrix} \mathbf{J}_3 \\ \mathbf{M}_3 \end{bmatrix} = \tilde{S}_{22} \cdot \mathbf{X}_2^{inc} \tag{8}$$

$$\tilde{T}_{31}^{ph} \cdot \mathbf{X}_1^{sca} + \tilde{T}_{32}^{ph} \cdot \mathbf{X}_2^{sca} - \tilde{L}_{33}^{S} \cdot \begin{bmatrix} \mathbf{J}_3 \\ \mathbf{M}_3 \end{bmatrix} = -\mathbf{E}_3^{inc} \tag{9}$$

above A-EPA equations describe all the interactions between ESs and PEC object. Iterative methods can be employed to solve the above equation system.

3. A-EPA WITH A-EFIE

A. Using A-EFIE in the scattering operator

The augmented electric field integral equation (A-EFIE) [11] treats the charge as an unknown and introduces an additional equation to relate the current and the charge. Similar to using both Kirchhoff's current and voltage law (KCL and KVL) in Modified Nodal Analysis (MNA), it bypasses the imbalance between the vector potential and the scalar potential in the conventional EFIE. Hence, the A-EFIE formulation includes not only the current but also the charge as unknowns. It has a 2×2 block structure as:

$$\begin{bmatrix} \overline{\mathbf{V}} & \overline{\mathbf{D}}^T\cdot\overline{\mathbf{P}} \\ \overline{\mathbf{D}} & k_0^2\bar{\mathbf{I}} \end{bmatrix}\cdot\begin{bmatrix} ik_0\mathbf{J} \\ c_0\rho \end{bmatrix}=\begin{bmatrix} \eta^{-1}\mathbf{b} \\ 0 \end{bmatrix} \tag{10}$$

where **J** is current density , ρ is the vector of charge density, **b** is the excitation vector, and $\bar{\mathbf{I}}$ is an identity matrix. The sub-matrices are written as

$$\left[\overline{\mathbf{V}}\right]_{m,n}=\mu_r\int_{S_m}\mathbf{\Lambda}_m(\mathbf{r})\int_{S_n}g(\mathbf{r},\mathbf{r}')\mathbf{\Lambda}_n(\mathbf{r}')dS'dS \tag{11}$$

$$\left[\overline{\mathbf{P}}\right]_{m,n}=\varepsilon_r^{-1}\int_{S_m}h_m(\mathbf{r})\int_{S_n}g(\mathbf{r},\mathbf{r}')h_n(\mathbf{r}')dS'dS \tag{12}$$

where $\mathbf{\Lambda}$ stands for the RWG basis function, h is the pulse expansion function, and $g(\mathbf{r},\mathbf{r}')$ is the Green's function in the homogeneous medium. Here, $\overline{\mathbf{D}}$ is a divergence operator and defined as

$$\left[\overline{\mathbf{D}}\right]_{m,n}=\begin{cases} 0, & \text{path } m \text{ does not belong to RWG } n \\ 1, & \text{path } m \text{ is the positive part of RWG } n \\ -1, & \text{path } m \text{ is the negative part of RWG } n \end{cases} \tag{13}$$

The augmented EPA method has the capability to suppress the low-frequency breakdown of EPA method on equivalence surfaces. But its $\tilde{L}$ operator inside the equivalence surface still uses the loop-tree decomposition technique to overcome the low frequency issues. It becomes complicated especially for complex structures. This difficulty can be solved by using the A-EFIE method.

In this method, the $\tilde{S}$ operator of A-EPA becomes

$$\tilde{S}=\begin{bmatrix} -\hat{\mathbf{n}}'\times\tilde{K}_{HJ}^{S} \\ -\eta^{-1}\hat{\mathbf{n}}'\times\tilde{L}_{EJ}^{S} \\ (c_0\eta)^{-1}\hat{\mathbf{n}}'\cdot\tilde{L}_{EJ}^{S} \\ -\dfrac{\eta}{c_0}\hat{\mathbf{n}}'\cdot\tilde{K}_{HJ}^{S} \end{bmatrix}\cdot\left[\tilde{L}_{pp}\right]_{A-EFIE}^{-1}\cdot\begin{bmatrix} -\tilde{L}_{EJ,v}^{S} \\ -\eta\tilde{K}_{EM}^{S} \\ -\tilde{L}_{EJ,s}^{S} \\ 0 \end{bmatrix}^T \tag{14}$$

where the $\left[\tilde{L}_{pp}\right]_{A-EFIE}^{-1}$ is the operator in Eq. (10). Assuming that one object (labeled as *i*) is enclosed in an equivalent surface, the inside operator becomes:

$$\left[\tilde{L}_{pp}^{(i)}\right]_{A-EFIE}^{-1}=\begin{bmatrix} \overline{\mathbf{V}}^{(i)} & \overline{\mathbf{D}}^T\cdot\overline{\mathbf{P}}^{(i)} \\ \overline{\mathbf{D}}^{(i)} & k_0^2\bar{\mathbf{I}} \end{bmatrix}^{-1}. \tag{15}$$

B. Tap basis scheme

Decomposing a general structure into small-scale parts is challenging. In [12], a tap basis scheme has been proposed to handle this difficulty. This scheme can be extended for solving low frequency problems.

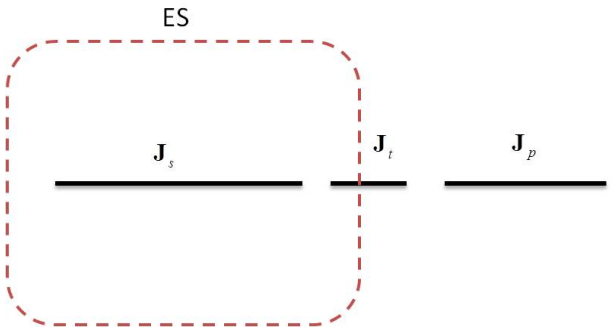

Figure 2 A strip intersects with an equivalence surface.

As shown in Fig. 2, a metallic strip intersects with the equivalence surface. The currents on the strip are then divided into three parts: inside current $\mathbf{J}_s$, tap current $\mathbf{J}_t$, and outside current $\mathbf{J}_p$. Using the same technique of [12], the A-EPA equation system becomes

$$\begin{bmatrix} I & 0 & \tilde{\tilde{S}}\cdot\tilde{\tilde{T}}^{hp} & \tilde{\tilde{S}}^{ht} \\ 0 & I & \tilde{\tilde{S}}^{th}\cdot\tilde{\tilde{T}}^{hp} & \tilde{\tilde{S}}^{tt} \\ \tilde{\tilde{T}}^{ph} & 0 & \tilde{\tilde{L}}^{pp} & \tilde{\tilde{L}}^{pt} \\ 0 & I & \tilde{\tilde{L}}^{tp} & \tilde{\tilde{L}}^{tt} \end{bmatrix} \cdot \begin{bmatrix} \mathbf{X} \\ \mathbf{t} \\ \mathbf{Y}_p \\ \mathbf{Y}_t \end{bmatrix} = \begin{bmatrix} \tilde{\tilde{S}}\mathbf{X}^{inc} \\ \tilde{\tilde{S}}^{th}\mathbf{X}^{inc} \\ -\mathbf{E}_p^{inc} \\ -\mathbf{E}_t^{inc} \end{bmatrix} \tag{16}$$

where $\mathbf{Y}$ refers to $\begin{bmatrix}\mathbf{J} & \rho\end{bmatrix}^T$, $\mathbf{t}$ is the tap vector

$$\mathbf{t} = \tilde{\tilde{L}}^{ts}\mathbf{Y}_s. \tag{17}$$

4. NUMERICAL RESULTS

To demonstrate the accuracy and validity of the proposed method, we simulated several examples, including both scattering and radiation problems. The platform we worked on is a computer with 2.67 GHz CPU, 12 GB memory, and the Linux operating system.

In the first example, the scattering problem of a PEC sphere is calculated. The PEC sphere with a radius of 1.0 m is enclosed in a Huygens' box that has the edge length of 2.4 m. This sphere is illuminated by an *x*-polarized plane wave from the $+z$ direction. Fig. 3(a) shows the RCS result solved by EPA with normal EFIE while Fig. 3(b) demonstrates the corresponding result solved by A-EPA with A-EFIE. As can be seen from these two figures, traditional EPA method fails to obtain the correct answer at 1 MHz whereas A-EPA with A-EFIE can work well even at frequencies as low as 2 KHz.

Next, we use the proposed method to simulate a differential via-hole structure. Two coupled striplines start from the upper layer, go through the via-holes to the second layer, and then return to the first layer. This differential vias with holes are frequently encountered in integrated circuits. The geometry specifications are shown in Fig. 4.

In order to alleviate the computational burden, two equivalent surfaces are employed. It shall be noted that finding the loop-tree basis for this via-holes structure is laborious because it takes significant efforts to search for global loops in the presence of holes. The proposed method circumvents this trouble by A-EFIE operator method inside ESs.

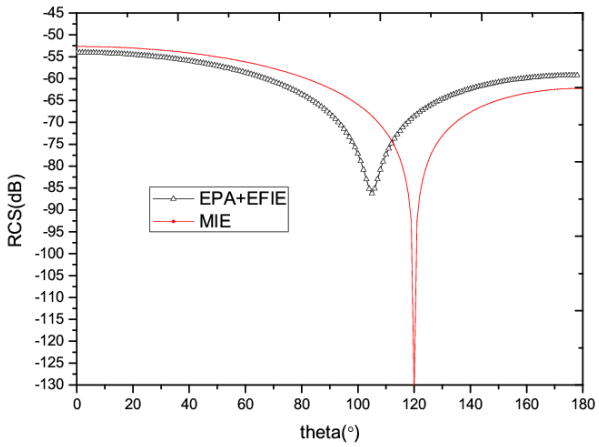

(a)

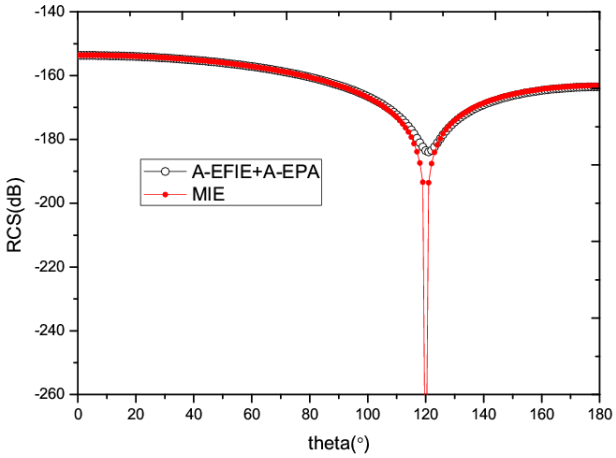

(b)

Figure 3 Scattering of a unit sphere: (a) simulated by EPA with EFIE at 1MHz, (b) simulated by proposed method at 2KHz.

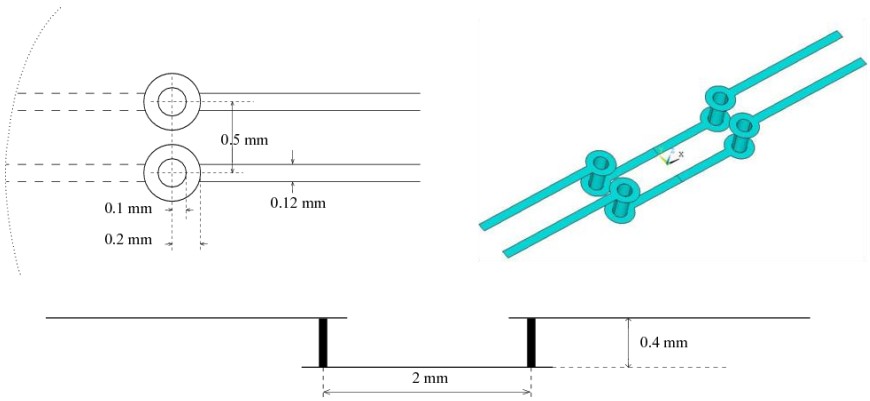

Figure 4 Differential vias structure: top view, side view and tracks only.

In this case, the via-hole structure is enclosed by two ESs as shown in Fig. 5. A delta feed port is imposed at the middle of its left end. The calculated current distribution of this structure is showing in Fig. 6 where the wavelength is 3.0 mm. The results are validated by normal MoM with A-EFIE.

As the third example, a metallic ball array is modeled and simulated. The coupling current distribution has been analyzed when one of balls is excited by a delta source. 32 EPA boxes are created and used. Due to the geometry similarity of all the balls, A-EPA with A-EFIE only one scattering operator is solved and reused for coupling interactions. The current distribution is shown in Fig. 7 at the frequency of 300 MHz.

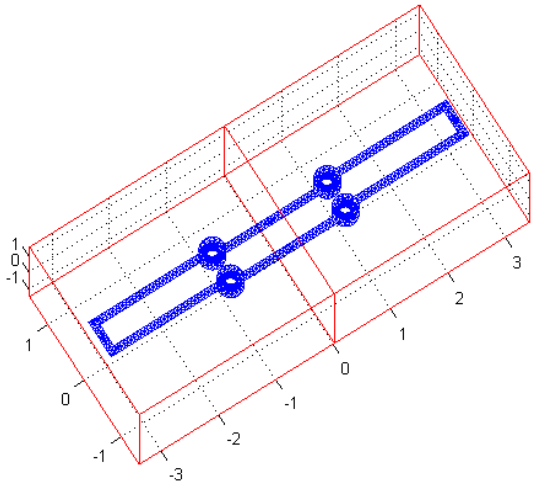

Figure 5 Two ESs enclose the via hole structure.

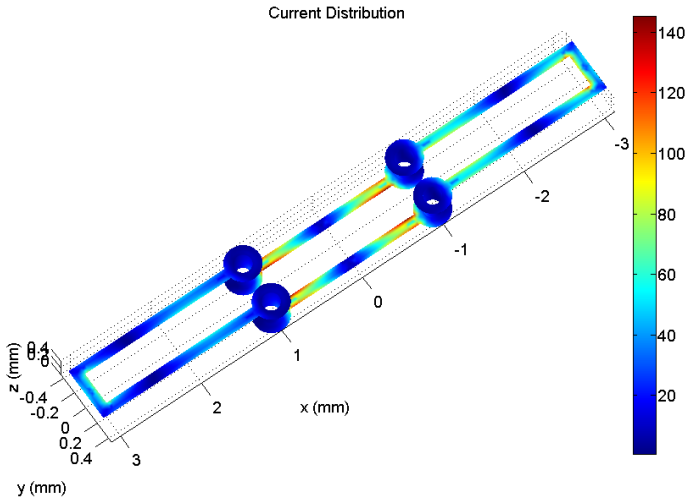

Figure 6 Current Distribution of via-hole structure.

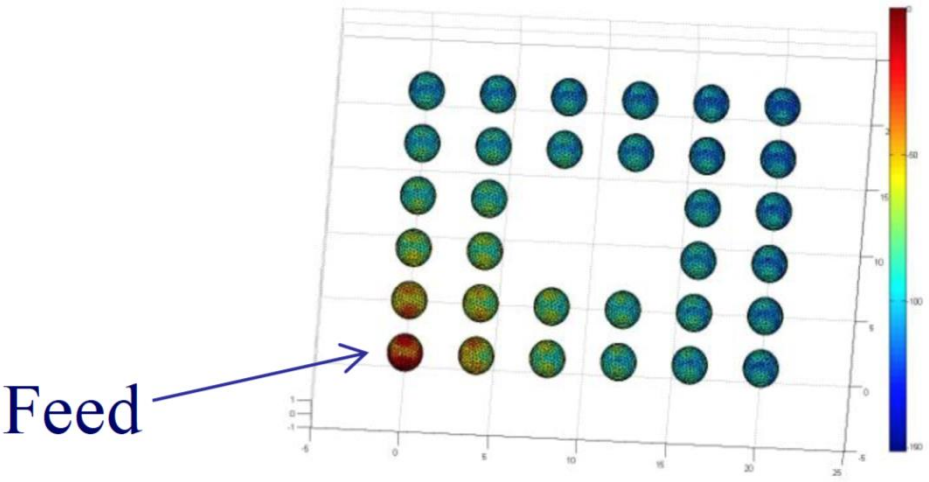

Figure 7 Ball array analysis: top view, geometry specification and current distribution. Frequency is 300MHz. The center to center distance between neighboring balls is 4 mm. The diameter of each ball is 2 mm.

5. CONCLUSION

In this work, a new augmented EPA with augmented EFIE has been presented to solve low frequency domain decomposition problems. The A-EPA applies equivalent surface electric and magnetic charges to bypass the low frequency instability problem. With the incorporation of A-EFIE in the scattering operator, this method can be used to solve low frequency problems without using loop-tree basis. From numerical verifications, the proposed method is stable and effective in solving problems at low frequencies. Furthermore, this method can be further integrated with fast multipole methods (FMM) to solve large-scale problems.

REFERENCES

1. W. C. Chew, L. Jiang, Y. Chu, G. Wang, L.-T. Chiang, Y. Pan, and J. Zhao, Toward a more robust and accurate CEM fast integral equation solver for IC applications, IEEE Trans Advanced Packaging 28(2005), 449–464.
2. W. C. Chew, Computational electromagnetics–the physics of smooth versus oscillatory fields, Philo. Trans. Royal Soc. London Series A, Math., Phys. Eng. Sci., 362 (2004), 579–602.
3. R. F. Harrington, Field Computation by Moment Method, MacMillan, New York (1968).
4. S. Rao, D. Wilton, and A. Gllisson, Electromagnetic scattering by surfaces of arbitrary shape, IEEE Trans Antennas and Propagation 30 (1982), 409–418.
5. D. R. Wiltion and A. W. Glisson, On improving the electric field integral equation at low frequencies, In: Proceeding of the URSI Radio Science Meeting Digest, Los Angeles, CA, USA, 1980, p. 24.
6. J. Mautz and R. Harrington, An E-field solution for a conducting surface small or comparable to the wavelength, IEEE Trans Antennas and Propagation 32 (1984), 330–339.
7. J.-S. Zhao and W. C. Chew, Integral equation solution of Maxwell's equations from zero frequency to microwave frequencies, IEEE Trans Antennas and Propagation 48 (2000), 1635–1645.
8. Z.-G. Qian and W. C. Chew, A quantitative study on the low frequency breakdown of EFIE, Microwave Opt Technol Lett 50 (2008), 1159-1162.
9. M. K. Li, W. C. Chew and L. J. Jiang, A domain decomposition scheme based on equivalence theorem, Microwave Opt Technol Lett 48 (2008), 1159-1162.
10. L. E. Sun, W. C. Chew and J. M. Jin, Augmented equivalence principle algorithm at low frequencies, Microwave Opt Technol Lett 52 (2010), 2274-2279.
11. Z.-G. Qian and W. C. Chew, Fast full-wave surface integral equation solver for multiscale structure modeling, IEEE Trans Antennas and Propagation 57 (2009), 3594–3601.
12. M.-K. Li and W. C. Chew, Multiscale simulation of complex structures using equivalence principle algorithm with high-order field point sampling scheme, IEEE Trans Antennas and Propagation 56 (2008), 2389–2397.

Appendix 6:

A Novel Broadband Equivalent Source Reconstruction Method for Broadband Radiators

1 INTRODUCTION

Equivalent source reconstruction methods are widely employed as a near-field (NF) measurement post-processing technique. With this equivalent source, antenna diagnostics, near-field to far-field transformations (NF-FF), etc., can be easily performed. Moreover, source reconstruction is more flexible in handling complex geometries where equivalent current source as well as the measurement domain reside. These merits are hard to be observed in wave expansion methods [1].

The source reconstruction method (SRM) has received intensive attention for near-field far-field (NF-FF) transformations. People firstly facilitate SRM by placing equivalent electric or magnetic current sources at an infinite large planar perfect electric conductor (PEC) or magnetic conductor (PMC) [2]-[3]. The deficiency of these methods is its difficulties in handling the whole 3-D radiation pattern. This problem was addressed in [4] by constructing the equivalent current source over an surface enclosing the radiator or just the surface of the radiator. The fast multipole algorithm is introduced in [5] to accelerate the matrix-vector product with the purpose of tackling electrical large problems.

However, the equivalent sources built in these references are only mostly valid at a single frequency. Our aim is to construct the equivalent source that is able to deal with wide-band problems without involving all frequencies. With this wide-band model, the computational cost will be greatly reduced since we do not need to invert or factorize

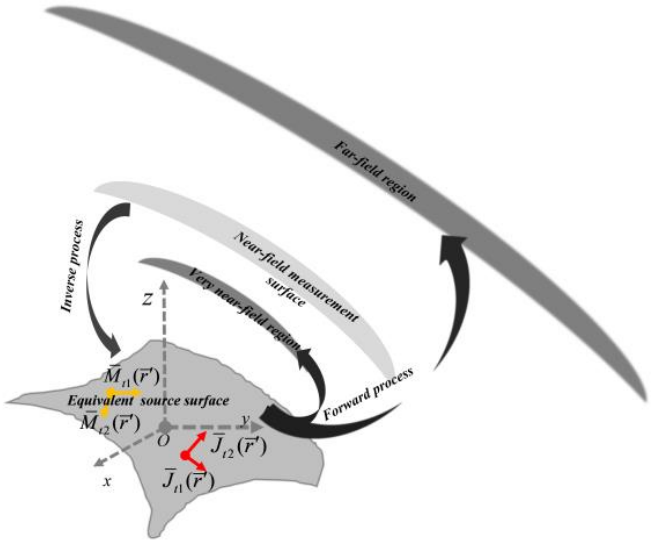

Figure 1: The inverse equivalent source reconstruction process and the NF-NF or NF-FF transformation process.

the matrix system at each frequency. To achieve our purpose, an efficient interpolation algorithm suitable for our problem must be developed. In this work, the Neville-type Stoer-Bulirsch rational interpolation algorithm is adopted [6]. The SB algorithm is derivative free. Thus, it is amenable to our problem. To effectively reduce the number of samples, an adaptive frequency sampling strategy based on the bisection-searching scheme allowing frequency step to be locally refined without limitation is employed.

In order to achieve high-order accuracy, high-order hierarchical basis can be used. But it will make the problem very complex and increase the amount of computation required per entry of the system matrix. Another easy and convenient alternative is the Nystrom method [7]. In the Nystrom method, the unknown quantity is represented by its samples at the quadrature nodes

2 FORMULATION OF THE SRM

The electromagnetic equivalence principle [8] states that only the tangential electric or magnetic field over a closed surface surrounding the device/antenna under test (DUT/AUT) is needed to characterize the electromagnetic radiation from the DUT/AUT. The tangential electric and magnetic fields correspond to the equivalent magnetic and electric currents, respectively. This equivalent source may be comprised of electric current $\mathbf{J_s}$, magnetic current $\mathbf{M_s}$ or both. They are capable of reproducing the original radiation outside that surface. For the inverse radiation problem, the unknown equivalent

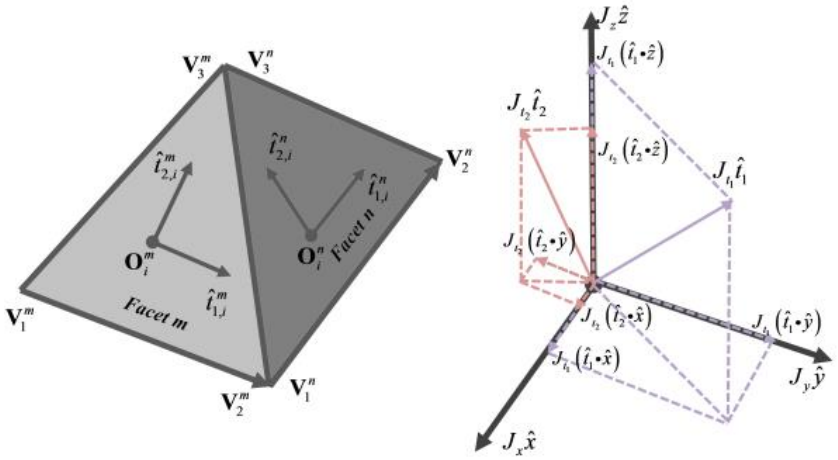

Figure 2: Two local orthogonal components of the surface current in each triangle facet.

source is determined by the measured near-field data over an arbitrary surface shown in Fig. 1. After building the equivalent source, the NF-NF and NF-FF transformations are able to be performed with little effort. Integral equations are implemented the SRM:

$$\mathrm{E}(\mathrm{r}_{Meas}) = \mathrm{E}_{\mathrm{Js}'} + \mathrm{E}_{\mathrm{Ms}'} \tag{1}$$

where

$$\begin{aligned} \mathrm{E}_{\mathrm{Js}'} = -j\eta_0 k_0 \int_{s'} [\mathrm{J}_{s'}(\mathrm{r}') \frac{e^{-jkR}}{4\pi R} \\ + \frac{1}{k_0^2} \nabla\nabla' \cdot \mathrm{J}_{s'}(\mathrm{r}') \frac{e^{-jkR}}{4\pi R}] dS' \end{aligned} \tag{2}$$

$$\mathrm{E}_{\mathrm{Ms}'} = \int_{s'} M_{s'}(\mathrm{r}') \times \nabla \frac{e^{-jkR}}{4\pi R} dS' \tag{3}$$

3 NYSTROM METHOD

To solve the integral equation (1), we need to transform it into a matrix equation basis functions that are used to represent equivalent sources. To achieve high order accuracy, Nystrom method is applied in this work. The integrations in (2) and (3) are implemented with proper quadrature rules. For a surface integration, Nystrom method [7] is formulated as

$$\int_{s'} f(\mathrm{r}') dS' = \sum_{i=1}^{p} \omega_i f(\mathrm{r}_i') \tag{4}$$

where $f(\mathrm{r}')$ is a smooth function, p is the number of quadrature points. After dividing the surface S' into a series of non-overlapping elements that are usually triangles in the surface integral equation (SIE) and choosing proper number of quadrature points, the entries of the matrix equations are simply the direct product between the integral kernel and weights of the quadrature rule at those points. Another important benefit of the Nystrom method is that it can deal defective meshes such as non-conforming meshes encountered in MoM.

Since the integration region is on surfaces, we suppose that the unknown currents at Gaussian quadrature points have two orthogonally tangential components as defined below and shown in Fig. 2.

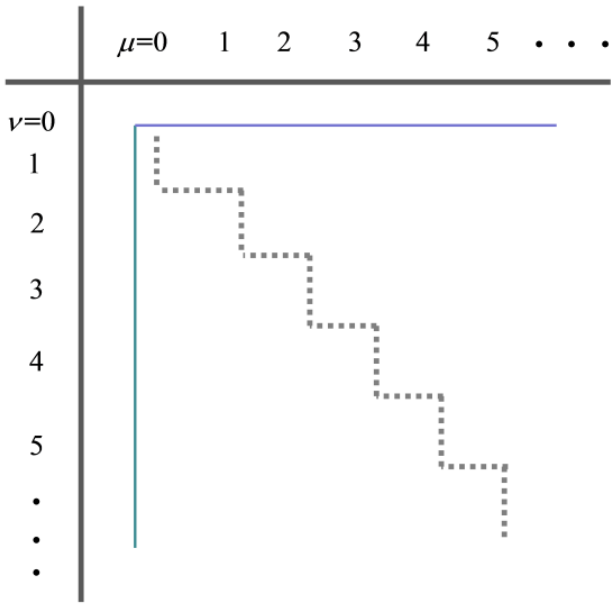

Figure 3: Recursive tabular chart.

By performing the Nystrom method in (4) over the integral equations in (1)-(3), a matrix equation system based on the NF sampled data will be obtained after a length mathematical calculation:

$$\begin{pmatrix} \bar{\mathrm{E}}_{\theta} \\ \bar{\mathrm{E}}_{\phi} \end{pmatrix} = \begin{pmatrix} \bar{\bar{\mathrm{Z}}}_{\theta,J_{t1}} & \bar{\bar{\mathrm{Z}}}_{\theta,J_{t2}} & \bar{\bar{\mathrm{Z}}}_{\theta,M_{t1}} & \bar{\bar{\mathrm{Z}}}_{\theta,M_{t2}} \\ \bar{\bar{\mathrm{Z}}}_{\phi,J_{t1}} & \bar{\bar{\mathrm{Z}}}_{\phi,J_{t2}} & \bar{\bar{\mathrm{Z}}}_{\phi,M_{t1}} & \bar{\bar{\mathrm{Z}}}_{\phi,M_{t2}} \end{pmatrix} \begin{pmatrix} \bar{\bar{\mathrm{J}}}_{t1} \\ \bar{\bar{\mathrm{J}}}_{t2} \\ \bar{\bar{\mathrm{M}}}_{t1} \\ \bar{\bar{\mathrm{M}}}_{t2} \end{pmatrix} \tag{5}$$

For brevity, the matrix equation in (5) is rewritten as:

$$\begin{pmatrix} \bar{\mathrm{E}}_{\theta} \\ \bar{\mathrm{E}}_{\phi} \end{pmatrix} = \begin{pmatrix} \bar{\bar{\mathrm{Z}}}_{\theta,J} & \bar{\bar{\mathrm{Z}}}_{\theta,M} \\ \bar{\bar{\mathrm{Z}}}_{\phi,J} & \bar{\bar{\mathrm{Z}}}_{\phi,M} \end{pmatrix} \begin{pmatrix} \bar{\mathrm{J}}/J_0 \\ \bar{\mathrm{M}}/\mathrm{M}_0 \end{pmatrix} \tag{6}$$

The finalized matrix equation will be iteratively solved by the conjugate gradient algorithm in this work.

4 THEORY OF THE STOER-BULIRSCH ALGORITHM WITH ADAPTIVE FREQUENCY SAMPLING

Suppose a given group of samples $\{(f_i, P(f_i))\ i=0, 1, ..., N\}$ representing values of desired observables. f_i is the i-th frequency point, $P(f_i)$ is the i-th frequency response. In the frequency band from f_1 to f_N, these supporting points can be interpolated by rational functions [14]-[15]:

$$R(f) = \frac{A(f)}{B(f)} = \frac{a_0 + a_1 f + \cdots + a_\mu f^\mu}{b_0 + b_1 f + \cdots + b_\nu f^\nu} \tag{7}$$

Instead of solving these polynomial coefficients explicitly, Stoer and Bulirsch introduced a recursive tabular algorithm to determine the value of the interpolating rational function R at the sampling frequency point f The

SB algorithm is free of singularity and requires no matrix inversion. Hence, it can tackle large number of supporting points.

Three FMs are included in the SB algorithm. They are two "triangle rules" and one "rhombus rule". In this work, the "rhombus rule" in (8) is employed.

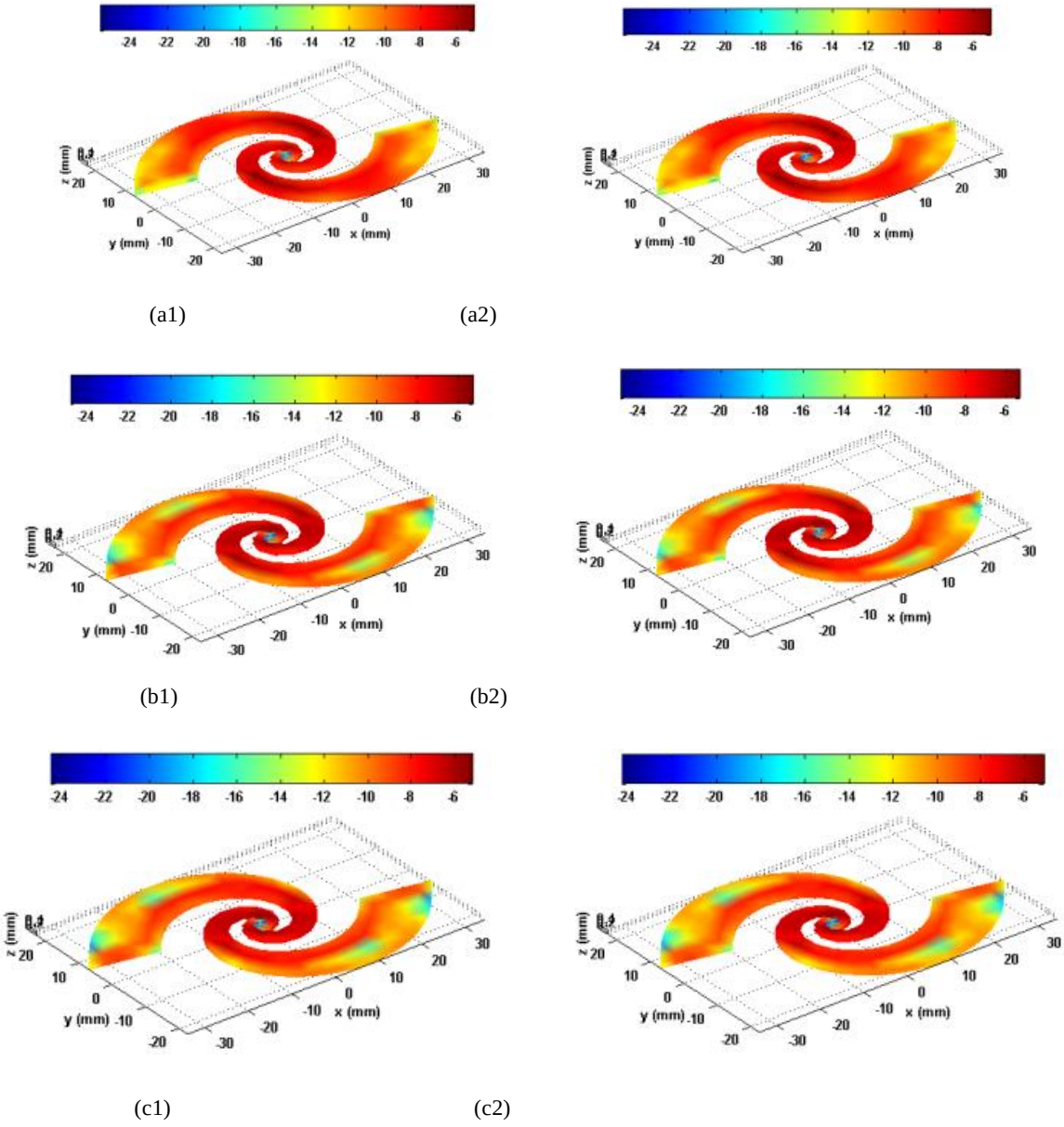

Figure 4: The interpolated equivalent electric currents (dB A/m) based on the SB-algorithm with the "rhombus rule" (right column) and their counterparts by solving (15) (left column). (a1-a2) are the equivalent currents at 4.125 GHz. (b1-b2) are the equivalent currents at 5.625 GHz. (c1-c2) are the equivalent currents at 6.125 GHz.

$$T_{i,k} = T_{i,k-1} + \frac{T_{i,k-1} - T_{i-1,k-1}}{\dfrac{f - f_{i-k}}{f - f_i}\left[1 - \dfrac{T_{i,k-1} - T_{i-1,k-1}}{T_{i,k-1} - T_{i-1,k-2}}\right] - 1} \tag{8}$$

The recursive table in Fig. 3 for the "rhombus rule" starts with the initial conditions $T_{i,-1}=0$ and $T_{i,0}=P(f_i)$.

To improve the interpolation efficiency, AFS strategy is integrated with the SB algorithm. AFS performs the bisection of each individual initially chosen frequency interval δf until a termination criterion is reached. The AFS process starts with computing the observable samples by solving the matrix equation in (6) at the sample frequencies uniformly spaced by a coarse initial frequency step δf over the whole frequency band of interest. These samples are kept as the initial data for SB algorithm. Then, the frequency nodes $f_{new}=(f_i+f_{i+1})/2$ is obtained at the subinterval (f_i, f_{i+1}). The new solution $\boldsymbol{X}_{new}$ at f_{new} is again solved via the matrix equation in (6) and compared with the data $\boldsymbol{X}_{SB}$ obtained from the SB interpolation with "rhombus rule" in (8). If the error function satisfies

$$\frac{\left\| X_{new} - X_{SB} \right\|}{\left\| X_{new} \right\|} < \varepsilon \tag{9}$$

, the process is terminated in this subinterval and moves to the next subinterval. The bisection process will continue until all of the convergence criterions are achieved. All the above generated data are kept as the samples for the SB interpolation algorithm.

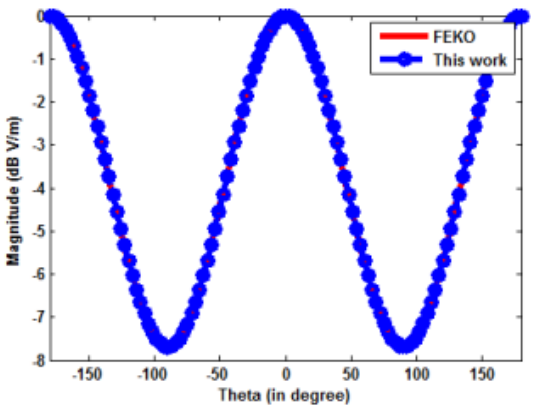

(a1)

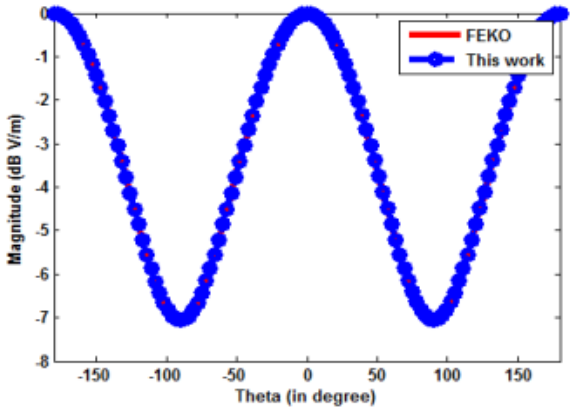

(a2)

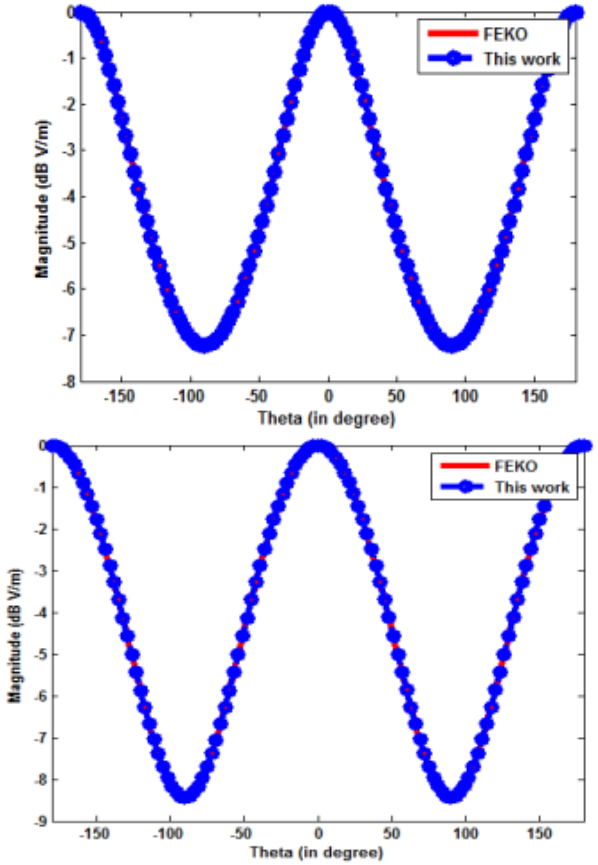

(b1) (b2)

Figure 5: The normalized far-field radiation (dB V/m) at *f*=4.125 GHZ (a1-a2) and 5.625 GHz (b1-b2), respectively. The left column are those in the *xoz* plane, the right column are those in the *yoz* plane.

5 Numerical Examples

To further verify the accuracy and efficiency of the proposed algorithm for more practical wide band application, a helical antenna operating from 4 to 11 GHz is investigated. To capture its 3D radiation property, the near field sampling is conducted over a spherical surface with radius R=1 m. At each sampling point, both θ and φ components of the electric field are acquired with the angular resolution five degree. All of the sampled near field data is obtained from the commercial full-wave software FEKO [15]. Since this helical antenna consists of PEC only, only the contribution from the equivalent electric current is considered. The surface of this antenna is triangulated into 704 patches and the three-point quadrature rule is employed, which results in 4224 unknowns.

The SB-algorithm with the AFS starts with a coarse sampling rate of f_{step}=500 MHz, and 20 samples are finally required to establish a single rational function model of the reconstructed equivalent source with δ_{mean}=1.97%. The frequencies of these supporting points are f_s={4.0, 4.25, 4.5, 4.75, 5.0, 5.25, 5.5, 5.75, 6.0, 6.25, 6.5, 7.0, 7.5, 8.0, 8.5, 9.0, 9.5, 10.0, 10.5, 11.0} GHz. the reconstructed equivalent current sources using the SB interpolation algorithm at *f*= 4.125 and 5.625 GHz are compared with those directly solved by (6). The results are presented in Fig. 4. No obvious differences are noted. Next, the normalized far-field patterns these three points are presented in Fig. 5. Also, very good agreements are achieved. It means that these current distribution differences originated from the SB scheme have trivial influences on the far field radiation, which is attributable to the existence of non-radiating sources. To further show the influences on the near field

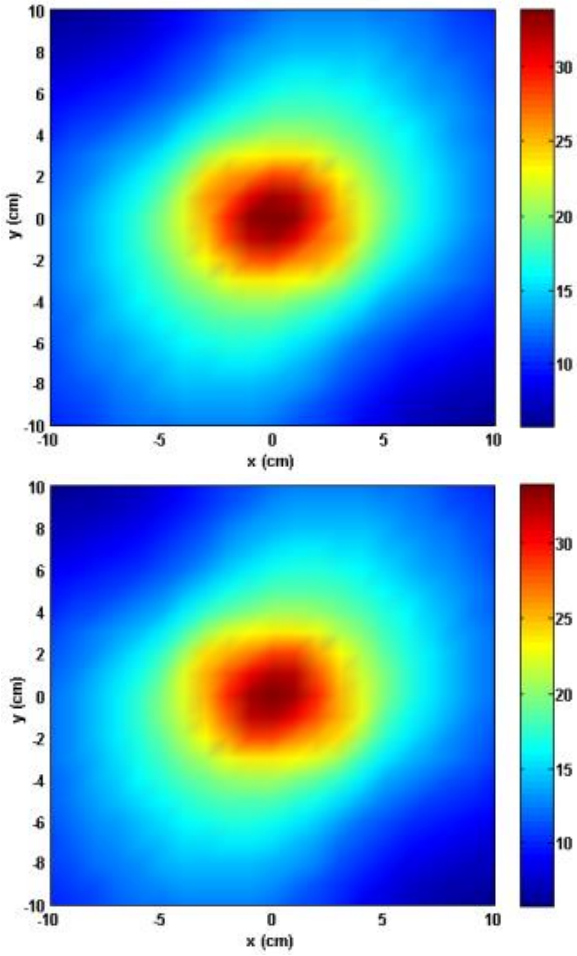

(a1) (a2)

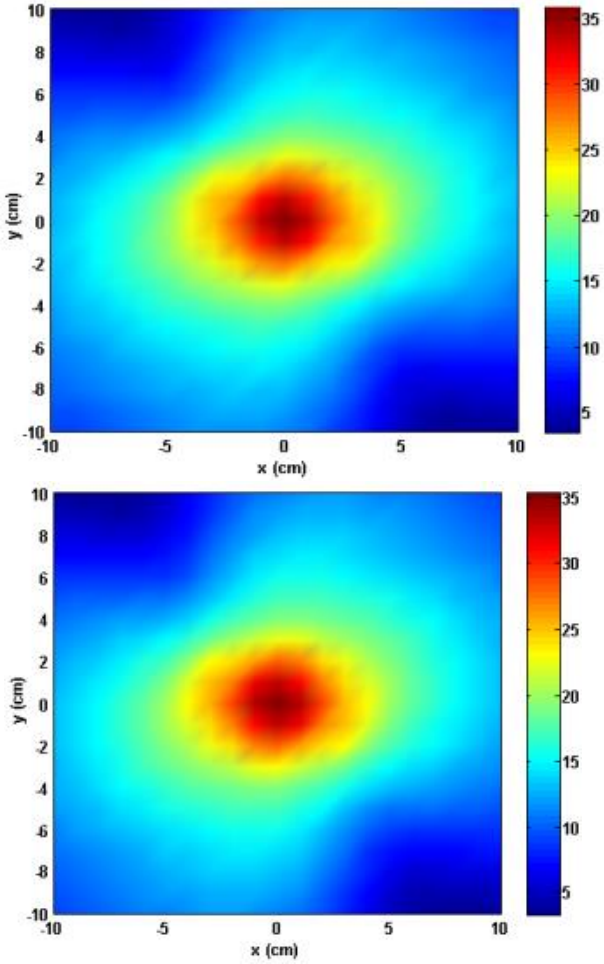

(b1) (b2)

Figure 6: Calculated near field (dB V/m) over a plane with z=1 cm at *f*=4.125 GHz (a1-a2) and 5.625 GHz (b1-b2), respectively. The left column are those calculated from FEKO. The right column are those computed from the interpolated current sources.

prediction, the electric near field distributed over a rectangular plane at z=1 cm is calculated. The size of this plane is 20 cm in *x*-direction and 20 cm in the *y*-direction. The sampling resolution is δx=1 cm and δy=1cm. The results are shown in Fig. 6. Good agreements are noted again.

6 Conclusion

This work proposed a wide band equivalent source reconstruction method based on the SB-algorithm. It is derivative-free, it avoids the singularity issue during the wide band source reconstruction process. The resultant wide band equivalent source is completely represented by a single rational function. To reduce the sampling points, the bisection method based adaptive sampling scheme is employed. This SB-algorithm with AFS significantly reduces the computational cost since only a very small number of frequency points need to be solved. To verify the feasibility of the proposed method, a planar spiral antenna is benchmarked.

References

[1] P. Li and L. J. Jiang, "The far field transfor- mation for the antenna modeling based on spherical electric field measurements," *Prog. In Electromagn. Research*, vol. 123, pp. 243-261, 2012.

[2] P. Peter and T. K. Sarkar, "Planar near-field to far -field transformation using an equivalent magnetic current approach," *IEEE Trans. Antennas Propag.*, vol. 40, no. 11, pp. 1348-1356, Nov. 1992.

[3] T. K. Sarkar and A. Taaghol, "Near-field to near /far-field transformation for arbitrary near-field geometry utilizing an equivalent electric current and MOM," *IEEE Trans. Antennas Propag.*, vol. 47, no. 3, pp. 566-573, Mar. 1999.
[4] Y. Alvarez, F. Las-Heras, and M. R. Pino, "Reconstruction of equivalent currents distri- bution over arbitrary three-dimensional surfaces based on integral equation algorithms," *IEEE Trans. Antennas Propag*., vol. 55, no. 12, pp. 3460-3468, Dec. 2007.
[5] T. F. Eibert and C. H. Schmidt, "Multilevel Fast multipole accelerated inverse equivalent current method employing Rao-Wilton-Glisson discre- tization of electric and magnetic surface currents," *IEEE Trans. Antennas Propag*., vol. 57, no. 4, pp. 1178-1185, Apr. 2009.
[6] J. Stoer and R. Bulirsch, *Introduction to Numerical Analysis*, Third Edition, Springer, New York, 2002.
[7] A. F. Peterson and M. M. Bibby, *An introduction to the locally-corrected Nystrom method*, Morgan and Claypool Publisher, 2010.
[8] S. R. Rengarajan and Y. Rahmat-Samii, "The field equivalence principle: illustration of the establishment of the non-intuitive null fields," *IEEE Antennas Propag. Mag*., vol. 42, no. 4, pp. 122-128, Aug. 2000.